Fall 2017

Comparative study of near-infrared pulsed laser machining of carbon fiber reinforced plastics

Timothy Donald Heiderscheit
University of Iowa

Recommended Citation

Heiderscheit, Timothy Donald. "Comparative study of near-infrared pulsed laser machining of carbon fiber reinforced plastics." MS (Master of Science) thesis, University of Iowa, 2017.
https://doi.org/10.17077/etd.por88e8m

Follow this and additional works at: https://ir.uiowa.edu/etd
Part of the Mechanical Engineering Commons

COMPARATIVE STUDY OF NEAR-INFRARED PULSED LASER MACHINING OF CARBON FIBER REINFORCED PLASTICS

by

Timothy Donald Heiderscheit

A thesis submitted in partial fulfillment
of the requirements for the Master of Science
degree in Mechanical Engineering in the
Graduate College of
The University of Iowa

December 2017

Thesis Supervisor: Professor Hongtao Ding

Graduate College
The University of Iowa
Iowa City, Iowa

CERTIFICATE OF APPROVAL

MASTER’S THESIS

This is to certify that the Master’s thesis of

Timothy Donald Heiderscheit

has been approved by the Examining Committee for
the thesis requirement for the Master of Science degree
in Mechanical Engineering at the December 2017 graduation.

Thesis Committee:

Hongtao Ding, Thesis Supervisor

Hiroyuki Sugiyama

Shaoping Xiao

To my entire family and friends:

ACKNOWLEDGEMENTS

I would like to thank my advisor, Professor Hongtao Ding, for all of his support during my time in the College of Engineering. His expertise has been a valuable resource in helping me complete this research and navigating graduate school. I would also like to thank everyone in the Laser Materials Processing Lab – Ninggang 'George' Shen, Qinghua 'Nicholas' Wang, and Avik Samanta – for all the time and effort that they have contributed to my success. I couldn't have done it without all of their help. Throughout my years at Iowa, I have had a chance to work with some of the best colleagues around and I wish all of them nothing but success in all of their future endeavors.

I've made some of the best friends I could ask for here at Iowa. They've pushed me to achieve and always had my back, no matter what. I would like to thank my family, especially my parents. Without their love and support, none of my accomplishments would have been possible. And lastly, I would like to remember my grandparents – I miss you very much and hope that this makes you proud. To everyone who has played a role in my life: your belief has helped me to get to where I am and to become the person I am today.

This is for you!

ABSTRACT

Carbon fiber-reinforced plastics (CFRPs) have gained widespread popularity as a lightweight, high-strength alternative to traditional materials. The unique anisotropic properties of CFRP make processing difficult, especially using conventional methods. This study investigates laser cutting by ablation as an alternative by comparing two near-infrared laser systems to a typical mechanical machining process. This research has potential applications in the automotive and aerospace industries, where CFRPs are particularly desirable for weight savings and fuel efficiency.

First, a CNC mill was used to study the effects of process parameters and tool design on machining quality. Despite high productivity and flexible tooling, mechanical drilling suffers from machining defects that could compromise structural performance of a CFRP component. Rotational feed rate was shown to be the primary factor in determining the axial thrust force, which correlated with the extent of delamination and peeling. Experimental results concluded that machining quality could be improved using a non-contact laser-based material removal mechanism.

Laser machining was investigated first with a Yb:YAG fiber laser system, operated in either continuous wave or pulse-modulated mode, for both cross-ply and woven CFRP. For the first time, energy density was used as a control variable to account for changes in process parameters, predicting a logarithmic relationship with machining results attributable to plasma shielding effects. Relevant process parameters included operation mode, laser power, pulse overlap, and cross-ply surface fiber orientation, all of which showed a significant impact on single-pass machining quality. High pulse frequency was required to successfully ablate woven CFRP at the weave boundaries, possibly due to matrix absorption dynamics. Overall, the Yb:YAG fiber laser system showed improved performance over mechanical machining. However, microsecond pulses cause extensive thermal damage and low ablation rates due to long laser-material interaction time and low power intensity.

Next, laser machining was investigated using a high-energy nanosecond-pulsed Nd:YAG NIR laser operating in either Q-Switch or Long Pulse mode. This research demonstrates for the first time that keyhole-mode cutting can be achieved for CFRP materials using a high-energy nanosecond laser with long-duration pulsing. It is also shown that short-duration Q-Switch mode results in an ineffective cutting performance for CFRP, likely due to laser-induced optical breakdown. At sufficiently high power intensity, it is hypothesized that the resulting plasma absorbs a significant portion of the incoming laser energy by the inverse Bremsstrahlung mechanism. In Long Pulse mode, multi-pass line and contour cutting experiments are further performed to investigate the effect of laser processing parameters on thermal damage and machined surface integrity. A logarithmic trend was observed for machining results, attributable to plasma shielding similar to microsecond fiber laser results. Cutting depth data was used to estimate the ablation threshold of Hexcel IM7 and AS4 fiber types. Drilling results show that a 2.2 mm thick cross-ply CFRP panel can be cut through using about 6 laser passes, and a high-quality machined surface can be produced with a limited heat-affected zone and little fiber pull-out using inert assist gas. In general, high-energy Long Pulse laser machining achieved superior performance due to shorter pulse duration and higher power intensity, resulting in significantly higher ablation rates. The successful outcomes from this work provide the key to enable an efficient high-quality laser machining process for CFRP materials.

PUBLIC ABSTRACT

Carbon fiber-reinforced plastics (CFRPs) have gained popularity as a lightweight, high-strength alternative to traditional materials. However, the same properties that give CFRP superior performance also make processing difficult and prohibitively expensive by conventional methods. This study focuses on laser machining as an alternative to conventional methods and investigates the underlying mechanisms of laser-based materials processing for CFRP. This research has potential applications in the automotive and aerospace industries, where reduced cost might allow the full potential of CFRPs to be realized for use in weight savings and fuel efficiency without sacrificing strength.

Three machining systems for CFRP are presented in this study. First, conventional mechanical drilling is examined to establish a baseline level of machining performance. Despite high productivity and widespread availability, severe damage during conventional drilling results in generally poor quality for CFRP. Laser machining is investigated, first using a CW/modulated fiber laser system. Mechanical defects are eliminated, but new issues related to thermal distortion are introduced due to the physiochemical nature of the laser ablation process. Microsecond pulse duration at low intensity reduces thermal damage but also reduces material removal efficiency. Machining performance is drastically improved using a high-energy nanosecond-pulsed laser system. Pulse duration is reduced and intensity is increased, both by several orders of magnitude, to significantly increase the material removal rate and decrease thermal damage. At sufficient intensity, plasma formation and absorption becomes important. When combined with an inert assist gas flow, such a laser system is capable of high quality CFRP machining using less than 10 scans for samples of 2.2 mm thickness by line-cutting, pocketing, and contour drilling.

TABLE OF CONTENTS

LIST OF TABLES

LIST OF FIGURES

CHAPTER 1.

INTRODUCTION

Carbon fiber-reinforced plastic (CFRP) is a two-component anisotropic structure comprised of a binding plastic matrix and mechanical reinforcements. The reinforcements are small fibers approximately 5-10 μm in diameter made of carbon filaments produced from a precursor, most commonly polyacrylonitrile (PAN). The binding matrix is typically an epoxy resin or polymer. Thermomechanical properties of CFRP are directional, depending on the layup orientation of the fibers within individual laminate layers and within the overall structure. Figure 1-1 shows the three main layup categories for CFRP: (1) unidirectional, (2) cross-ply (sometimes referred to as quasi-isotropic), and (3) woven. Unidirectional CFRP possesses the highest maximum mechanical properties as all fibers throughout the full thickness of the component are oriented in the same direction (Figure 1-1a). Cross-ply CFRP utilizes several laminate layers stacked in a desired pattern, with the fibers within each laminate layer oriented in the same direction (Figure 1-1b). Fibers in woven composites are interlocked in a specified over-under pattern (Figure 1-1c); the exact specifications of the weave can vary depending on the application. This type of CFRP possesses the weakest properties since the fibers are not oriented completely horizontal. The weave pattern introduces slight vertical bending that can have a significant directional effect on mechanical properties. CFRPs derive strength and rigidity from the reinforcements, which possess tensile and stiffness properties many times greater than steel or aluminum alloys. Additionally, fiber configuration variability allows a high degree of design freedom to tailor properties to specific applications. Matrix properties are significantly weaker, which gives CFRPs their anisotropic structure and makes analysis and secondary processing notoriously difficult.

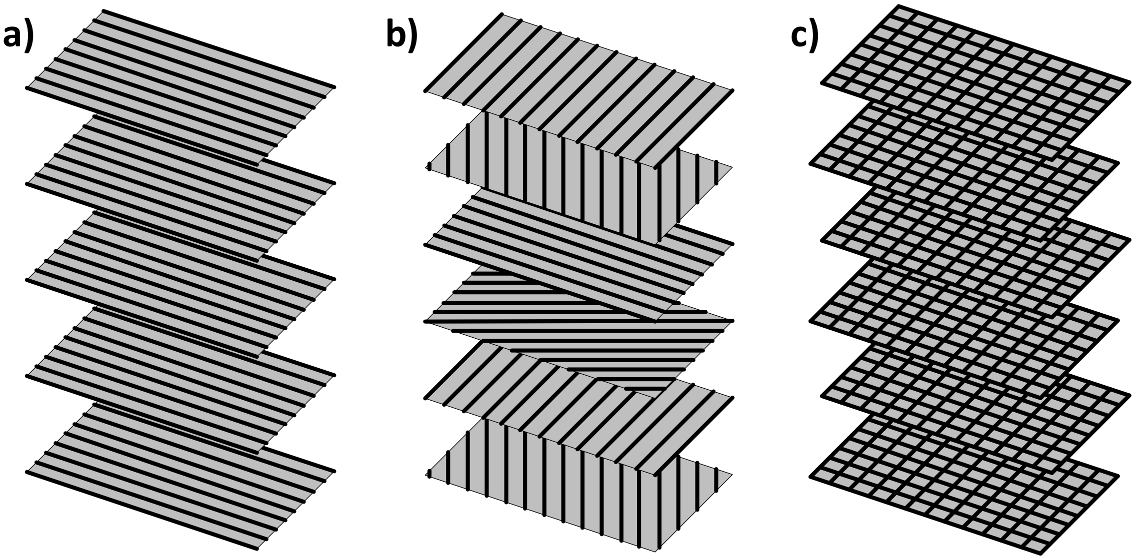

Figure 1-1: Illustration of the two main types of CFRP layups: (a) unidirectional, all fibers are aligned uniformly throughout (b) cross-ply, all fibers within single layer are aligned; (c) woven, fibers within each layer are interlocked.

Composite materials are used in many modern applications to reduce weight without sacrificing performance. CFRP components are approximately 70% and 30% lighter than an identical part made of steel or aluminum with up to 10 times the strength (Cherif, 2011), but can carry as much 20 times the cost (Meredith et al., 2015). Nonetheless, CFRPs have seen increased usage in industry in recent years, particularly in automotive and aerospace applications, as a lightweight high-strength alternative to traditional metals. Although CFRPs first appeared in the aerospace industry over 50 years ago, their utilization had not seen a dramatic increase until the 1990s. Modern airplanes from Airbus and Boeing are being designed with as much as 50% composites by total weight (M'Saoubi et al., 2015). The use of lightweight materials combined with advances in jet engine technology is estimated to yield a 15% decrease in fuel consumption and a 20% reduction in operational costs overall (Shyha et al., 2010). Figure 1-2 illustrates the extensive use of lightweight materials in the Airbus A380, the world's largest passenger airliner, released in 2007 and designed with 22% composites by weight (Hexcel Corporation, 2000). Automotive industry experts similarly project that the application of CFRP in mass-production could reduce vehicle weight by as much as 50% and improve fuel economy by up to 35% alone without any sacrifices in performance or safety (Mascarin et al., 2015). BMW recently entered a joint manufacturing venture with SGL (Reinforced Plastics, 2012). The passenger compartment of BMW's i3 compact hybrid, referred to as the "Life Module", is light enough to be lifted by hand, shown in Figure 1-3.

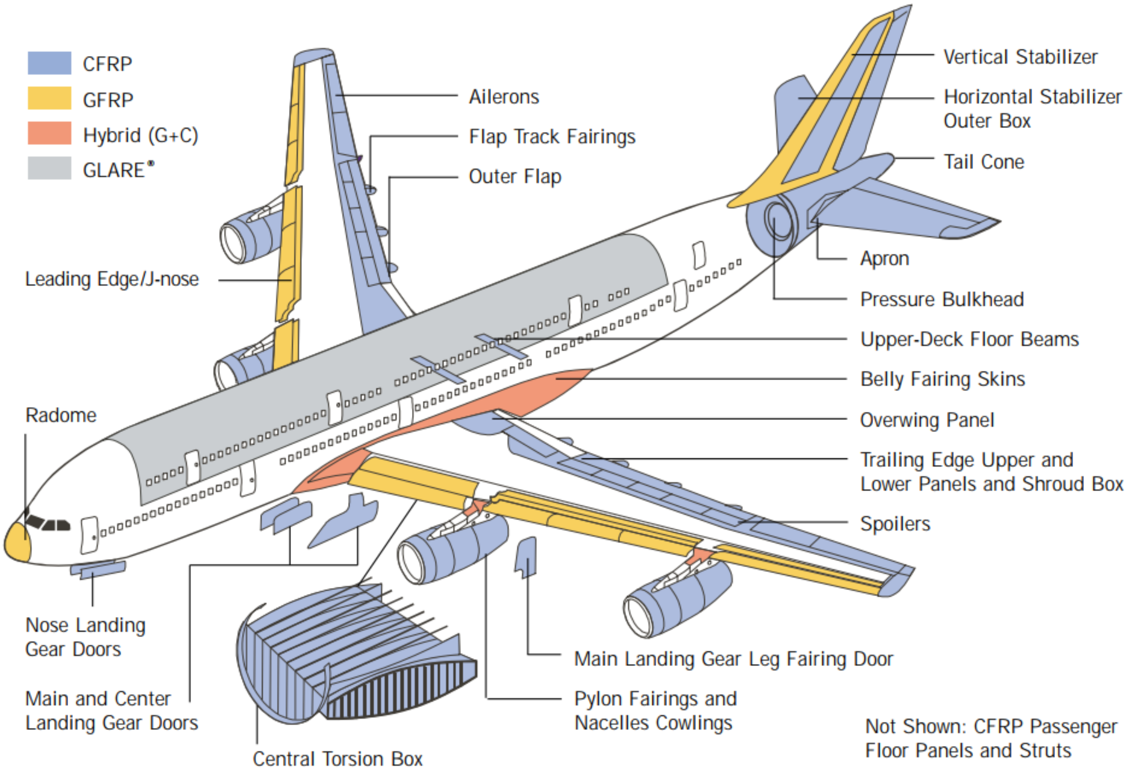

Figure 1-2: Schematic of the structural design of the Airbus A380 showing extensive usage of fiber-reinforced composites totaling 22% of total aircraft weight (Hexcel Corporation, 2000).

Figure 1-3: The “Life Module” of BMW’s i3 compact hybrid. Full carbon construction allows vehicle to achieve total curb weight of less than 3,000 lbs (EV World, 2013)

Cost is especially important in applications where small increases in component expense can significantly affect the viability of advanced materials for high-volume production. As an example, automotive manufacturers desire CFRP in the range of $5 per pound – significantly less than the current price of $10 to $15 per pound (Mazumdar et al., 2016). Although raw materials processing for CFRP production represents a significant portion of total cost, the price of secondary processes plays an important role. Despite CFRP components typically being created close to final shape and form, secondary processes are sometime required to create assembly features and to achieve final dimensions or tolerances. The industry standard is to assemble CFRP components using mechanical fasteners, such as rivets and bolts, as in traditional materials (Gaugel et al., 2016). The Boeing 787 “Dreamliner” requires drilled hole diameters within ± 0.018 mm to meet strict ISO 286 H8 tolerance (Gardiner, 2014). This makes high-quality drilling essential considering that the typical commercial airliner can contain over 1,000,000 fasteners, depending on aircraft size (Campbell, 2006). Conventional operations cause unacceptable machining damage and rapidly accelerate tool wear, necessitating premature tool replacement and causing an increased number of part rejections. As much as 60% of part rejections during final assembly in the aviation industry are due to machining errors alone (DAVIM et al., 2007). Non-contact laser machining is becoming a viable alternative, which uses a focused laser beam to remove CFRP material by ablation to avoid the detrimental effects of mechanical cutting force and tool degradation. The advantages of laser machining include the absence of physical tool contact, precise control of process parameters, and flexible high-speed path scanning for the creation of complex features. However, laser machining can introduce new issues of thermal damage related to anisotropic nature of the CFRP structure and significant differences in thermomechanical properties between the matrix and reinforcements.

1.1 Laser Ablation Process Overview

Laser machining of CFRP is defined as an ablation process, where the fiber-matrix structure is removed from the substrate by way of heating and evaporation of the matrix material and sublimation of the fiber reinforcements. The laser ablation process for can be divided into four stages: (1) optical absorption, (2) plasma ignition, (3) plasma expansion and cooling and absorption, and (4) particle formation and ejection (Russo et al., 2007).

1.1.1 Optical Absorption

During laser ablation, photon energy from the laser beam is absorbed within the target area at the workpiece surface. The surface absorptivity is characterized using the coefficient, α, which describes the fraction of light reflected by the material. This is dependent on the wavelength of laser irradiation and the material properties. Given the highly variable properties within the CFRP structure, fiber-matrix decomposition and subsequent phase changes are difficult to predict.

$$\mathrm{I(z)} = \mathrm{I_0 e^{-\alpha z}} \tag{1.1}$$

The intensity of the light decays once the irradiation penetrates below the workpiece surface, with the intensity being proportional to depth at a rate determined by α as a function of wavelength and temperature. This is shown by the Beer-Lambert Law in the Eq. 1.1, where intensity, I (z), decays exponentially with depth, z. The Beer-Lambert Law assumes constant α for initial intensity, I_0, just inside the surface. Absorptivity of CFRP is difficult to characterize due to non-homogeneity of material properties. Additionally, the effective absorption at the CFRP workpiece surface may be different than the absorption at a milled surface since most laser through-cutting operations require multiple laser scans (Xu and Hu, 2017).

1.1.2 Plasma Ignition

For pulsed laser ablation the absorption mechanisms during laser-material interaction are determined primarily by the emission wavelength, the power intensity, the pulse duration and frequency, and the thermalization time of the material, defined as the response time for the excited electronic states to transfer energy to phonons. In other words, the thermalization time is the time required for absorbed laser energy to manifest as a thermal response at the atomic level, which depends on the molecular properties of the material. For example, the thermalization time for most metals is on the order of 10^{-12} to 10^{-10} seconds. In the case of graphitic fiber reinforcements for CFRP, estimates by Kampfrath et al. (2005) and Ishioka et al. (2008) place the phonon response time at less than 1 picosecond (10^{-13} seconds). There is significant variation in the phonon response of non-metals, with thermalization times as long as 10^{-6} seconds. This is particularly relevant to CFRP in that many matrix epoxy resins and polymers fall in this range (Brown and Arnold, 2010), highlighting the variability in the predicted laser-CFRP interaction. The combination of pulse frequency and duration is generally referred to as the laser-induced excitation rate. When the laser-induced excitation rate is high (i.e. fast pulse frequency and/or short pulse duration) compared to the thermalization time, large excitations can build up in the intermediary states of the material. These excitation energies can be sufficient to break intermolecular bonds via photo-chemical ablation. Essentially, the laser excitation of the atomic structure outpaces the thermal response of the material. The material absorbs sufficient energy to break bonds directly, and is vaporized with very little temperature increase in the local substrate. This has important implications in CFRP laser machining since an isothermal photo-chemical ablation mechanism could drastically reduce thermal damage and improve machining quality.

When the laser-induced excitation rate is low (i.e. low pulse frequency and/or long pulse duration) compared to the thermalization time, the transient electronically-excited states become less significant. The atomic structure does not absorb sufficient laser energy relative to the thermal response of the substrate. The material response can then be characterized using a thermal framework, and is referred to as photo-thermal ablation. In this case, absorption of laser energy increases the temperature of the substrate, and well-defined phase transitions ensue. The absorbed laser energy may elevate the target material temperature, cause phase transformations, and eventually induce deep material removal from the target by conduction. The triple point of carbon occurs at approximately 11 MPa and 4,600 K (Zazula, 1997), and its critical point is approximately 7,000 K (Leider et al., 1973). The carbon fibers may be directly sublimated to the gas phase or converted to plasma during laser ablation, whereas the matrix material is melted and evaporated due to the heat absorbed by the fibers. For photo-thermal processing, the material response can be characterized using the heat equation derived from the conservation of energy and Fourier’s Law. The temporal and spatial evolution of the temperature field inside a material in a coordinate system that is fixed with the laser beam can be written according to Eq. 1.2 (Bogaerts et al., 2003).

$$\frac{\partial T(x,t)}{\partial t} = \frac{\partial}{\partial x}\left[\left(\frac{k}{c_p \rho}\right)\frac{\partial T(x,t)}{\partial t}\right] + \frac{\alpha}{c_p \rho} I(x,t) \tag{1.2}$$

In general, finding analytic solutions to this non-linear partial differential equation can be difficult. An important quantity that comes out of applying simplifying assumptions is the thermal diffusion length from Eq. 1.3.

$$L_T \approx \zeta \sqrt{\tau \frac{k\rho}{c_p}} \tag{1.3}$$

The thermal diffusion length, L_T, characterizes the area were significant temperature changes are experienced during a characteristic time, τ. Heat transfer before and after the laser pulse can lead to elevated temperatures and drastic changes in material properties. The region over which these changes occur is referred to as the heat-affected zone (HAZ), and is a common metric of quantifying CFRP laser machining quality. An example of this is shown below in Figure 1-4 from experimental results as a part of this research.

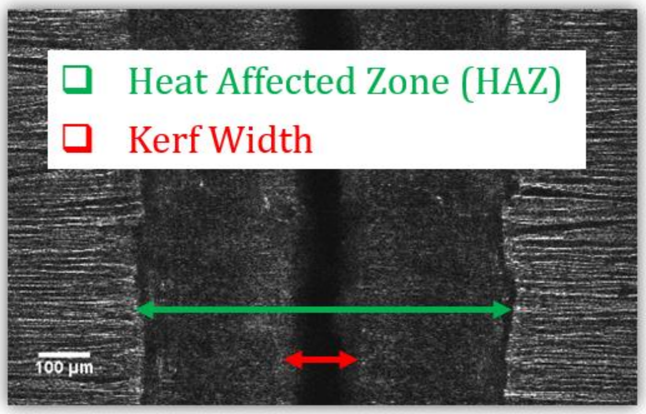

Figure 1-4: Example CFRP laser machining result showing the kerf and HAZ generated by laser ablation process. The HAZ includes areas where the matrix has been evaporated, melted, or re-solidified.

In the case of moderate laser-induced excitation rate (i.e. nanosecond pulse duration) and high power intensity (10^7 to 10^{11} W/cm^2), photo-chemical ablation can potentially co-exist with photo-thermal thermal mechanisms. Additionally, a third ablation mechanism is possible, either for laser irradiation with high photon energy relative to the bond energy of the material, or in the presence of ultra-sort laser pulses (10^{-13} to 10^{-15} seconds). In this case, the excited electrons of the solid may be removed directly and the ablation mechanism is classified as “photo-electric” (Steen (2003), Dutta Majumdar and Manna (2003)).

1.1.3 Plasma Expansion & Absorption

Some of the ablated CFRP material is converted into plasma with plume expansion related to the initial mass and energy in the vapor plume, and the surrounding gas environment. The expansion of the evaporated material plume and shockwaves can be described by the Euler equations in Eqs. 1.4-1.6 (Bogaerts et al., 2003).

$$\frac{\partial p}{\partial t} = -\frac{\partial(\rho v)}{\partial x} \tag{1.4}$$

$$\frac{\partial(\rho v)}{\partial t} = -\frac{\partial}{\partial x}\left[p + \rho v^2\right] \tag{1.5}$$

$$\frac{\partial}{\partial t}\left[\rho(E_d) + \frac{v^2}{2}\right] = -\frac{\partial}{\partial x}\left[\rho v\left(E_d + \frac{p}{\rho} + \frac{v^2}{2}\right) + \alpha_{IB} I\right] \tag{1.6}$$

In a vacuum, the plasma plume expands adiabatically with the expansion speed expressed as in Eq. 1.7 (Zel’dovich and Raizer, 2002). When ablation occurs in a non-vacuum, the ejected mass compresses the surrounding gas environment, producing shockwaves. Once the external shockwave is formed, its expansion distance can be described by Sedov’s theory. The expansion distance H, representing the location of the shockwave front, can be calculated as a function of time given in Eq. 1.8 (Sedov, 1993).

$$v_p = \sqrt{\frac{4\gamma+10}{3}\frac{E}{M_v}} \tag{1.7}$$

$$H = \lambda_0 (t)^{\frac{2}{2+D}} \left(\frac{E_0}{\rho_1}\right)^{\frac{1}{2+d}} \tag{1.8}$$

Part of the incoming laser energy is absorbed by the expanding plasma plume. Photon absorption by laser-induced plasma during the ablation process occurs primarily by the inverse Bremsstrahlung mechanism (Russo et al., 2007). Free electrons gain kinetic energy from the laser beam and during collisions among sample atoms and ions, electron, and gas species, which reduces the incident pulse energy at the target surface. The inverse Bremsstrahlung absorption coefficient is given by Eq. 1.9 (Russo et al., 2007).

$$\alpha_{IB} = \left[Q N_e N_0 + \frac{4e^6 \lambda^3 N_e Z^2 N_i}{3hc^4 m_e} \sqrt{\frac{2\pi}{3 m_e k_b T_e}} \right] \left[1 - e^{-\left(\frac{hc}{\lambda k_b T_e}\right)} \right] \tag{1.9}$$

Longer wavelengths promote Bremsstrahlung absorption, which lowers the ablation rate and increase the chances of elemental fractionation. This has been experimentally confirmed by Cabalín and Laserna (1998) and Thiyagarajan and Thompson (2012). Bremsstrahlung absorption in laser-induced plasma becomes important in two ways during laser ablation. First, laser-induced photoionization and optical breakdown of the gas environment above the target area can occur when the power intensity is sufficiently high. This intense plasma is highly absorptive, and can sufficiently reduce the incident power intensity absorbed by the workpiece to significantly affect the ablation rate. Secondly, for laser pulsing in the nanosecond time regime the later part of laser pulse can be absorbed by the expanding plasma plume to effectively "shield" the target area. This phenomenon is called plasma shielding, and intensifies with laser irradiance to reduce the ablation rate up to a saturation level (Borisov et al., 1998).

1.1.4 Particle Formation & Ejection

Nano-sized particles are formed from condensation of the vapor. Condensation starts when the vapor plume temperature reaches the boiling temperature of the material (~3000 K) and stops at the condensation temperature of the material (< 2000 K). Ejection of ablated materials is typically aided by an assist gas flow.

1.2 Review of CFRP Laser Machining Research

Contrary to mechanical machining of CFRP, laser machining is non-contact form of material removal with no measurable cutting force. Given the primarily thermal nature of the laser-material interaction, the interaction time between the beam and CFRP workpiece is extremely important. This is illustrated in Figure 1-5, showing the relationship between power intensity and interaction time for the vaporization limit of CFRP.

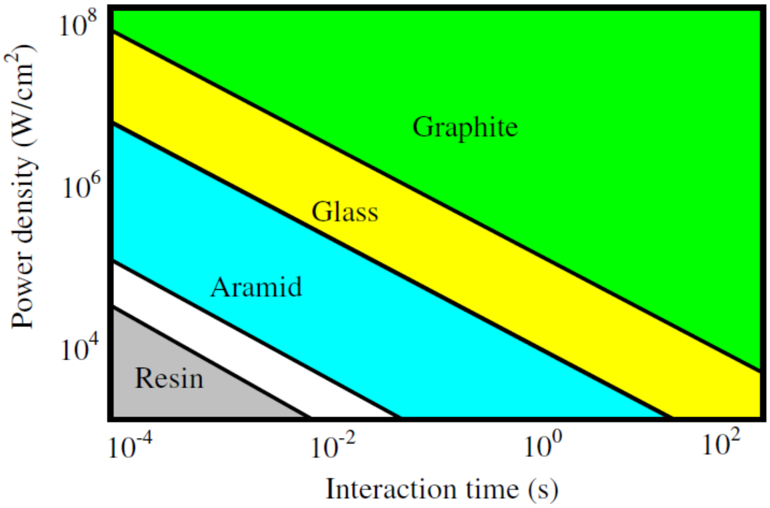

Figure 1-5: Vaporization limit conditions for laser machining of CFRP based on laser-material interaction time and applied power intensity. In particular, matrix resin (bottom-left) has much lower limit that graphitic fiber reinforcements (top-right) (Negarestani, 2010).

Non-contact laser machining is becoming a viable solution for high-speed machining of CFRP without the detrimental effects of mechanical cutting force and tool degradation. Although there has been significant study on laser source options and the effect of individual process parameters in the literature, there is potential for further investigation into specific material removal and energy absorption mechanisms.

A wide range of laser source options have been investigated by researchers. Salama et al. (2016b) employed a transversely-excited atmospheric-pressure (TEA) CO_2 laser. Tests showed minimal thermal damage, likely from increased matrix absorption at a wavelength of 10.6 µm. However, CO_2 lasers generate large spot diameters that produce wide kerfs, reduce power intensity, and limit the ablation rate. Jung et al. (2012) evaluated laser machining using a 1030 nm CW disk laser for both long- and short-fiber CFRP. Their tests showed significant HAZ expansion due to continuous laser-material interaction, and a subsequent reduction in tensile strength during high power and low scanning speed conditions. Leone et al. (2013) analyzed the CFRP removal mechanism and HAZ formation using a Q-Switched Yb:YAG fiber laser working at a pulse duration of 50 ns with low pulse energy (0.2-1.0 mJ). Li et al. (2010) investigated laser machining quality with a Nd:YVO_4 and claimed a HAZ width of only 50 µm using 25 ns pulses. (Mathew et al., 1999) performed CFRP machining experiments using a high-energy Nd:YAG laser system. Relatively long pulse duration in the range of 0.2-1.0 ms produced widespread matrix recession and charring.

In general, UV lasers are able to achieve slightly better results than IR lasers. Anzai et al. (2014) came to this conclusions by comparing trepanning performance using a prototype dual-beam scanning system with a CW single-mode NIR fiber laser and an ns-pulsed UV laser. Similarly, (Fujita et al., 2016) compared different combinations of pulse duration (fs to ns) and wavelength (266 nm to 1064 nm). Takahashi et al. (2016) directly compared CFRP laser machining at 266 nm and 1064 nm with a Q-Switched Nd:YAG laser, and concluded that matrix absorptivity was a key factor in determining machined surface integrity. The matrix material is largely transparent in the NIR spectrum. Therefore, laser irradiation passes through the matrix and is absorbed by the fibers, indirectly heating the matrix by conduction and causing fiber pull-out and HAZ extension. Conversely, UV irradiation is absorbed by the matrix directly. Wolynski et al. (2011)investigated three laser wavelengths (355 nm, 532 nm, 1064 nm) to estimate the ablation threshold by extrapolating measurements for ablated width over a range of laser fluences. The calculated threshold increased with wavelength, with the volumetric ablation rate also being 25% lower for 355 nm than for 1064 nm. Given the transparency of the CFRP matrix for the NIR spectrum, it was postulated that the penetration depth of the laser irradiation would be greater since a portion of UV laser energy is absorbed by the matrix according to Beer's Law. Additionally, the photon energy for UV wavelengths is sufficient to directly break the intermolecular bonds of the carbon-based fiber reinforcements. Therefore, there is a much greater chance of achieving photo-chemical ablation rather than photo-thermal. This effect, combined with increased absorptivity of the CFRP matrix in the UV spectrum, leads to significant reduction in HAZ. This was experimentally confirmed by Denkena et al. (2007), Emmelmanna et al. (2011), Niino and Kurosaki (2011), and Sato et al. (2013), who all found more favorable results using shorter laser wavelengths. Similarly, Völkermeyer et al. (2011) and Fischer et al. (2010) proposed using UV lasers to achieve layer-by-layer removal of CFRP material for repair techniques. However, UV lasers are typically much more expensive than more common IR laser, particularly Nd:YAG systems, and operate with low pulse energy to limit the ablation rate.

It is generally agreed that the use of inert assist gases in CFRP laser machining reduces thermal damage by limiting exothermic oxidation reactions, while reactive gases promote fiber-matrix decomposition and enhance the material removal process. An early study by Lau et al. (1990) showed that an Argon gas flow in CFRP laser cutting produced cleaner edges and reduced the thermal damage ratio. Rodden (2002) illustrated the effect of inert assist gas on plasma formation and HAZ expansion using a long pulse NIR Nd:YAG laser for CFRP drilling experiments. Likewise, Riveiro et al. (2012) improved the CO_2 laser cutting process for CFRP by using an Argon assist gas flow to decrease the HAZ width. Negarestani et al. (2010) evaluated the effect of mixed reactive for CFRP laser cutting using a nanosecond Nd:YAG laser, and observed enhanced machining performance in the partial presence of oxygen. Similarly, (Kononenko et al., 2014) conducted CFRP laser machining experiments to compare the effect of pure oxygen and nitrogen gas flows. During multi-pass cutting using a near-UV ultrafast laser system, they found that oxygen enhanced the ablation rate while a standard air environment produced increased deformation. French et al. (2010) compared N_2 and CO_2 assist gases using a long duration (0.3-0.5 ms) laser system at high pulse energy (1.8 J to 6.0 J). They reported improved drilling quality with less surface debris using CO_2 assist gas, and postulated the Joule-Thompson effect was responsible.

Due to the thermal nature of the process, traditional surface roughness metrics are insufficient to quantify CFRP laser machined surface quality. Analysis of surface integrity using SEM imaging is important beyond HAZ formation at the workpiece surface. Voisey et al. (2006) analyzed fiber swelling during laser percussion drilling of CFRP using a 1.06 µm Nd:YAG laser system. SEM imaging revealed radial swelling as high as 60% for fibers near the drilled wall, attributable repeated energy absorption during each additional laser pass. The authors used Raman spectroscopy to conclude that removing impurities through the use of heat-treated T300 PAN-based fibers reduced fiber swelling. It is also possible that the swelling mechanism was the result of inelastic thermal expansion from energy absorption due to the high pulse energy (1.0 J) over long pulse duration (1.0 ms). (Fuchs et al., 2013) noted a similar effect using a continuous-wave NIR Yb:YAG fiber. Fiber ends near at the wall surface swelled and combined with re-solidified matrix material to become fused. Similarly, matrix recession near the internal wall surface was observed by Takahashi et al. (2016) during NIR laser machining. Theoretically, this could lead to cracking and compromise the fatigue life of the CFRP structure. Li et al. (2008) analyzed the CFRP microstructure for multi-ring laser drilling using a high power Q-Switched Nd:YVO_4 DPSS UV laser system and also saw evidence of “cracking” and voids in the local fiber-matrix structure. The multi-ring scanning technique led to heavily-modified surface integrity along the multi-ring profiles.

Due to µm-scale for laser machining parameters, optical limitations play are critical for optimizing precision laser machining operations for CFRP. Herzog et al. (2016), Takahashi et al. (2015), and Ushida et al. (2012) studied various laser focusing strategies, and found that shadowing effects at the groove entry limit the machining depth for CFRP of high thickness. Herzog et al. (2016) proposed a linear relationship between the numbers of laser passes and cutting depth; this claim has not been researched extensively. Salama et al. (2016c) described an additional limiting characteristic related to the reflectance of laser light from a machined CFRP sidewall, which was calculated to increase with taper angle. Therefore, the shape of the machined profile becomes important for analyzing the effective laser ablation rate and deploying a scanning strategy. All three studies proposed the use of multi-ring and hatching strategies to alleviate optical limitations. Gaussian beam distributions have potential consequences for deep drilling. As the laser gradually de-focuses, holes take on a conical shape due to tapering. Romoli et al. (2012) showed that re-focusing as the laser progresses through the material thickness can help resolve this issue.

Statistical analyses have attempted to correlate process parameters to optimize using parametric analyses, such as Analysis of Variance (ANOVA). (Salama et al., 2016b) performed ANOVA on CFRP laser machining to minimize the HAZ width and maximize both the machining depth and ablation rate, with HAZ reduction of highest priority. The statistical analysis predicted optimized values that were most significantly affected by laser fluence, scanning speed, and pulse frequency. Leone et al. (2014) used ANOVA to analyze the effect of process to determine the number of laser scans required to cut through 0.5 mm thick CFRP laminates using a MOPA Q-Switched Yb:YAG fiber laser. Similarly, they found that pulse energy and scanning speed were of the most significance; ANOVA predicted a minimum of 4.2 scans would be achieved by scanning at 50 mm/s with a pulse energy of 0.75 mJ. Mathew et al. (1999) used response surface methodology (RSM) to evaluate interactions for theoretically better optimization of the CFRP laser machining process. RSM found that thermal properties and fiber volume fraction were the principle factors in determining cutting performance. Optimization of laser cutting parameters was shown to reduce the HAZ width to 78 µm for 1.4 mm thick CFRP sample using 12-16 passes with a 30 kW NIR Yt:YAG fiber laser by Herzog et al. (2015). Other studies have proposed algorithms to suitably balance process parameters for acceptable machining quality. Examples of such processing regimes were postulated by (Leone et al., 2009) using a millisecond 1064 nm Nd:YAG laser with pulse energy from 0.33 J to 0.69 J.

Researchers have attempted to numerically model the laser ablation process in an effort to optimize the amount of energy delivered for HAZ reduction. Transient computer simulations for laser ablation non-melting materials have been developed, as in (Modest, 1996). However, there is significant difficulty in accounting for the anisotropic structure of; characterization of the process is difficult given the complex nature of laser-CFRP interaction. Studies have proposed simplified thermodynamic models [Cenna, Mathew]. A 1-dimensional (1D) “perpendicular heat flow” model based on energy balance was proposed by (Weber et al., 2011) to predict the minimum thermal damage possible for CFRP laser machining. This model was validated by experiments executed by (Mucha et al., 2014), which also estimated residual conduction losses in the evaporated matrix and remaining bulk material. These concepts were extended to a “heat accumulation” model by (Weber et al., 2012) to determine temperature distributions that would lead to CFRP material removal by photo-thermal laser ablation. Temperature distributions were calculated for an ultrafast near-UV laser system at two different pulse frequencies, and were confirmed experimentally by measuring the HAZ width.

Finite element models have been developed with varying degrees of success. Wu et al. (2015) compared the temperature distributions for continuous wave and pulsed laser ablation and found agreement with experimental results. Similarly, Ohkubo et al. (2014) numerically simulated the combustion and decomposition of CFRP through oxidation using thermo-gravity differential thermal analysis (TG-DTA). They also applied a finite difference method to compute heat transfer and subsequent HAZ formation, and experimentally confirmed their findings using nanosecond NIR laser system.

Researchers have attempted to correlate the laser ablation rate to process parameters in an attempt to measure the ablation threshold, but results have been inconsistent. High performance laser drilling of CFRP using a high-frequency ultrafast-pulsed NIR laser system was demonstrated by Salama et al. (2016a). Thermal damage was significantly reduced, but at the expense of processing time; 500 laser passes were required to drill through a 2 mm thick CFRP sample. This is likely due to the low ablation rate (~15 nm/pulse) that is typical of ultrafast-pulsed laser systems as a result of low pulse energy (< 1 mJ). Wolynski et al. (2011) estimated the threshold fluence of CFRP to be approximately 0.410 J/cm^2 for 1064 nm wavelength using 10 ps pulses by extrapolating the ablated width. Hoffman et al. (2014) proposed a slightly higher estimate of 0.52 J/cm^2 for graphite using longer 10 ns pulses, also at a wavelength of 1064 nm, by extrapolating the observed ablation rate. Lednev et al. (2013) reported the laser ablation threshold of carbon nanotubes to be only 50 mJ/cm^2 using a nearly identical 1064 nm laser. As such, the exact relationship between the CFRP ablation rate and laser irradiance is not clear. An alternative for characterizing laser materials processing was originally proposed by Beal et al. (2009) and applied to the CFRP laser machining process by Romoli et al. (2012). Energy density is a measure of total laser energy delivered to a laser scanned area (Eq. 1.10).

$$\mathrm{ED}\ [\mathrm{J/mm^2}] = \frac{\mathrm{P_{avg}}}{\mathrm{v \cdot d}} \qquad (1.10)$$

All relevant pulse and scanning properties are accounted for, with average laser power, P_{avg}, laser scanning speed, v, and laser spot diameter, d. Traditional parameters, such as laser fluence and power density, quantify pulse energy or peak laser power delivered per unit area, respectively. Using a high frequency Q-Switched Nd:YAG UV laser, Romoli et al. (2012) calculated the threshold energy density of Toray T300 fibers to be 0.58 J/mm^2, two orders of magnitude lower than threshold fluence estimates. Energy density has not been used extensively in studying laser machining of CFRP, and offers flexibility to compare laser systems over a wide range of process parameters.

1.3 Research Objectives and Outline

Laser machining of CFRP using a high-energy nanosecond laser source has not been well studied in the literature, particularly high-energy long-duration nanosecond pulsing at low frequency. The primary objective of this research is to develop a better understanding of the laser ablation process for CFRP by analyzing the performance of two laser systems for two different CFRP materials. In particular, the physiochemical nature of the material removal and energy absorption mechanisms is addressed as it relates to CFRP laser machining quality. The secondary objective of this research is to compare and contrast laser machining as an alternative to mechanical machining for CFRP and to analyze the effect of individual process parameters on machining performance. The effects of process parameters are evaluated for single-pass line cutting using both cross-ply and woven CFRP. Surface integrity analysis is carried out for through cuts obtained by multi-pass line cutting and contour cutting.

Conventional machining of CFRP is investigated in Chapter 2 to establish baseline results. Laser machining is conducted first using a CW/modulated Yb:YAG NIR fiber laser system in Chapter 3 and later using a NIR high-energy nanosecond-pulsed Nd:YAG laser system in Chapter 4. The results of all three machining systems are discussed in Chapter 4. Lastly, Chapter 5 draws final conclusions regarding the overall contributions of this research and possible future work.

CHAPTER 2.

MECHANICAL DRILLING EXPERIMENTS FOR CFRP

2.1 Introduction

Mechanical machining is a popular approach for CFRP processing, maintaining dominance as the primary processing method across a wide range of applications (Negarestani, 2010). Conventional machining processes (i.e. orthogonal cutting and drilling) are preferred for cost reduction and increased productivity (Lopresto et al., 2016). Although there been significant research into mechanical machining, particularly for traditional materials, challenges remain in adapting and optimizing the process for CFRP due to complexity of material structure and properties.

Mechanical machining of CFRP can cause rapidly accelerated tool wear, increased surface roughness, delamination, burring, and poor tolerances adherence for machined features. Cutting mechanisms for CFRP are increasingly complex due to non-homogeneity, and have been previously examined by researchers (Teti, 2002). Abrasive tool contact results in local stress concentrations in a cyclic loading pattern. Although CFRP possesses very high elastic moduli, it is virtually inelastic with as little as 0.5% strain-to-failure and is susceptible to cracking once mechanical strength has been exceeded (Han et al., 2016). This shows brittle failure mechanics with uneven fatigue life and unpredictable endurance limits due to the variability of the fiber-matrix structure. The primary fracture method is inter-laminar cracking due to de-bonding failure of the fiber-matrix system and delamination. In mechanical machining, the downward thrust force in the axial cutting direction generates delamination at the entry and exit surfaces for cross-ply and unidirectional CFRP while shear stress along the tool contact patch causes peeling and burring in woven samples. Ho-Cheng and Dharan (1990) developed a linear elastic fracture mechanics model that determined that delamination occurs once loading from the thrust force exceeds the inter-laminar fracture toughness. An illustration of delamination at both entry and exit surfaces is shown in Figure 2-1. Tool geometry can significantly reduce the thrust force, which is critical to improving machining quality. Threshold values for positive rake angles and clearance angles, as well as rounding and chamfering of cutting edges, can virtually eliminate delamination, enhance tool life, and finish quality (Koplev et al., 1983). Split-point drill bits can effectively "split" the central point tip of the drill bit using a secondary cutting edge, reducing the thrust force. This prevents de-centering of the tool, known as "walking", and reduces the thrust force by flattening the tool tip similar to the concept of orbital drilling as discussed by Sadek et al. (2012). Additionally, the chisel edge is removed, which was found to reduce delamination at the exit surface by Hocheng and Tsao (2006).

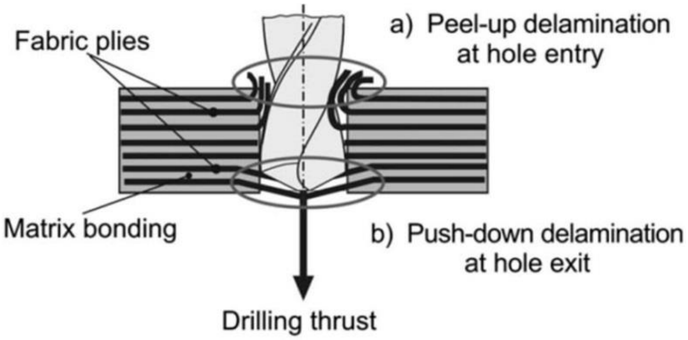

Figure 2-1: Illustration of delamination in mechanical drilling of CFRP: (a) shear chip formation at entry surface pushes separated CFRP material through the tool cutting flutes, causing peel-up delamination; (b) axial thrust force pushes downward on the exit surface, bending bottom laminate layers until fracture (Faraz et al., 2009).

Tool life is very important in CFRP mechanical machining. Increased wear reduces the sharpness of cutting edges, increases thrust force, and exacerbates the extent of delamination (Rawat and Attia, 2009). If the tool is severely degraded, machined features may exceed acceptable tolerances. Tool wear in CFRP machining primarily consists of abrasive wear, chipping, and adhesion, with abrasion seen as the predominant mechanism due to the properties of fiber reinforcements (Gaugel et al., 2016). Proper tool selections and coatings can provide important advantages. In general, high-speed steel drills (HSS) do not provide satisfactory performance. Tungsten-carbide drills can provide satisfactory drilling quality, but typically only for a limited number of holes. Murphy et al. (2002) found that the H8 tolerance criteria was exceeded after just 6 holes using uncoated WC tools due Polycrystalline diamond (PCD) coating significantly improves tool wear for high-speed milling [39-41]. Diamond-coated carbide tools demonstrated a significant improvement in tool life compared to non-coated tools (Iliescu et al., 2010). Brazed CVD diamond tools outperforms even the best-performing PCD tools by as much as 200-300% (Köpf et al., 2006). In mechanical milling of CFRP, cutting paths that are aligned with the fiber orientation ($\theta = 0°$) result in better surface integrity, with little to no significant cracking and a smoother surface finish (Ramulu, 1997). Damage increases as the angle θ increases, with fibers oriented for 90°-135° producing deep cracking along the fiber-matrix interface (Pecat et al., 2012) (Rentsch and Mamedov, 2012). Higher feed rates produce significant levels of fiber pullout and delamination, and increase surface roughness (Kim et al., 2005). Higher feed rates increase thrust force, causing more surface delamination; higher spindle speeds increase surface roughness, but decrease delamination (Rawat and Attia, 2009). The combination of high feed rates with high spindle speeds substantially decreases machining quality and accelerates tool wear (König and Graß, 1989). In testing, Attia et al. (2011) compared ultra-high speed (UHS) and high-speed drilling (HSD) to evaluate tool wear and found that UHS reached critical wear after just 20 holes while at HSD reached such levels after as many as 500 holes.

In this chapter, CFRP mechanical drilling experiments are performed using a CNC mill. The results of the experiments will be used to gain an understanding of how CNC parameters affect machining quality and establish a baseline for comparison with CFRP laser machining results in later sections. The effects of spindle speed, feed rate, tool geometry, and diamond coating are investigated for cross-ply IM7 and woven AS4 CFRP.

2.2 Experiments

2.2.1 Experimental Setup

Drilling experiments were carried out using a Haas Tool Room TM-1P machining mill. Maximum spindle speed is 6,000 RPM and maximum cutting speed is 400 inches per min. Two different Kennametal tools are used, shown in Figure 2-2: standard twist drill (DAL) and split-point fiber (SPF) drill. Both tools are made of solid carbide; the DAL drill is uncoated solid carbide and the SPF drill is solid carbide with a KDV400-Grade CVD multi-layer diamond coating. Thrust force is was measured using a Kistler 9257B dynamometer and signal amplifier sampling at a frequency of 1,000 Hz. Visual results were analyzed using an optical microscope and digital camera. The axial cutting speed is calculated using Eq. 2.1.

$$\mathrm{v} = \mathrm{Rotational\ Feed\ Rate} \cdot \mathrm{Spindle\ Speed} = \mathrm{F_R} \cdot \mathrm{N} \qquad (2.1)$$

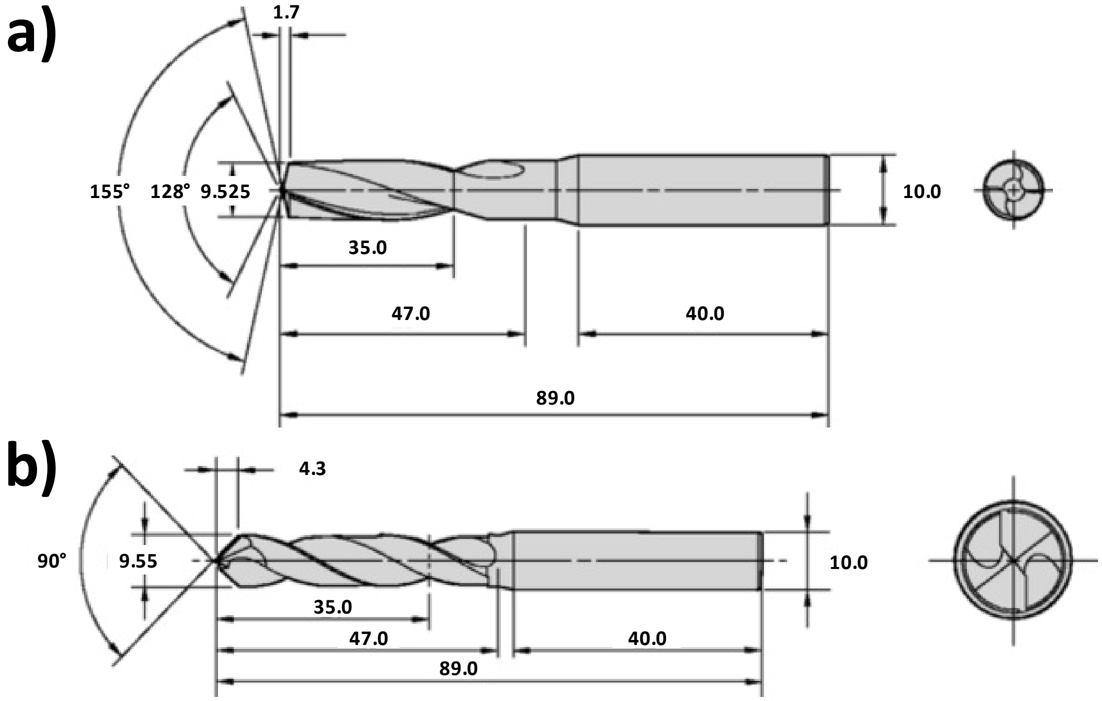

Figure 2-2: Diagram of Kennametal solid carbide tools used in CFRP drilling experiments: (a) DAL-series non-coated standard twist drill with 155° point angle and 9.525 mm nominal diameter; (b) SPF-series CVD diamond-coated twist drill with 90° point angle and 9.55 mm nominal diameter.

Table 2-1: Summary of thermomechanical properties for Hexcel HexTow® fibers used in CFRP laser machining experiments.

Property	**HexTow® IM7** (Hexcel, 2014a) **(for cross-ply CFRP)**	**HexTow® AS4** (Hexcel, 2014b) **(for woven CFRP)**
Fiber Diameter (µm)	5.2	7.1
Carbon Content (%)	95	94
Tensile Strength (MPa)	5515 - 5655	4410 - 4620
Failure Elongation (%)	1.9	1.7 - 1.8
Conductivity (W/m·K)	5.4	6.8
Specific Heat (J/kg·K)	879	1130
Mass Density (kg/m$^{3)}$	1780	1790

The CFRP materials used are manufactured by Hexcel Corporation and Cytec Industries and are employed in state-of-the-art designs by industry-leading aerospace companies [58]. Hexcel's HexTow AS4 and IM7 fibers are both high performance, intermediate modulus, PAN-based fibers (Table 2-1). Both possess excellent tensile and shear strength. Cytec's CYCOM 977-3 is a toughened, two-part epoxy system specially designed for primary and secondary aerospace structure applications where impact resistance during hot and wet conditions is critical (Table 2-2).

Table 2-2: Summary of mechanical strength and fatigue properties for Cytec CYCOM 977-3 epoxy system and HexTow CFRP. Properties are measured at room temperature.

Property	**Cytec CYCOM® 977-3**	**HexTow® IM7 12K (with 977-3 epoxy)**	**HexTow® 5HS AS4 6K (with 977-3 epoxy)**
Compression Yield (MPa)	186	-	-
Flexural Strength (MPa)	144	-	-
Flexural Modulus (GPa)	3.8	-	-
Critical Strain Energy (J/m^2)	217	-	-
Fracture Toughness (MPa·m$^{1/2}$)	0.9	-	-
Tensile Strength (MPa)	-	2510	869
Tensile Modulus (GPa)	-	162	68
Inter-Laminar Shear (MPa)	-	128	90

2.2.2 Experiment Design

Experiments for mechanical machining tests were designed to investigate the effects of three parameters: (1) constant cutting speed, (2) constant rotational feed rate, and (3) constant spindle speed. Test parameters are summarized in Table 2-3. The effect of spindle speed is investigated for both tool types. Spindle speed is first varied from 1,000

RPM to 6,000 RPM for a constant axial cutting speed of 6.0 in/min using cross-ply IM7 CFRP. Spindle speed is then varied again over the same range for a constant rotational feed rate of 0.0015 in/rev for woven AS4 CFRP, which is the value recommended by Kennametal. Finally, cutting speed was varied between 2.00 in/min and 10.00 in/min for woven AS4 CFRP to produce a constant spindle speed of 4,000 RPM, which is the value recommended by Kennametal.

Table 2-3: Summary of tests investigating effects of spindle speed for constant axial feed rate for cross-ply IM7 CFRP. Tests were executed using both drilling tools.

Spindle RPM	**Rotational Feed [in/rev]**	**Rotational Feed [μm/rev]**	**Axial Cutting Speed [in/min]**	**Axial Cutting Speed [mm/s]**
1000	0.0060	152	6.00	2.54
2000	0.0030	76.2	6.00	2.54
3000	0.0020	50.8	6.00	2.54
4000	0.0015	38.1	6.00	2.54
5000	0.0012	30.5	6.00	2.54
6000	0.0010	25.4	6.00	2.54
1000	0.0015	38.1	1.50	0.64
2000	0.0015	38.1	3.00	1.27
3000	0.0015	38.1	4.50	1.91
4000	0.0015	38.1	6.00	2.54
5000	0.0015	38.1	7.50	3.18
6000	0.0015	38.1	9.00	3.81
4000	0.0005	12.7	2.00	0.85
4000	0.0010	25.4	4.00	1.69
4000	0.0015	38.1	6.00	2.54
4000	0.0020	50.8	8.00	3.39
4000	0.0025	63.5	10.0	4.23

2.3 Results & Discussion

2.3.1 Constant Cutting Speed

Figure 2-3 and Figure 2-4 illustrate the difference in tool design between the SPF and DAL drills for cross-ply IM7 CFRP. For both tools, absolute maximum cutting forces are observed as the primary cutting edges engages with the CFRP exit surface (Figure 2-3b and Figure 2-4b). The elapsed time from points (a) to (b) for both figures is approximately 0.87 seconds, which is equal to the time required for the tool to penetrate through the 2.2 mm thick sample at an axial cutting speed of 6.0 in/min. Figure 2-5a compares the maximum cutting force measured for both tools for different spindle speeds at an axial cutting speed of 6.0 in/min. As spindle speed increases from 1,000 RPM to 6,000 RPM, the thrust force decreases from 137 N to 77 N for the SPF drill and from 151 N to 53 N for the DAL drill. Figure 2-5b gives a comparison of maximum primary and secondary cutting forces for the SPF drill. Compared with the DAL drill, the SPF drill produces a local maximum cutting force as the secondary cutting edge engages (Figure 2-3c). Increasing the spindle speed over the same range decreases the secondary thrust force force from from 40 N to 11 N.

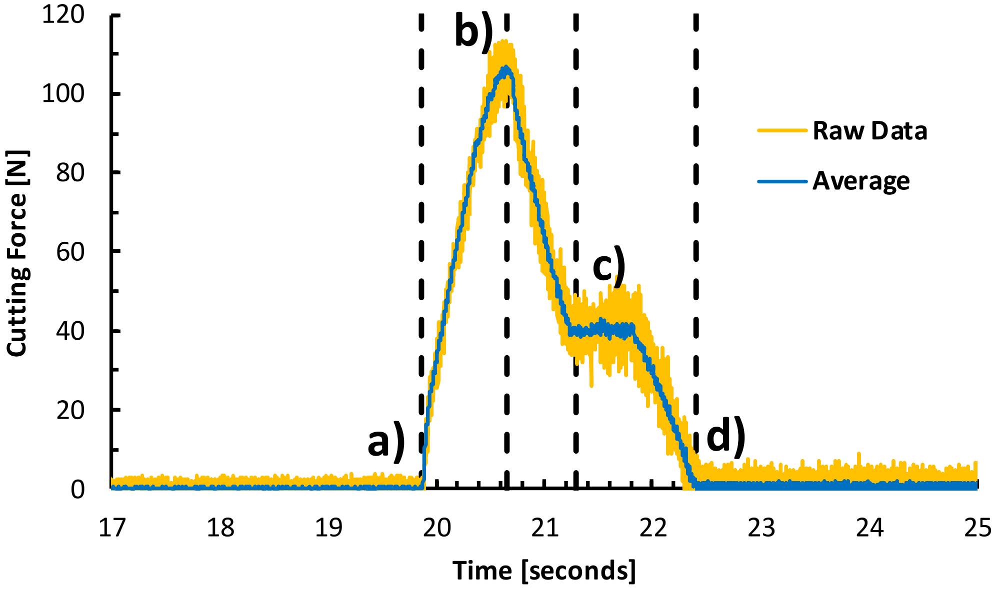

Figure 2-3: Cutting force progression measured by dynamometer in axial direction for CFRP drilling at 2,000 RPM and 6.0 in/min cutting speed using SPF drill: (a) drill point contacts entry surface; (b) maximum as drill point reaches exit surface; (c) local maximum as secondary cutting edge reaches exit surface; (d) tool exits material.

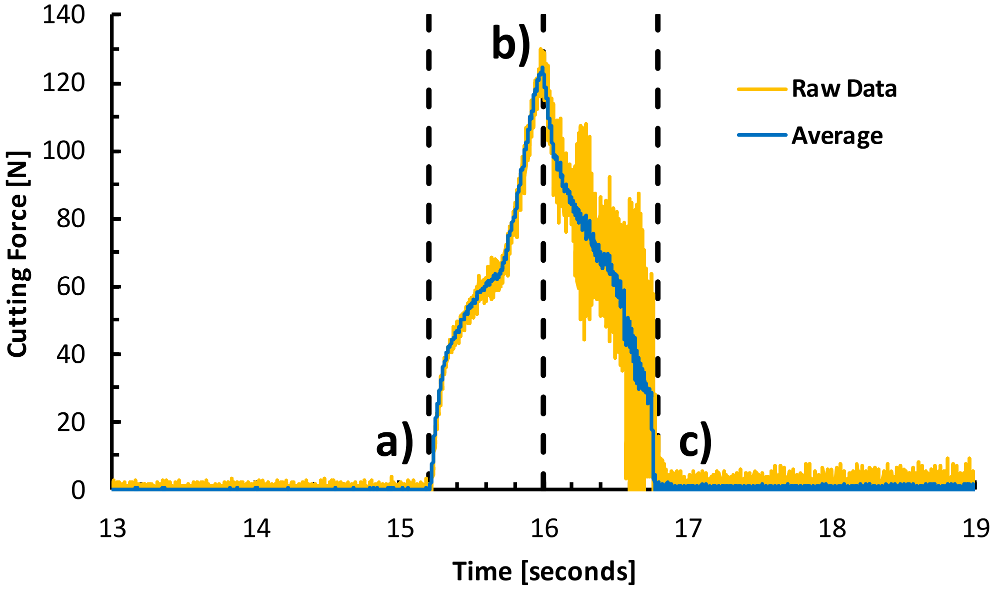

Figure 2-4: Cutting force progression measured by dynamometer in axial direction for CFRP drilling at 2,000 RPM and 6.0 in/min cutting speed using DAL drill: (a) drill point contacts entry surface; (b) maximum as drill point reaches exit surface; (c) tool exits material.

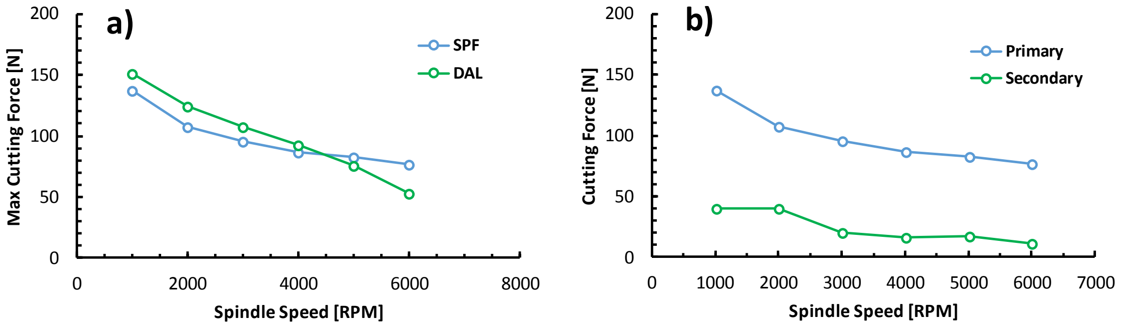

Figure 2-5: Cutting force comparisons measured by dynamometer in axial direction for drilling at varying RPM and 6.0 in/min axial feed rate: (a) Maximum primary cutting forces for SPF and DAL drills (point (b) in Figure 2-3 and Figure 2-4); (b) Comparison of primary and secondary cutting forces for SPF drill (points (b) and (c) in Figure 2-3).

Rotational feed rate is dependent on both spindle speed and axial cutting speed; as spindle decreases, rotational feed rate decreases for constant cutting speed. Therefore, it can be deduced from Figure 2-5 that the rotational feed rate is the primary factor in determining thrust force and machining quality. Figure 2-6 and Figure 2-7 compare entry and exit delamination at both spindle speeds for the SPF and DAL drills, respectively. The SPF drill shows an improvement in exit delamination while the DAL drill shows an improvement in entry delamination. From visual inspection, it was observed that the SPF drill produced a rougher internal surface than the DAL drill at 6,000 RPM. Additionally, chip size increased as spindle speed was decreased for both drills.

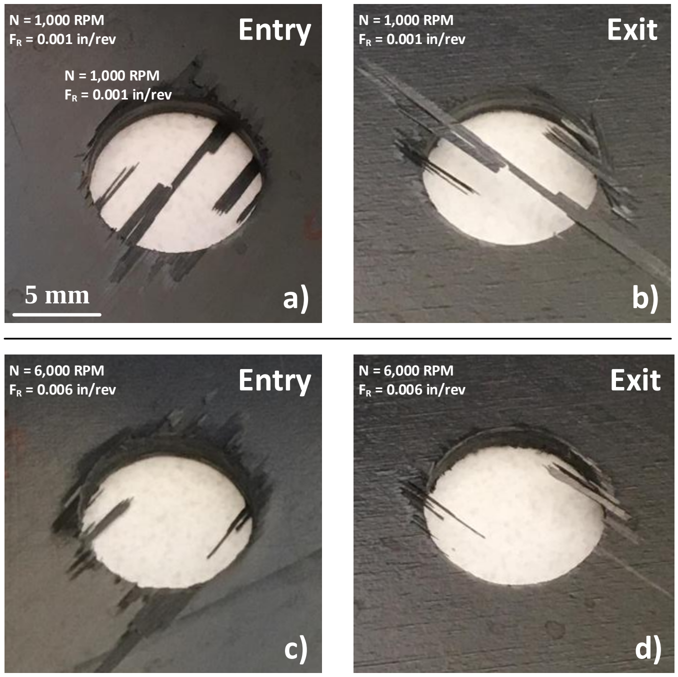

Figure 2-6: Surface imaging of CNC drilling for cross-ply CFRP using an SPF drill (V = 6.0 in/min): (a) and (b) entry and exit surfaces, respectively, for 1,000 RPM and 0.001 in/rev; (c) and (d) entry and exit surfaces, respectively, for 6,000 RPM and 0.006 in/rev.

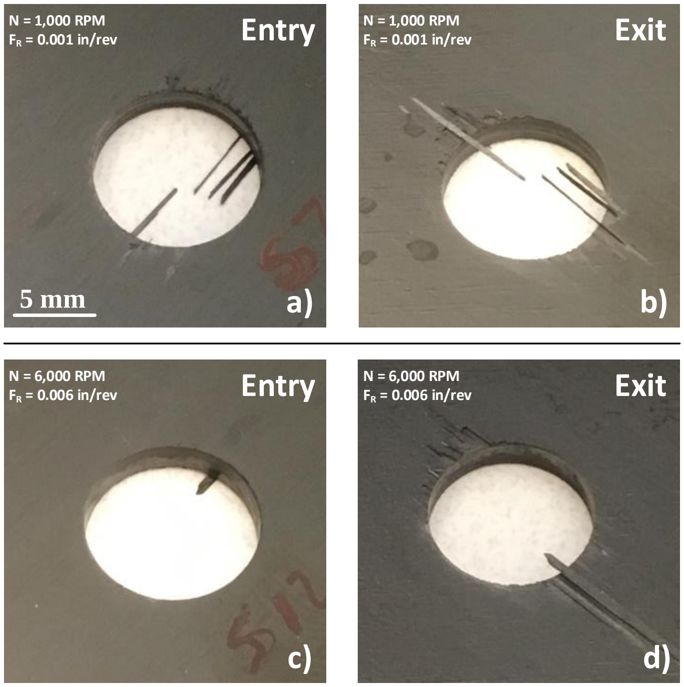

Figure 2-7: Surface imaging of CNC drilling for cross-ply CFRP using a DAL drill (V = 6.0 in/min): (a) and (b) entry and exit surfaces, respectively, for 1,000 RPM and 0.001 in/rev; (c) and (d) entry and exit surfaces, respectively, for 6,000 RPM and 0.006 in/rev.

2.3.2 Constant Rotational Feed Rate

Figure 2-8a compares the maximum cutting force measured for both tools for woven AS4 CFRP. The results were obtained for the same range of spindle speeds (1,000-6,000 RPM) at rotational feed rate of 0.0015 in/rev. The results show that thrust force is not affected by increasing spindle speed, which supports the results from Figure 2-5 that suggest that rotational feed rate determines the thrust force and therefore machining quality. Cutting force increased slightly from 74 N to 79 N for the SPF drill and from 123 N to 137 N for the DAL drill. Figure 2-8b shows a similarly small effect on the maximum primary and secondary cutting forces for the SPF drill. Likewise, spindle speed had a negligible effect on machining quality at both surfaces for the DAL drill in Figure 2-9. Increasing the spindle speed from generated more slightly more damage at the entry surface for the SPF drill (Figure 2-10). As seen in previous tests, 1,000 RPM produced better machined surface quality than 6,000 RPM using the SPF drill; DAL surface roughness was not affected. The effect of spindle speed on chip size was observed once again.

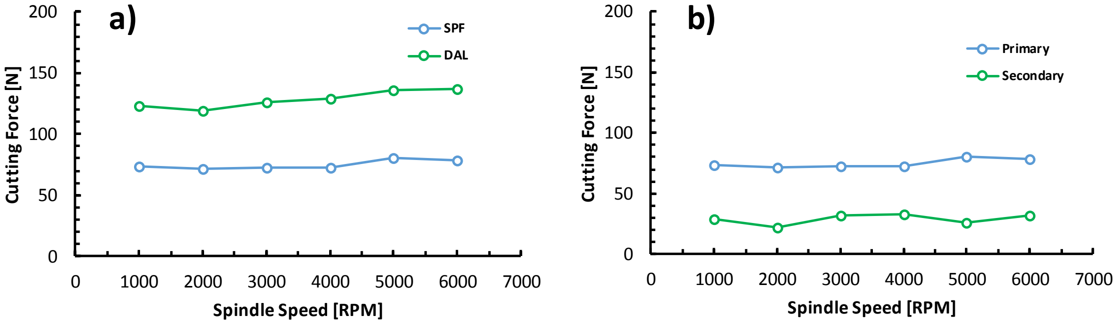

Figure 2-8: Cutting force comparisons measured by dynamometer in axial direction for drilling at varying RPM and 0.0015 in/rev rotational feed rate: (a) Maximum primary cutting force for SPF and DAL drills; (b) Comparison of primary and secondary cutting forces for SPF drill.

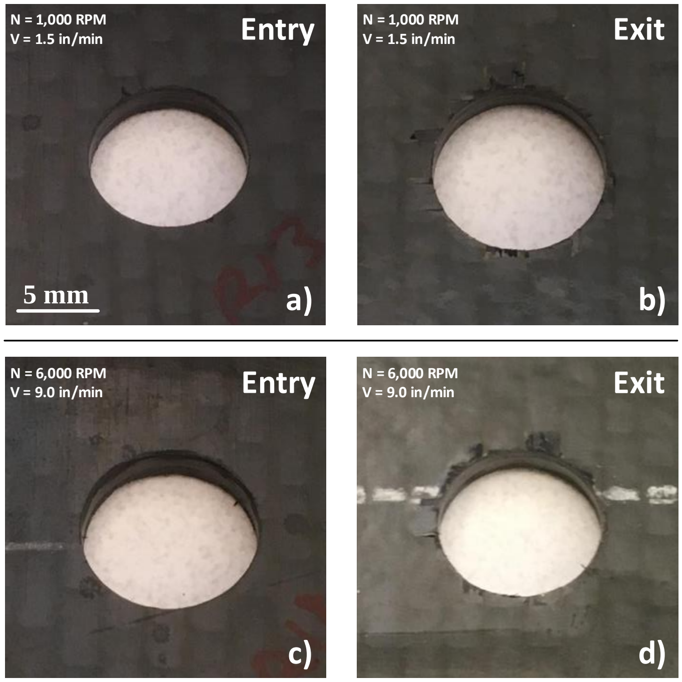

Figure 2-9: Surface imaging of CNC drilling for woven CFRP using a DAL drill (F_R = 0.0015 in/rev): (a) and (b) entry and exit surfaces, respectively, for 1,000 RPM and 1.5 in/min; (c) and (d) entry and exit surfaces, respectively, for 6,000 RPM and 9.0 in/min.

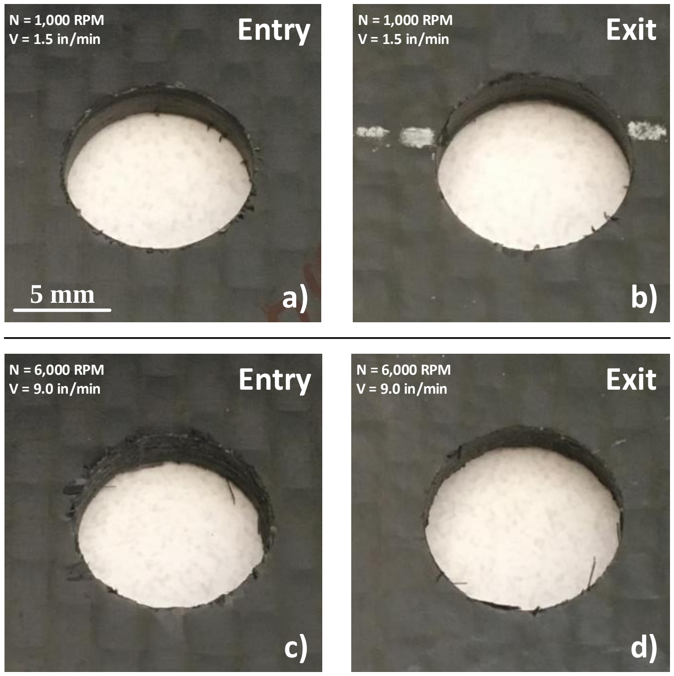

Figure 2-10: Surface imaging of CNC drilling for woven CFRP using an SPF drill (F_R = 0.0015 in/rev): (a) and (b) entry and exit surfaces, respectively, for 1,000 RPM and 1.5 in/min; (c) and (d) entry and exit surfaces, respectively, for 6,000 RPM and 9.0 in/min.

2.3.3 Constant Spindle Speed

Figure 2-11a compares the absolute maximum cutting force measured for both tools for woven AS4 CFRP. The results were obtained at 4,000 RPM for rotational feed rates ranging from 0.0005 in/rev to 0.0025 in/rev and axial cutting speeds ranging from 2.0 in/min to 10.0 in/min. Spindle speed was set at the manufacturer’s recommended value of 4,000 RPM. Shown in Figure 2-11b is a comparison of maximum primary and secondary cutting forces for the SPF drill. The results show that increasing rotational feed and cutting speed increases the thrust force from 43 N to 88 N and from 81 N to 165 N for the SPF and DAL drills, respectively. The same trend is shown in comparing the primary and secondary cutting forces for the SPF drill (Figure 2-12). Figure 2-13 shows only a negligible increase in delamination and burring at the exit surface using the DAL drill; the SPF drill produced comparable results at identical parameters. Comparing drilling performance using both drills with cross-ply and woven CFRP, it is clear that woven samples exhibit better overall machining quality. This was also noted by Feito et al. (2015), who analyzed the drilling performance of several tool geometries for near-identical woven AS4 and cross-ply IM7 CFRP material samples.

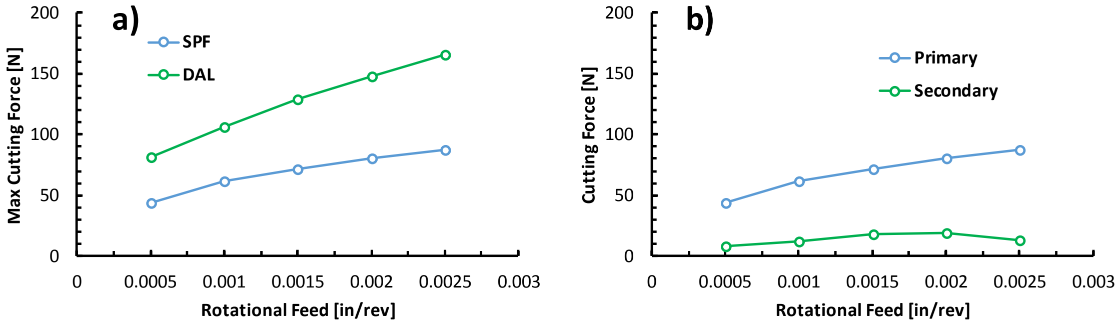

Figure 2-11: Cutting force comparisons measured by dynamometer in axial direction for drilling at varying rotational feed and 4,000 RPM spindle speed: (a) Maximum primary cutting force for SPF and DAL drills; (b) Comparison of primary and secondary cutting forces for the SPF drill.

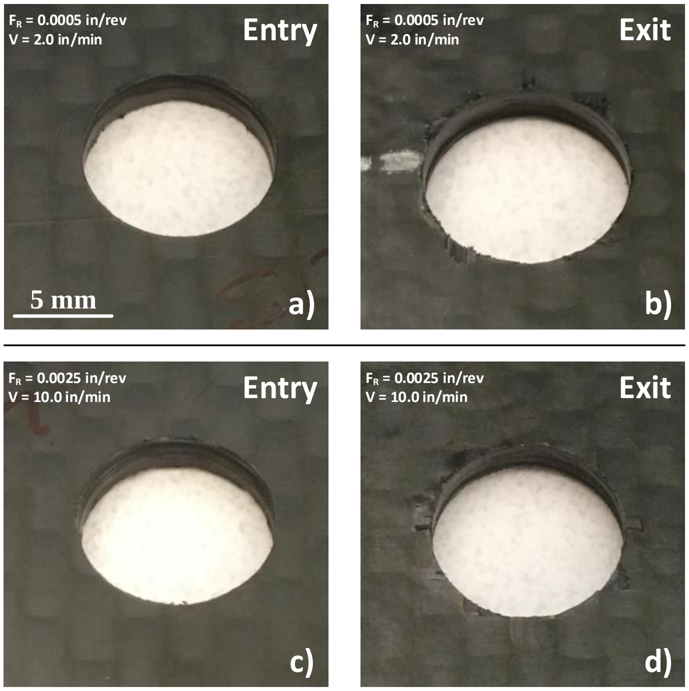

Figure 2-12: Surface imaging of CNC drilling for woven CFRP using an DAL drill (N = 4,000 RPM): (a) and (b) entry and exit surfaces, respectively, for 4,000 RPM and 2.0 in/min; (c) and (d) entry and exit surfaces, respectively, for 4,000 RPM and 10.0 in/min.

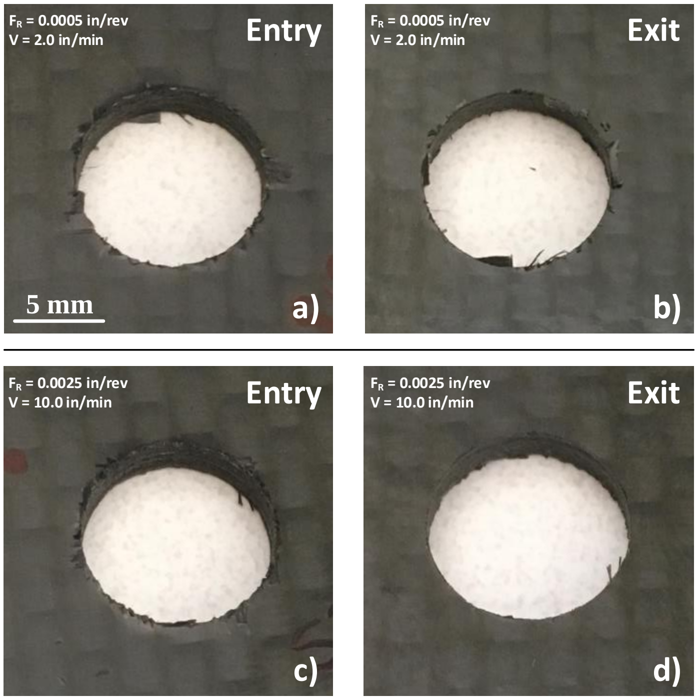

Figure 2-13: Surface imaging of CNC drilling for woven CFRP using a SPF drill (N = 4,000 RPM): (a) and (b) entry and exit surfaces, respectively, for 4,000 RPM and 2.0 in/min; (c) and (d) entry and exit surfaces, respectively, for 4,000 RPM and 10.0 in/min.

2.4 Conclusions

From the experiments in Chapter 2, it is evident that mechanical machining can be used for CFRP to achieve high speed flexible processing based on tool selection. These aspects make mechanical machining of CFRP a popular choice in industry. However, the results show a significant amount of damage at both the entry and exit surfaces related to high axial thrust force. Reducing the rotational feed rate was shown to reduce thrust force and improve machining quality. Drilling of woven CFRP was shown to be of better quality than cross-ply CFRP, likely due to the mechanical interlocking of fiber strands to resist shear deformation. Woven CFRP exhibited burring and peeling while cross-ply CFRP exhibited delamination. Decreasing the spindle speed of the SPF drill improved the surface roughness for both materials. Overall, results regarding performance difference related to tool coating are inconclusive; the diamond coating and split-point design did not appear to improve machining quality. Further in-depth investigation using direct comparisons of high performance drilling tools is required.

CHAPTER 3.

CW/MODULATED FIBER LASER MACHINING OF CFRP

3.1 Introduction

Fiber lasers have become a popular choice for materials processing in industry, particularly since the 1990s. Advantages of this laser type include high power, operational efficiency, process flexibility, and focal properties. Fiber laser systems are able to achieve twice the efficiency of diode-pumped solid-state systems in industrial applications with much higher beam parameter product (BPP) values. Additionally, high power (i.e. kW-range) levels combined with remote delivery through a fiber optic cable allow for robotic operation and high productivity. Fiber lasers can be operated in either continuous-wave (CW) or pulsed mode. In CW mode, there is no cycle time to allow for workpiece cooling. As such, thermal damage is typically extensive with wide HAZ formation. When the laser is operated in pulse mode, the interaction time is significantly reduced. This allows for higher applied pulse energy and power intensity without sacrificing machining quality. This is also of particular importance when considering the concepts related to the thermal response time of the CFRP, as discussed briefly in Section 1.2.2. Carbon-based fiber reinforcements typically have very short thermalization times while matrix resins and epoxies have much longer thermalization times. Combining these concepts with the applied laser-induced excitation rate (i.e. pulse duration and frequency) can provide insight into the level of machining quality that is attainable for a particular laser system.

In this chapter, CFRP laser machining experiments using a CW/modulated pulsed Yb:YAG fiber laser system are discussed. The results of the experiments will be used to gain an understanding of the physiochemical processes involved in microsecond laser ablation for CFRP. This understanding will help determine if high quality CFRP laser machining is possible using such a laser setup. The effects of laser power, pulse duration and frequency, pulse overlap, surface fiber orientation are examined for cross-ply IM7 CFRP using single-pass line cutting. Additionally, laser power was also investigated for woven AS4 CFRP.

3.2 Experiments

3.2.1 Experimental Setup

The experimental setup utilized a continuous wave Yb:YAG laser system (IPG YLR-500 AC). A diagram of the laser system is shown in Figure 3-1. Maximum power output is 500 W and the wavelength is 1070 nm, placing it in the NIR spectrum. An internal pulse generator modulates the duty cycle of laser to allow pulsed operation at a minimum pulse duration is 0.01 ms and maximum repetition frequency is 50 kHz. The beam is delivered remotely through an optical cable to a turret fixed to the spindle assembly of the Haas CNC mill from Chapter 2 (Figure 3-1a). The laser scans the top surface of the CFRP material using a turret mounted to the spindle holder (Figure 3-1b), with the scanning path being controlled using the X-Y stage of the CNC mill. Surface ply fiber orientation relative to the laser scanning path is defined by the angle θ (Figure 3-2a). As θ approaches 0° the scanning path is defined as parallel; 90° denotes an orthogonal path. Pulse spacing is determined by the repetition rate and scanning speed in Eq. 3.1. Pulse overlap is calculated using Eqs. 3.2 and 3.3, according to Figure 3-2b.

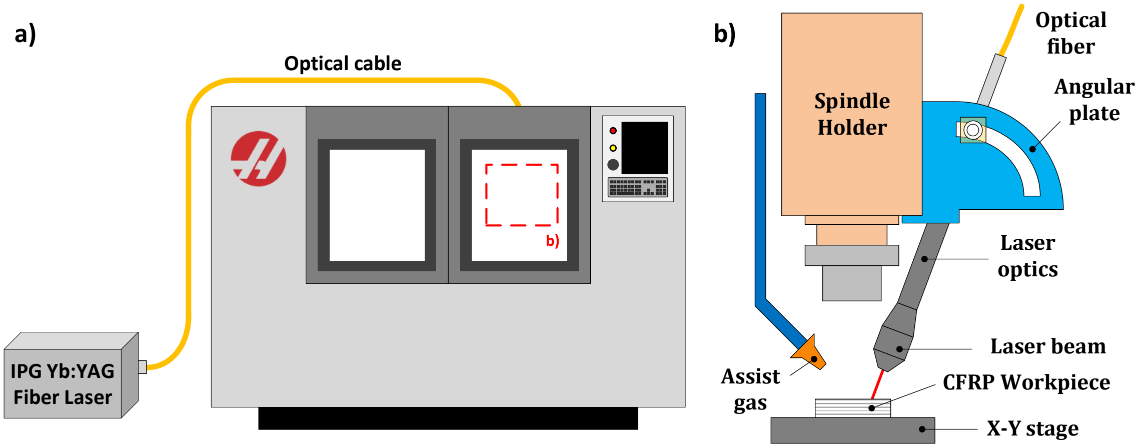

Figure 3-1: Diagram of Yb:YAG fiber laser setup for CFRP laser machining experiments: (a) laser fiber optic cable allows for remote operation; (b) adjustable fiber delivery head mounted to CNC mill spindle holder..

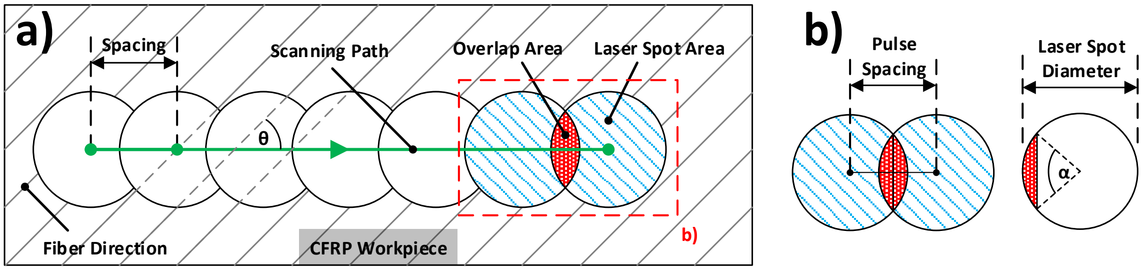

Figure 3-2: (a) Schematic of laser scan path over CFRP workpiece during nanosecond laser machining experiments; scan path direction, θ, is not relevant for woven CFRP samples. (b) Pulse Spacing and Laser Spot Diameter are used to calculate the Overlap Angle, α, and the Overlap Ratio, *OR*.

$$\text{Pulse Spacing} = \frac{\text{Laser Scanning Speed}}{\text{Laser Repetition Rate}} \tag{3.1}$$

$$\text{Overlap Angle, } \alpha\ [°] = 2\cos^{-1}\left(\frac{\text{Pulse Spacing}}{\text{Laser Spot Diameter}}\right) \tag{3.2}$$

$$\text{Overlap Ratio, OR } [\%] = \frac{\text{Overlap Area}}{\text{Laser Spot Area}} = \frac{4 \cdot r^2(\alpha - \sin\alpha)}{\pi \cdot {D_{spot}}^2} \tag{3.3}$$

$$\text{Average Power, } P_{avg}\ [\text{W}] = \text{Peak Power} \times \text{Frequency} \times \text{Duration} = P_{avg} \cdot f \cdot t_p \tag{3.4}$$

$$\text{Pulse Energy, } E_P\ [\text{mJ}] = \frac{\text{Average Laser Power}}{\text{Repitition Rate}} = \frac{P_{avg}}{f} \tag{3.5}$$

$$\text{Power Intensity, } I_P\ [\mathrm{W/cm^2}] = \frac{\text{Peak Laser Power}}{\text{Laser Spot Area}} = \frac{4 \cdot P_{peak}}{\pi \cdot {D_{spot}}^2} \tag{3.6}$$

$$\text{Energy Density, ED } [\mathrm{J/mm^2}] = \frac{\text{Average Laser Power}}{\text{Scanning Speed} \times \text{Laser Spot Diameter}} = \frac{P_{avg}}{V \cdot D_{spot}} \tag{3.7}$$

$$\text{Spot Diameter, } D_{spot}\ [\mu\mathrm{m}] = D_{waist}\sqrt{1 + z^2\left(\frac{4\lambda M^2}{\pi {D_{spot}}^2}\right)^2} \tag{3.8}$$

Laser power, pulse duration, and frequency can be set using either the laser touchscreen menu or IPG’s Pulse Shape Generator (PSG) computer software. The peak laser power was used to calculate the average laser power and pulse energy using Eqs. 3.4 and 3.5. Power intensity and energy density were calculated using Eqs. 3.6 and 3.7. The laser scan path and speed were set using a short G-code program in the user interface of the CNC mill. Simultaneous operation of the CNC mill with the laser was accomplished using a simple control circuit. Laser firing can be triggered by programming the auxiliary M-relays of the CNC mill. The samples thickness was 2.2 mm for both CFRP materials. Relevant properties are listed in Table 2-1 and Table 2-2. An Argon assist gas flow was sprayed over the target area during machining to evacuate debris, aid workpiece cooling, and prevent oxidation. Three-dimensional (3D) surface profiles were characterized using a confocal laser scanning microscope (CLSM) (Zeiss, LSM710) with a 488 nm Argon laser illumination source. Two-dimensional (2D) surface profiles were obtained by slicing the 3D confocal microscope surface profile using an open source software package (ImageJ). Summary of thermomechanical properties for Hexcel HexTow® fibers used in CFRP laser machining experiments. A Z-coordinate of -2.85 inches in the coordinate system of the CNC interface achieves the fully-focused laser waist diameter of approximately 35 μm; the working distance can be adjusted to achieve desired laser spot diameters according to Eq. 3.8, where z is the required working distance offset and M^2 is equal to 1.05.

3.2.2 Experiment Design

Single-pass line cutting experiments for laser machining tests of CFRP were designed to investigate the effects of four parameters: (1) CW mode, (2) laser power, (3) scanning velocity for pulse overlap, and (4) cross-ply surface fiber orientation. Laser machining of CFRP in continuous wave (CW) mode was investigated for cross-ply CFRP. Tests scanned a linear 2 inch path at maximum peak laser output of 500 W with a beam diameter of 1.2 mm, producing a power intensity of 4.5×10^4 W/cm^2 and energy density ranging from 5.0 J/mm^2 to 10.0 J/mm^2. Scanning velocity was in the range of 42.3 mm/s to 84.7 mm/s.

The effects of average laser power for cross-ply IM7 CFRP were investigated according to the test parameters in Table 3-1. Tests used a linear 2 inch path scanned along an orthogonal fiber direction. The pulse duration was 0.05 ms for frequencies ranging from 1 kHz to 5 kHz. The scanning velocity was 42.3 mm/s and spot diameter was 60 µm. Peak power was varied from 75 W up to 137.5 W. Maximum power intensity was 1.8×10^7 W/cm^2 and maximum energy density was 19.7 J/mm^2.

The effects of average laser power and pulse repetition rate were investigated for woven AS4 CFRP. Tests scanned a linear 2 inch path using a pulse duration was 0.05 ms and pulse frequencies ranging from 1 kHz to 5 kHz. The scanning velocity was 42.3 mm/s and spot diameter was 60 µm. Power intensity ranged from 4.4×10^6 W/cm2 to 6.2×10^6 W/cm^2. Energy density ranged from 2.7 J/mm^2 to 17.2 J/mm^2.

The effects of scanning velocity and pulse overlap in LP mode were investigated using single-pass machining for cross-ply CFRP. Tests scanned a linear 2 inch path at speeds ranging from 8.5 to 84.7 mm/s. A spot diameter of 60 µm produced pulse overlap ranging from 0% to 82%. Average power was held constant at 40 W for a power intensity of 1.4×10^7 W/cm^2. Energy density ranged from 7.9 J/mm^2 to 78.7 J/mm^2 according to pulse overlap. The laser scanning path direction was $\theta = 90°$ relative to the surface fiber orientation.

Table 3-1: Summary of experimental conditions for tests investigating the effects of laser power and pulse frequency for cross-ply IM7 CFRP.

Pulse Duration	**Pulse Frequency**	**Pulse Energy**	**Average Power**	**Power Intensity**	**Energy Density**
ms	Hz	mJ	W	(10^6) W/cm^2	J/mm^2
0.05	1000	3.75	3.75	2.7	1.5
0.05	1000	4.38	4.38	3.1	1.7
0.05	1500	3.13	4.69	2.2	1.8
0.05	1000	5.00	5.00	3.5	2.0
0.05	1000	5.63	5.63	4.0	2.2
0.05	1000	6.25	6.25	4.4	2.5
0.05	1000	6.88	6.88	4.9	2.7
0.05	2000	3.75	7.50	2.7	3.0
0.05	2000	6.25	12.5	4.4	4.9
0.05	2000	6.88	13.8	4.9	5.4
0.05	5000	3.13	15.6	2.2	6.2
0.05	5000	3.75	18.8	2.7	7.4
0.05	100	25.0	2.50	18	19

The effect of surface fiber orientation for cross-ply CFRP was investigated using single-pass machining by performing identical tests for laser scanning path at θ = 0° and θ = 90°. A linear 2 inch path was scanned at speeds between 33.9 mm/s and 84.7 mm/s with a spot diameter of 60 µm. Nominal pulse frequency varied from 1 kHz to 8 kHz for a pulse duration of 0.1 ms. Peak laser power was held constant at 400 W for a power intensity of 1.4×10^7 W/cm^2. Energy density ranged from 3.0 J/mm^2 to 39.4 J/mm^2.

The effect of surface fiber orientation for cross-ply CFRP was investigated using single-pass machining for laser scanning path at θ = 0° and θ = 90°. A linear 2 inch path was scanned at speeds ranging from 33.9 to 84.7 mm/s with a spot diameter of 60 µm for various levels of pulse overlap. Power intensity was constant at 1.4×10^7 W/cm^2 for θ = 0° and ranged from 2.7×10^6 W/cm^2 to 5.3×10^6 W/cm^2. Likewise, energy density ranged from 15.7 J/mm^2 to 39.4 J/mm^2 for θ = 0° and from 3.0 J/mm^2 to 5.9 J/mm^2 for θ = 90°.

3.3 Results & Discussions

3.3.1 Continuous Wave Mode

An example of continuous wave (CW) mode laser machining is shown in Figure 3-3 below. CW mode does not allow for cyclic cooling of the CFRP workpiece and leads to extensive HAZ formation despite very low power intensity and low energy density (Figure 3-3a). Energy is continually conducted along the fiber axis, which causes a large area of matrix material to be heated and evaporated. This cannot be adequately compensated for by the Argon assist gas flow. Figure 3-3b is a close-up view of the machined laser path showing rough surface texture characterized by fiber swelling and matrix recession exposing the fiber ends. Excessive matrix evaporation and poor machined surface quality makes IR laser machining in CW mode unacceptable.

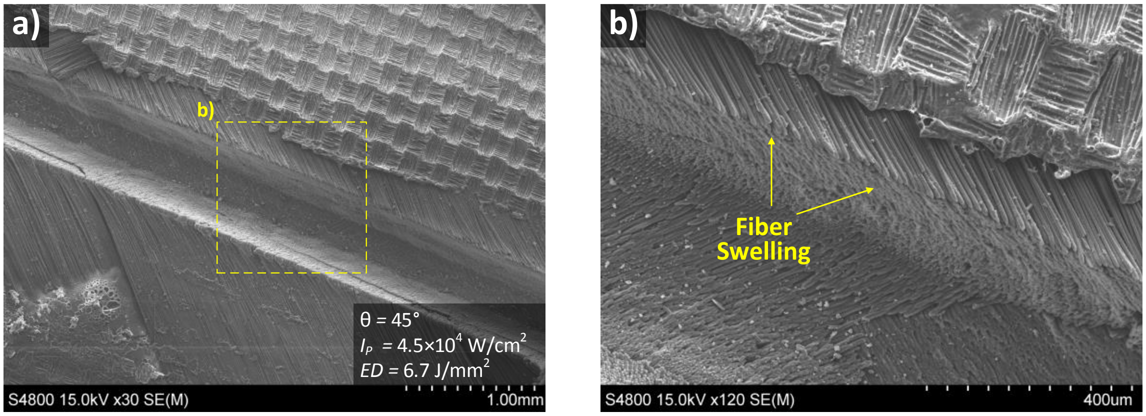

Figure 3-3: Surface SEM micrograph of laser cutting of cross-ply CFRP using CW mode: (a) machining damage is thermal-based, mechanical defects are removed; (b) fiber swelling and matrix recession is observed at machined surface.

3.3.2 Effect of Laser Power

Results for tests investigating the effects of average laser power and pulse frequency are summarized in Figure 3-4. Laser-induced plasma effects are avoided due to low power intensity. All tests showed effective laser ablation.

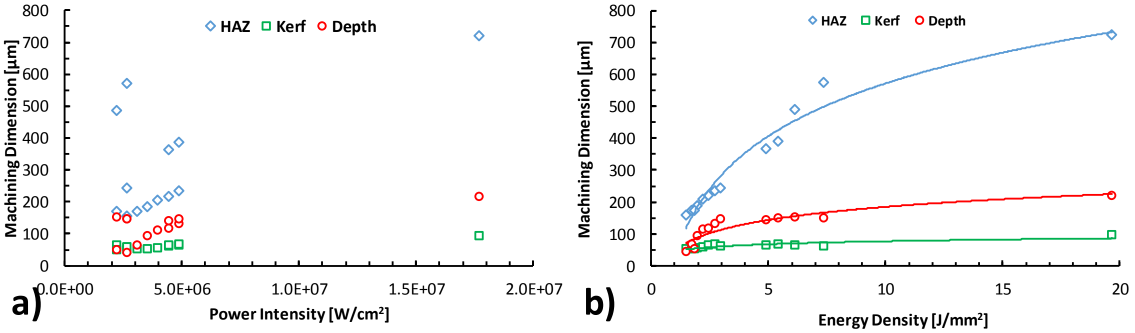

Figure 3-4: Machining results from tests for increasing laser input for cross-ply IM7 CFRP: results are graphed using (a) power intensity and (b) energy density. Energy density appears to show a logarithmic relationship while power intensity is inconclusive.

Figure 3-5 shows the significantly improved machining quality that is possible through pulsed laser ablation. Fiber delamination, burring, peeling, and other physical surface defects observed using mechanical machining in Chapter 2 are eliminated. Also, matrix evaporation is reduced for pulsed operation versus continuous wave delivery from Section 3.3.1.

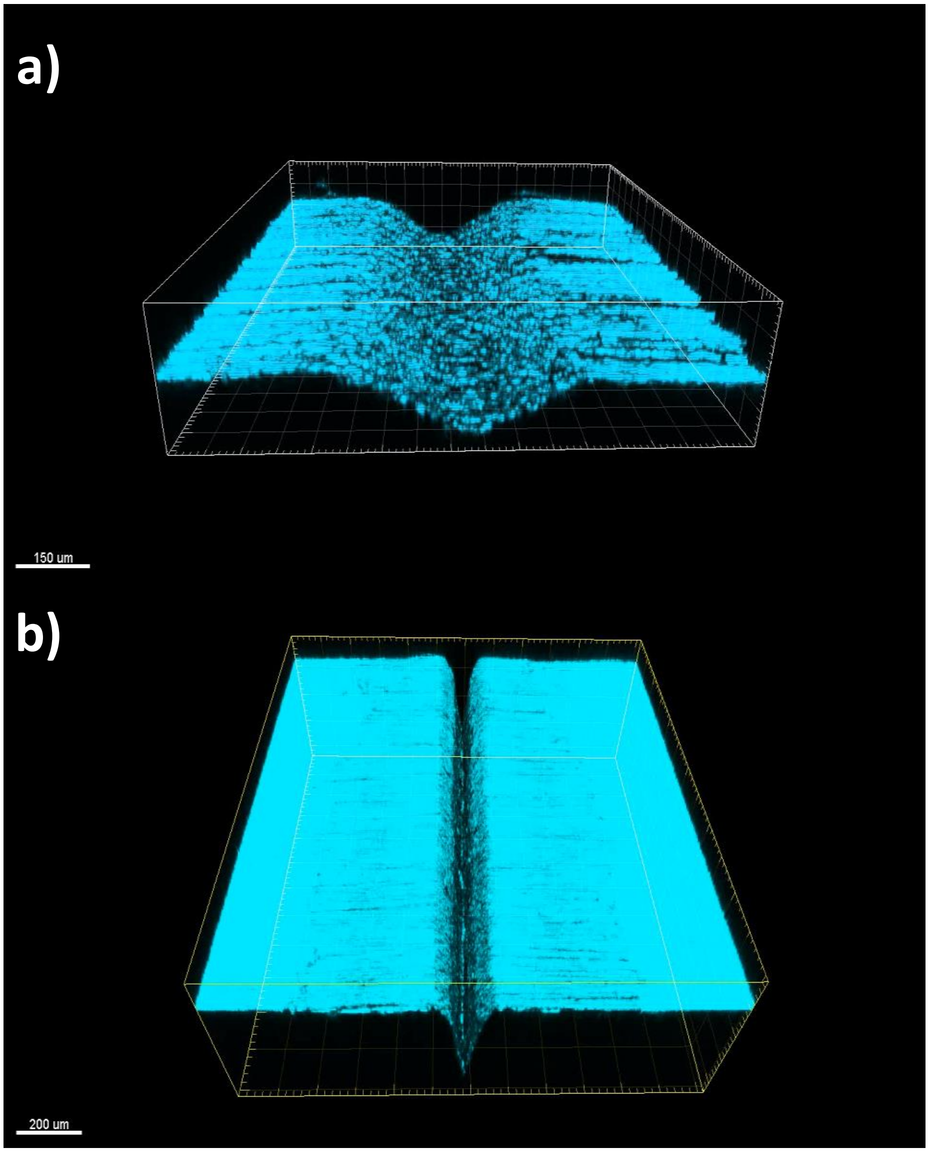

Figure 3-5: 3D confocal micrographs of laser scanned tracks in single-pass line cutting experiments of cross-ply CFRP: (a) inefficient CFRP laser machining due to laser spot size greater than 1 mm and low energy density; (b) CFRP laser machining is improved for 60 µm spot size and high energy density of 11.9 J/mm^2.

However, the machining depth is shallow due to the low power intensity. Power intensity is directly proportional to the peak laser power, which increases as pulse duration is shortened for a given average power. For pulse durations in the microsecond domain, laser-material interaction is relatively long and causes HAZ expansion for CFRP. Higher power intensities show widespread matrix evaporation and melting due to the long pulse duration at high frequency and low power intensity. In areas where the matrix has been evaporated to expose the underlying fibers, the temperature increase was sufficient to effectively boil the epoxy away. In regions closer to the target area, the temperature was sufficient to melt the matrix but insufficient to cause evaporation. In those areas, the matrix undergone a phase change to liquid state and then re-solidifying in a deformed state. This is visible in the form of bubbles and pooled re-solidification areas with irregular HAZ boundaries. The fibers are heated to sublimation temperature due to heat accumulation, but also conduct a significant amount of heat along the fiber axis. The matrix is continually heated over the microsecond pulse duration at high frequency with reduced cooling time.

These conclusions regarding the extensiveness and type of thermal damage phenomenon were repeatedly observed in testing with the microsecond pulsed fiber laser system. Results for tests investigating the effects of laser power on woven AS4 CFRP are illustrated in Figure 3-6. The images show effective CFRP material removal only at high pulse frequency. Figure 3-6a shows an interesting kerf discontinuity phenomena in areas near the fiber weave boundaries for low pulse frequencies (1-2 kHz). Tests at slightly elevated power intensity and higher pulse frequency (at least 5 kHz) resolved the kerf discontinuity effect but at a significant cost of thermal damage (Figure 3-6b). Increasing laser power and pulse frequency increased the kerf width to 87 µm. The HAZ width increased from 552 µm to 1064 µm, respectively, with large areas of both matrix melting and evaporation.

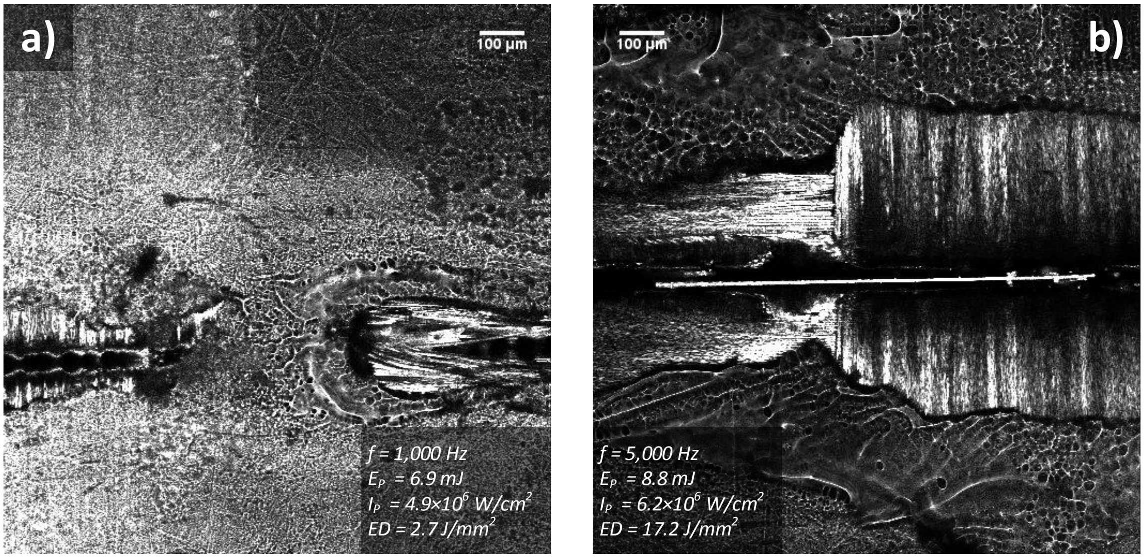

Figure 3-6: Surface micrographs of laser cutting for woven CFRP showing pulse frequency effect on kerf continuity at local fiber weave boundary for (a) 1 kHz and (b) 5 kHz. The increased pulse overlap and slight increase in laser power increases energy density from 2.7 J/mm^2 to 17.2 J/mm^2.

One possible explanation for these results is related to the absorption and thickness of the top layer of the matrix. At the weave boundaries, the fiber strands are linked together in a way that increases the effective depth of the top layer of the epoxy material. As the strands are woven on top of each other, there is more matrix material to be removed at these boundaries. Since the matrix is effectively transparent for NIR wavelengths, the epoxy can only be removed by indirect heating from the fibers. If the surrounding matrix is not sufficiently heated, it will not be removed. Significantly more energy is accumulated in the target area at elevated pulse frequencies and, therefore, higher energy densities. Therefore, the laser irradiation is initially absorbed deeper into the CFRP surface at the weave boundaries than for cross-ply samples.

3.3.3 Scanning Velocity and Pulse Overlap

Results for tests investigating the effects of scanning velocity and pulse overlap are summarized in Figure 3-7. Scanning velocity, pulse frequency, and spot size both determine the percentage of pulse overlap. For these tests, pulse frequency and duration were held constant for variable scanning velocity. The size of the HAZ area is very sensitive to heat accumulation at increasingly high pulse overlap, similar to previous results. This is expected since the heat transfer effects are rapidly amplified with increasing pulse overlap and more energy is delivered to the target area. For example, increasing pulse overlap from 0% to around 47% increased the HAZ area width from 493 µm to 795 µm. Likewise, the kerf width increased from 60 µm to 80 µm. Lower overlap ratios produce greater pulse feed striations along the kerf. The spacing of these striations is equal to the center-to-center spacing of laser pulses according to the frequency and scanning speed, seen in Figure 3-8.

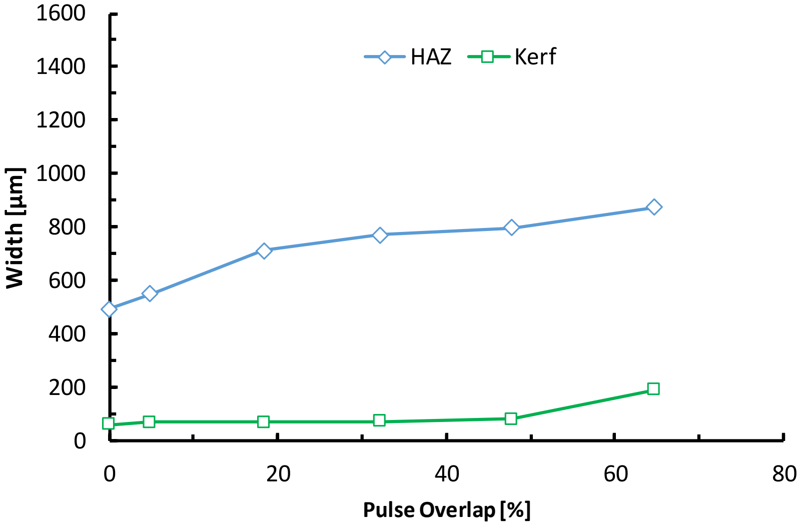

Figure 3-7: Surface machining results for increasing pulse overlap using cross-ply IM7 CFRP. Kerf and HAZ width increase according to increase in energy density.

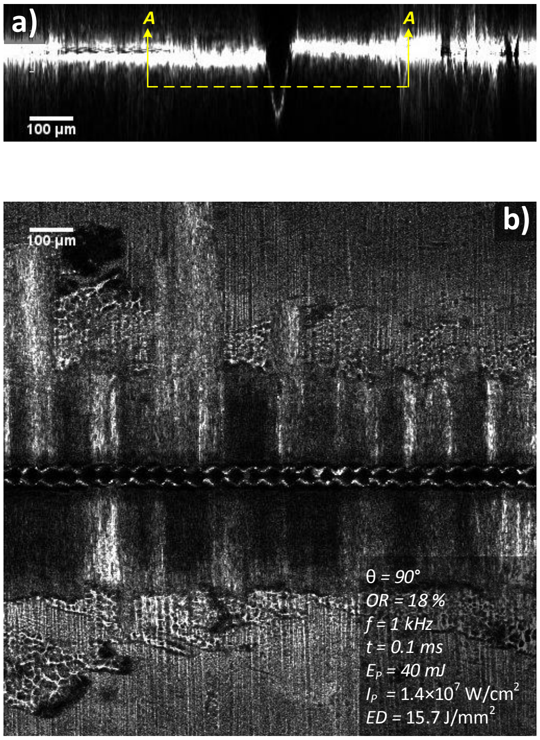

Figure 3-8: Imaging of laser cutting for cross-ply CFRP for effect of pulse overlap: (a) cross-section view of typical CFRP laser machining profile; (b) surface micrograph of laser test with 18% pulse overlap with focal plane adjusted below the workpiece surface. Section A-A shows pulse feed striations from low overlap ratios.

3.3.4 Cross-Ply Fiber Orientation

Results for tests investigating the effects of fiber orientation in cross-ply CFRP samples are summarized in Figure 3-9. Kerf width and machining depth area largely unaffected by fiber orientation. As expected, thermal damage is very sensitive to surface fiber orientation with parallel orientation (θ = 0°) showing narrow HAZ width. For orthogonal orientation (θ = 90°) heat is conducted away from the cutting zone along the fiber axes. This heats the adjacent surface matrix and causes evaporation, melting, and re-solidification at the fiber ends. When θ = 0°, heat is carried along the laser scanning path, resulting in less heat conduction conducted to the adjacent matrix. A comparison is illustrated below in Figure 3-10. The thermal conductivity for a typical polymer resin is approximately 0.25 W/m·K while the thermal conductivities for the HexTow IM7 and AS4 fibers are 5.4 W/m·K and 6.8 W/m·K, respectively. From Figure 3-10a, the thermal damage is more apparent on the right side of the machining zone than the left, which is attributed to the assist gas flow not being perfectly aligned with the laser scanning path and causing a slight distortion of the HAZ region.

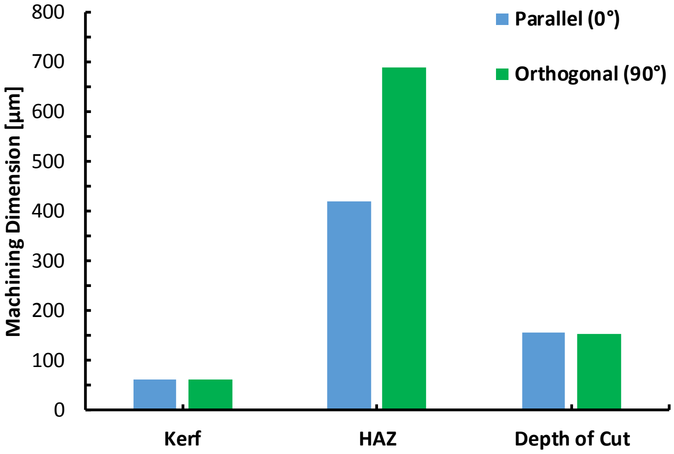

Figure 3-9: Machining dimension results comparing parallel and orthogonal fiber directions: (a) 18% overlap; (b) 32% overlap. Exposed HAZ represents complete fiber exposure due to matrix recession; total HAZ width adds additional area where partial melting and re-solidification has occurred.

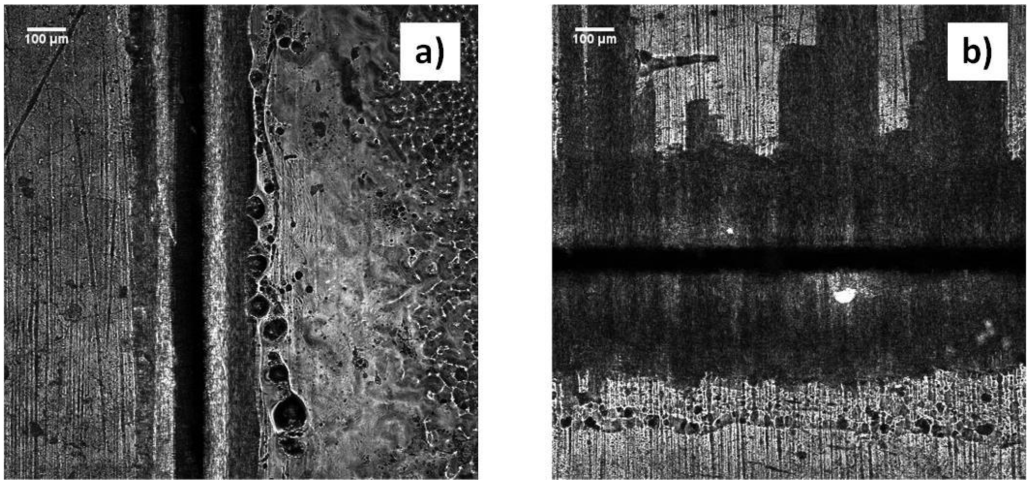

Figure 3-10: Surface micrographs of laser cutting for cross-ply CFRP showing the effect of fiber orientation and pulse overlap: (a) parallel with 18% overlap; (b) orthogonal with 32% overlap. Fibers are visible at the surface for orthogonal orientation showing a very wide HAZ area. Matrix texturing in test 35 is due to assist gas flow.

3.4 Conclusions

Results of experiments in Chapter 3 showed the improved quality and flexibility that is possible using a CW/modulated fiber laser system. The fiber optic cable allows remote delivery of the laser beam and high power levels for long pulse durations. Additionally, laser systems offer significantly improved machining quality of the mechanical process from Chapter 2.

However, the CFRP machining performance of the Yb:YAG fiber laser system can be limited by long pulse duration and low power intensity. Pulse durations in the microsecond domain significantly lengthen the laser-material interaction time. Also, low power intensity means that the CFRP structure absorbs considerable energy below the ablation threshold of the fiber reinforcements, leading to thermal damage. This is due to excessive heat conduction and accumulation effects from relatively long pulse duration, which increases the laser-material interaction time, promotes HAZ expansion, and significantly decreases ablation rate. Photon absorption from plasma shielding plays is assumed to reduce incident power intensity by the inverse Bremsstrahlung mechanism.

A logarithmic relationship was observed for laser input using energy density; power intensity did not account for pulse duration and frequency in predicting results. Critical values were identified for cross-ply IM7 CFRP; calculated values were comparable to the literature. Laser power, pulse overlap, frequency, and cross-ply fiber orientation were found to have a significant impact on surface results. Kerf discontinuities were observed for woven AS4 samples at the local weave boundaries for pulse frequencies below 5 kHz. This is hypothesized to be the result of the absorption properties of the matrix material for IR irradiation, which reduces the power intensity absorbed by the underlying woven fiber strands according to the Beer-Lambert Law. Multi-pass machining was unsuccessful; through machining was not observed in testing. Low ablation rates and matrix re-solidification observed in testing make this particular laser system ineffective for laser machining. Overall, it was shown that laser ablation using our Yb:YAG fiber laser setup provides improved machining performance compared to mechanical processes.

CHAPTER 4.

HIGH-ENERGY NANOSECOND PULSE LASER MACHINING OF CFRP

4.1 Introduction

In this chapter, CFRP machining experiments using a high-energy nanosecond-pulsed NIR laser system are presented. Laser machining of CFRP using a high-energy pulsed laser source has not been well studied in the literature, particularly for high-energy long-duration nanosecond pulsing at low frequency and high power intensity. Past studies have been conducted using high-energy microsecond lasers as well as Q-Switch pulsing at low energy. Few studies have attempted to address the phenomena of laser-induced plasma effects in CFRP laser machining. This research will offer potential explanations related to plasma photon absorption as it relates to the laser ablation process for CFRP. In particular, the physiochemical nature of the material removal and energy absorption mechanisms is addressed. The understanding gained from this research will allow various energy absorption mechanisms to be characterized in order to determine optimum processing parameters and quantify laser cutting quality for various machining operations.

The time duration of laser-material interaction is one of the primary factors in determining CFRP machining quality using a pulsed laser system. Results from Chapter 3 have shown that short pulsing at high laser power increases laser ablation rates while reducing thermal damage. Short duration pulses (i.e. nanosecond domain or shorter) are ideal for optimizing laser ablation by transferring a high amount of energy in a short amount of time. This is the primary difference between the laser setups in Chapter 3 and Chapter 4; the high-energy nanosecond laser uses pulse duration that is shorter by a factor of either 1,000 or 10,000, depending on the pulse mode. Subsequently, power intensity values reach a range of $10^9 – 10^{12}$ W/cm^2, an increase by a similar factor of at least 1,000.

In this work, a keyhole-mode cutting mechanism was demonstrated for the first time for CFRP using the high-energy long-duration nanosecond laser system. The effects of pulse duration, laser power, pulse overlap, and surface fiber direction were examined for cross-ply IM7 CFRP using single-pass line cutting. Additionally, laser power was also examined for woven AS4 CFRP. Multi-pass line cutting and pocketing was investigated for cross-ply CFRP for line cutting. Finally, contour drilling was performed for both materials.

4.2 Experiments

4.2.1 Experimental Setup

The experimental setup utilized a high energy Nd:YAG nanosecond-pulsed laser system (Spectra-Physics Quanta-Ray Lab-150). The beam output diameter is 10 mm at an emission wavelength of 1064 nm, placing it in the NIR spectrum. The laser has two pulse modes: Q-Switch (QSW) and Long Pulse (LP), which pulse durations of 8 ns and 120 ns, respectively, both at a fixed repetition rate of 10 Hz. Laser scanning is implemented using an IntelliSCAN 20 scan head and VarioSCAN 40 dynamic focusing unit, both controlled by ScanLab computer software. A schematic of the experimental setup is shown in Figure 4-1. The laser scanning path for machining experiments is identical to the concepts from Chapter 3 in Figure 3-2; likewise relevant process variables are calculated using Eqs. 3.1-3.8. The laser head scans the top surface of the CFRP material, with pulse spacing being determined by the repetition rate and scanning speed in Eq. 3.1. Surface ply fiber orientation relative to the laser scanning path is defined by the angle θ. As θ approaches 0° the scanning path is defined as parallel; 90° denotes an orthogonal path. Pulse overlap is calculated using Eqs. 3.2 and 3.3 according to Figure 3-2b.

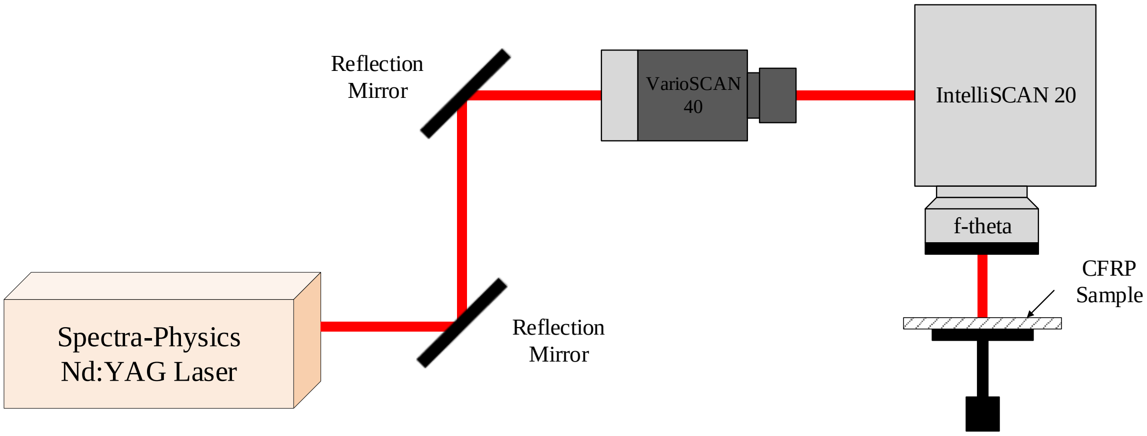

Figure 4-1: Diagram of high energy nanosecond Nd:YAG laser system setup for machining experiments. Beam output diameter is 10 mm; focused waist diameter approximately 40 µm. Testing performed both with and without the VarioScan unit.

Average laser power measured the incident laser power using an Ophir Photonics 10-P measurement sensor; a full calibration of laser power output is shown in Figure 4-2. The average laser power was used to calculate the peak laser power and pulse energy using Eqs. 3.4 and 3.5. Power intensity and energy density were calculated using Eqs. 3.6 and 3.7. The optimum working distance was found by firing laser pulses at thermal paper and measuring the spot diameter. A working distance of 303 mm achieves the fully-focused laser waist diameter of approximately 40 µm; the working distance was adjusted to achieve desired laser spot diameters according to Eq. 3.8, where z is the required working distance offset and M^2 is equal to 1.1. The samples thickness was 2.2 mm for both CFRP materials. Relevant properties are listed in Table 2-1 and Table 2-2. An Argon assist gas flow was sprayed over the target area during machining to evacuate debris, aid workpiece cooling, and prevent oxidation. Surface analysis was performed using a scanning electron microscope (SEM) (Hitachi, S-4800). Three-dimensional (3D) surface profiles were characterized using a confocal laser scanning microscope (CLSM) (Zeiss, LSM710) with a 488 nm Argon laser illumination source. Two-dimensional (2D) surface profiles were obtained by slicing the 3D confocal microscope surface profile using an open source software package (ImageJ).

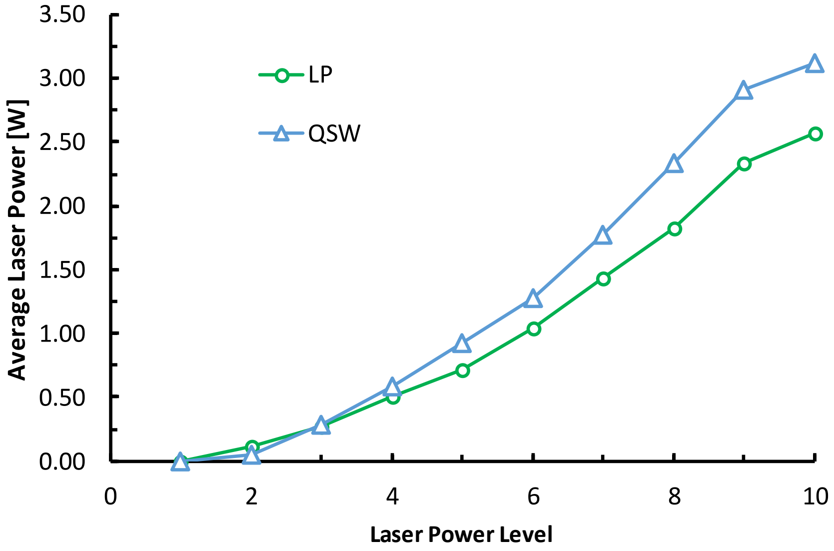

Figure 4-2: Calibration of measured average laser power at each control level; laser power levels are continuous from 0 to 10. Higher laser power is available in Q-Switch mode due to the shorter pulse duration.

4.2.2 Experiment Design

Line cutting experiments for laser machining tests of CFRP were designed to investigate the effects of four parameters: (1) pulse mode, (2) laser power, (3) scanning velocity for pulse overlap, (4) cross-ply surface fiber orientation, and (5) the effect of additional laser passes. Multi-pass experiments for laser machining tests of CFRP were designed to investigate two processes: (1) pocketing and (2) contour drilling. The effects of pulse duration and energy density for both CFRP materials were investigated using single-pass machining according to Table 4-1. The laser scanning path direction was θ = 45° relative to the surface fiber orientation. For cross-ply CFRP, a linear 10 mm path was scanned at a velocity of 1.0 mm/s using a spot diameter of 40 µm. For AS4 CFRP, the path length, scan velocity, and spot diameter were 5 mm, 0.3 mm/s, and 75 µm, respectively. Desired power levels were attained according to the calibration in Figure 4-2.

Table 4-1: Experimental conditions investigating the effects of laser power and pulse duration for both types of CFRP material.

Pulse Mode	**Pulse Duration**	**Pulse Energy**	**Average Power**	**Power Intensity (10^8)**	**Energy Density**
	ns	mJ	W	(10^8) W/cm^2	J/mm^2
QSW	8	5	0.05	47.1	1.25
QSW	8	20	0.20	188	5.00
QSW	8	48	0.48	452	12.0
QSW	8	93	0.93	876	23.3
QSW	8	131	1.31	1230	32.8
LP	120	5	0.05	3.14	0.38
LP	120	21	0.21	13.2	5.25
LP	120	44	0.44	27.6	11.0
LP	120	80	0.80	50.2	20.0
LP	120	111	1.11	69.7	27.8
LP	120	144	1.44	90.4	36.0
LP	120	183	1.83	115	45.8
LP	120	233	2.33	146	58.3
LP	120	257	2.57	161	64.3

The effects of scanning velocity and pulse overlap were investigated using single-pass machining for cross-ply CFRP. Tests scanned a linear 10 mm path in LP mode at 0.4-1.0 mm/s. A spot diameter of 100 µm produced pulse overlap ranging from 0% to 50%. Average power was held constant at 1.44 W for a power intensity of 1.5×10^{10} W/cm^2. Energy density ranged from 14.4 J/mm^2 to 36.0 J/mm^2 according to pulse overlap. The laser scanning path direction was $\theta = 45°$ relative to the surface fiber orientation.

The effect of surface fiber orientation for cross-ply CFRP was investigated using single-pass machining by performing identical tests for laser scanning path at $\theta = 0°$ and $\theta = 90°$. A linear 10 mm path was scanned in LP mode at a velocity of 0.3 mm/s with a spot diameter of 200 µm for 80% pulse overlap. Power intensity and energy density were 2.8×10^9 W/cm^2 and 16.3 J/mm^2, respectively.

Line scanning using multiple laser passes was performed on cross-ply CFRP to investigate the cumulative effects on the kerf and HAZ. All tests used a power intensity of 1.1×10^{10} W/cm^2 and an energy density of 31.6 J/mm^2. The laser scanning path direction was $\theta = 90°$ relative to the surface fiber orientation. Tests scanned a linear 5 mm at a velocity of 0.3 mm/s with a spot diameter of 100 µm for 60% pulse overlap.

Contour laser drilling was performed for both CFRP materials. Scanning speed was 0.3 mm/s using a 75 µm spot diameter for approximately 50% pulse overlap. Holes of 4 mm and 6 mm diameter were drilled at moderate power (1.0 W, 1.9×10^{10} W/cm^2, 44.9 J/mm^2) and maximum power (1.0 W, 1.9×10^{10} W/cm^2, 44.9 J/mm^2) for various numbers of laser passes.

Finally, laser pocketing was performed in LP mode for cross-ply IM7 CFRP according to Figure 4-3. A square pocket was incrementally machined to produce a staircase depth profile to better analyze the surface integrity of laser machined surfaces. Scanning at 0.4 mm/s using a spot diameter of 100 µm produced 40% pulse overlap. Moderate laser power yielded an average power of 1.4 W, power intensity of 1.5×10^{10} W/cm^2, and energy density of 28.0 J/mm^2.

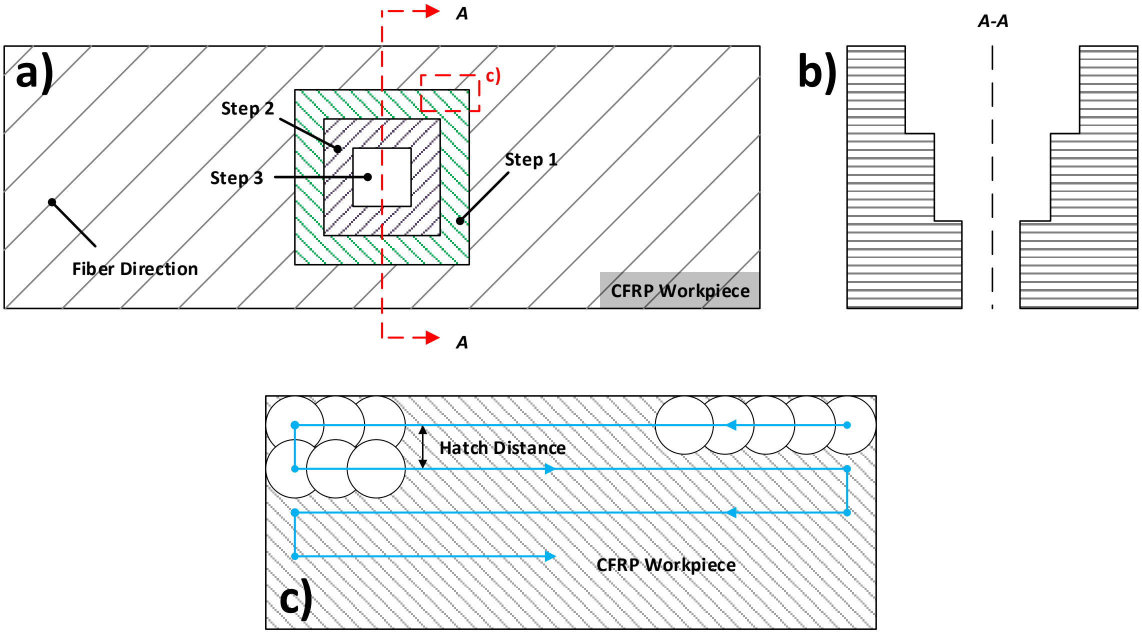

Figure 4-3: (a) Profile of contour pocketing process for cross-ply IM7 CFRP in LP mode. (b) Section A-A shows a staircase cross-section: each subsequent step uses one laser pass, third step is executed twice to produce thru cut. (c) Laser scan path; spacing is defined by a hatching distance between adjacent scanning paths.

4.3 Results

4.3.1 LP Mode vs. QSW Mode

Figure 4-4 shows the SEM and confocal micrographs of the typical surface morphology for cross-ply CFRP after a single laser scan in LP and QSW mode. Figure 4-4a shows a single-pass laser scan in LP mode produced a deep, clean cut with very minor defects using a spot size of 200 µm under laser power intensity of 2.8×10^9 W/cm^2. The 3D surface profile of the cut was obtained using the confocal microscope. The 3D confocal micrograph was sectioned using ImageJ to obtain the 2D cross-sectional surface profile. The cross-sectional micrograph shows a clean trench profile with a keyhole shape, and the kerf and depth of cut were 230 µm and 367 µm, respectively.

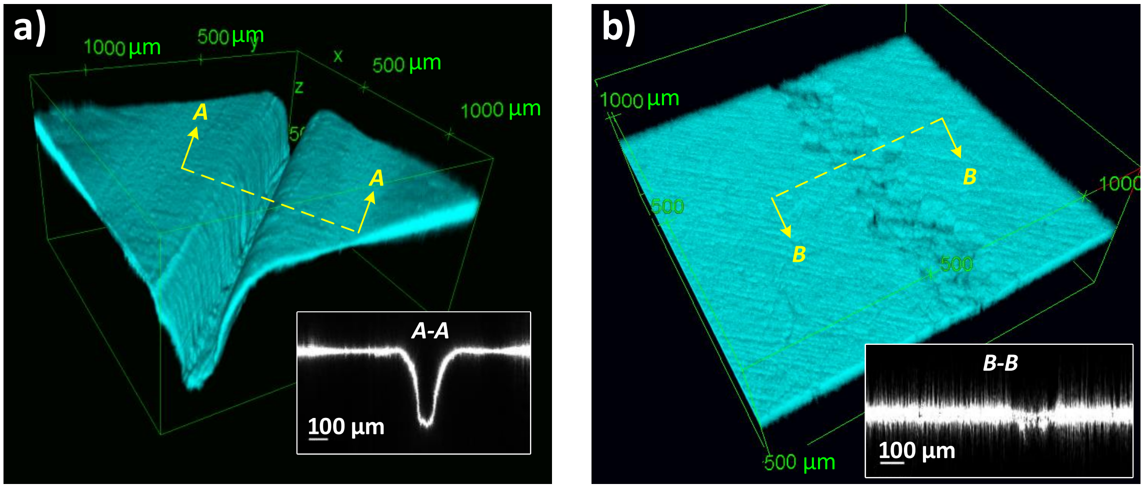

Figure 4-4: Laser scanned tracks in the single-pass line cutting experiments of cross-ply CFRP: (b) 3D confocal micrograph and 2D profile of the keyhole-shaped trench using LP mode; (d) 3D confocal micrograph and 2D profile for the ineffective cut using QSW mode.

As shown in Figure 4-4b, no significant cut was obtained after a single-pass laser scan in Q-Switch mode using a spot size of 40 µm under a power intensity of 6.0×10^{10} W/cm^2. The matrix resin was removed along the scanned track, and only the only fibers in the top layer of the CFRP specimen were cut. The 3D confocal micrograph shows the surface level was barely modified along the laser scanned track in Q-Switch mode. The 2D cross-sectional surface profile shows this surface profile change was limited, and was not even greater than the signal noise on the uncut surface. No trench could be formed by increasing the power intensity (as high as 1.3×10^{12} W/cm^2), and only a greater area of matrix resin was removed. QSW mode was deemed ineffective, even though the laser power intensity was ten times or even hundreds of times higher than that of LP mode.

Optical breakdown and subsequent plasma absorption was observed in all Q-Switch (QSW) tests. Previous studies have estimated the critical power intensity for optical breakdown of air to be approximately 4.42 x 10^9 W/cm^2 for a wavelength 1064 nm at a similar pulse duration of 6 ns. Power intensity values for all tests using QSW mode exceed this threshold value with a minimum intensity of 5.5×10^{10} W/cm^2. Therefore, single-pass machining of the CFRP material in QSW mode was ineffective. Surface HAZ formation was observed, as seen in Figure 4-5, with size being proportional to energy density. When optical breakdown occurs, an intensely absorptive plasma plume forms near the target area. This results in a significant reduction in the incident laser energy delivered to the CFRP surface. Although the absorbed laser energy is insufficient to ablate the fiber reinforcements, there is sufficient energy absorption to vaporize a very thin layer of matrix epoxy and cause the deformation seen in SEM imaging. Further details regarding this phenomenon will be discussed in Section 4.5.

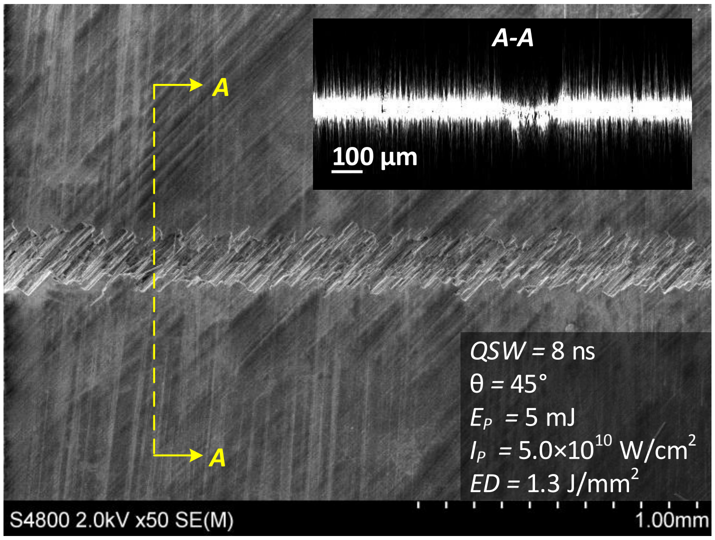

Figure 4-5: Surface SEM micrograph of laser cutting of cross-ply CFRP using QSW mode showing ineffective laser ablation and HAZ formation; cross sectional profile A-A shows no measurable ablation depth.

4.3.2 Effect of Laser Power

Optical breakdown was avoided in all Long Pulse (LP) trials. The critical power intensity in LP mode is theoretically higher than QSW mode due to the longer pulse duration of 120 ns. Therefore, all subsequent tests in this study used LP mode exclusively. Results over a range of energy density levels using cross-ply IM7 CFRP are summarized in Figure 4-6a. Overall, the results show a logarithmic relationship, which fits the original hypothesis. Increased laser power results in HAZ expansion and increased machining depth due to energy absorption at greater depths according to the Beer-Lambert Law. Using the data for machining depth from Figure 4-6a, the critical energy density was estimated to be 0.79 J/mm^2. Laser ablation is considered ineffective at energy density below this value. Unlike the high energy Nd:YAG laser used in this study, laser systems with fast pulse frequencies (kHz) rapidly accumulate heat in the machining zone. This reduces the required laser fluence to raise the CFRP material to sublimation temperature during photo-thermal ablation, but with a comparable energy density.

Energy density results using woven AS4 CFRP in LP mode are summarized in Figure 4-6b and show a similar logarithmic relationship. Critical energy density was estimated at 2.3 J/mm^2, which is higher than IM7 CFRP. This can be attributed to the greater thermal properties of AS4 fibers from Table 2-1, which means that more of the absorbed energy is transported away from the machining zone. Therefore, more laser input is required in order to be raise the fibers to sublimation temperature for photo-thermal ablation. Woven CFRP showed slightly narrower kerf width but much shallower machining depth than cross-ply CFRP. At an energy density of approximately 30 J/mm^2, IM7 showed a depth of 685 µm compared to just 355 µm for AS4. Thermal damage for woven CFRP was directionally dependent, with HAZ width varying with the local value for θ. The HAZ was maximized for θ = 90° and minimized for θ = 0°; HAZ widths shown in Figure 4-6b are measured for θ = 0°.

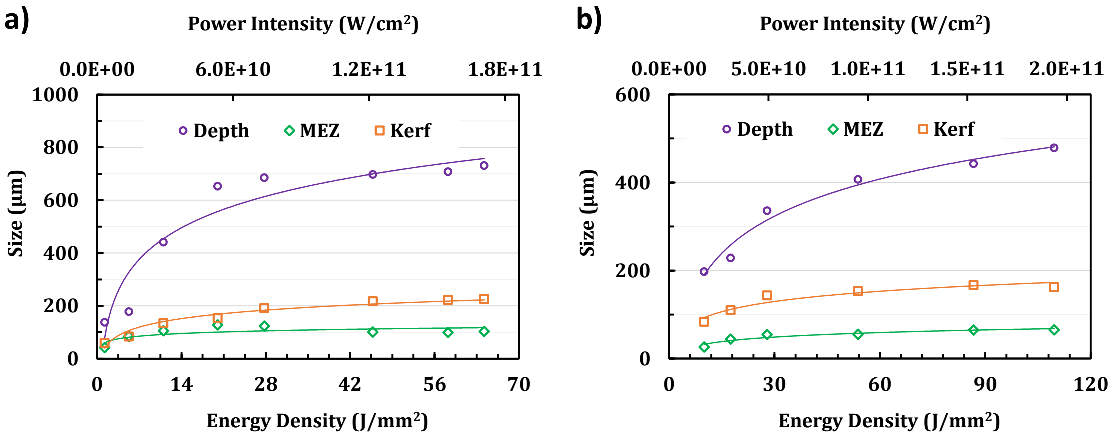

Figure 4-6: Machining results from tests in LP mode for increasing laser power for (a) cross-ply IM7 CFRP and (b) woven AS4 CFRP. Results show a logarithmic relationship with both energy density and power intensity. Note: HAZ width for woven AS4 is measured for θ = 0° local fiber direction.

4.4.2 Scanning Velocity and Pulse Overlap

Results for tests investigating scanning velocity and pulse overlap are summarized in Figure 4-7. Decreasing scanning speed from 1.0 mm/s to 0.4 mm/s for 100 µm spot diameter increases pulse overlap from 0% to 50%. In the case of cross-ply samples, θ changes as the laser beam penetrates multiple laminate layers, rendering machining depth measurements using confocal microscopy inaccurate. As less laser light is reflected at greater depths, measurements become increasingly unreliable and contain significant uncertainty. Kerf width is largely unaffected by pulse overlap given the high ablation threshold and conductivity of the carbon filaments. However, increasing pulse overlap from 0% to 50% increased the HAZ width from 340 μm to 402 μm with a significant increase in the cutting depth.

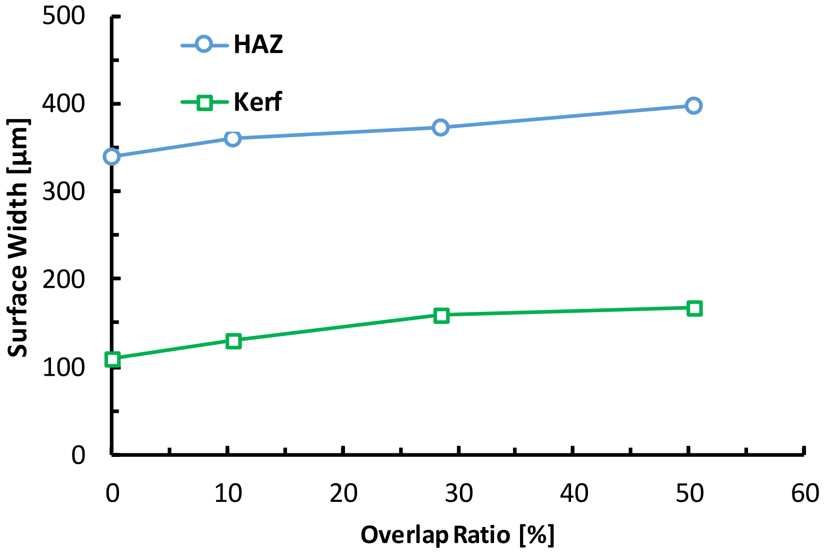

Figure 4-7: Surface machining results from tests in LP mode for increasing pulse overlap using cross-ply IM7 CFRP. Machining depth measurements at greater depths become unreliable using confocal microscopy.

As pulse overlap increases, successive pulses contact the CFRP material inside the trench rather than at the surface, increasing total incident energy absorption and increasing the effective ablation rate. The additional energy absorption gradually expands the HAZ region by heat accumulation. Pulse overlap also has a significant effect on the trench profile, as seen in Figure 4-8 and Figure 4-9. Scanning at 1.0 mm/s for a frequency of 10 Hz and 40 μm spot diameter generates pulses that are spaced 100 μm from center to center with a measurable gap. This produces a plateau effect where depth is maximized within the laser pulse area and minimized in the gap between pulses (Figure 4-8). In this case, machining depth was measured within the laser pulse area at the maximum value. Fiber pull-out was observed in all laser machining tests similar to Figure 4-8b. Fibers become dislodged from the internal machined surface, particularly in the bottom of the trench between laminate layers. These fibers are not sublimated or ejected as the laser scans the cutting path. This is a consequence of NIR-wavelength laser irradiation for CFRP machining, as the transmissivity of matrix materials in the NIR spectrum approaches 90%. Laser light is allowed to pass through the matrix to be absorbed by the fibers. The fibers are heated below sublimation temperature and conduct heat along the fiber axis. This heat is sufficient to damage or remove the matrix near the internal machined wall. Increased pulse overlap results in a smoother kerf edge, shown in Figure 4-9. As the overlap ratio decreases, an undesirable jagged edge is produced due to striations formed by the circular laser spot. The spacing of these striations along the cutting path direction is approximately equal to the center-to-center spacing of the pulses; 100 μm in Figure 4-8b and 40 μm in Figure 4-9b.

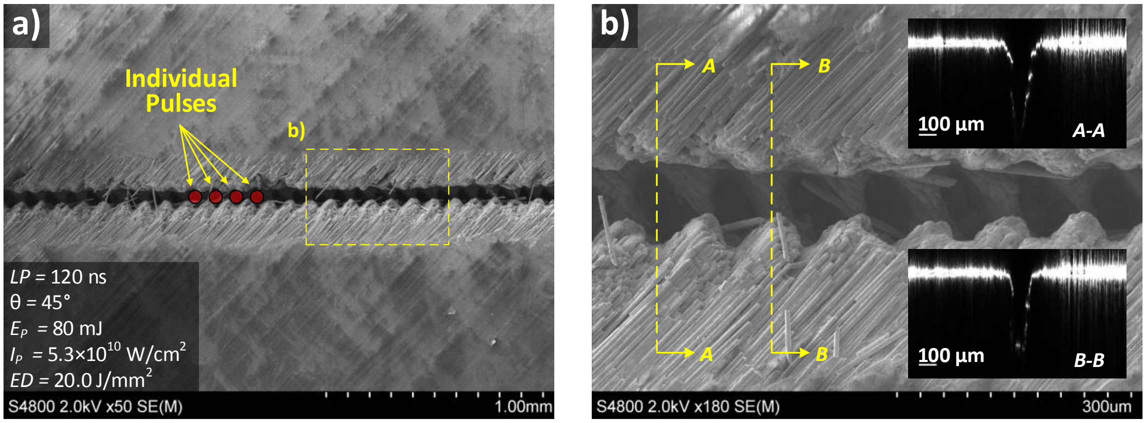

Figure 4-8: Imaging of laser cutting of cross-ply CFRP using LP mode: (a) surface micrograph showing typical single-pass machining zone; (b) close-up view showing severe striations from individual pulses; cross sections show greatest depth at laser spot area (A-A) and shallow depth between pulses (B-B).

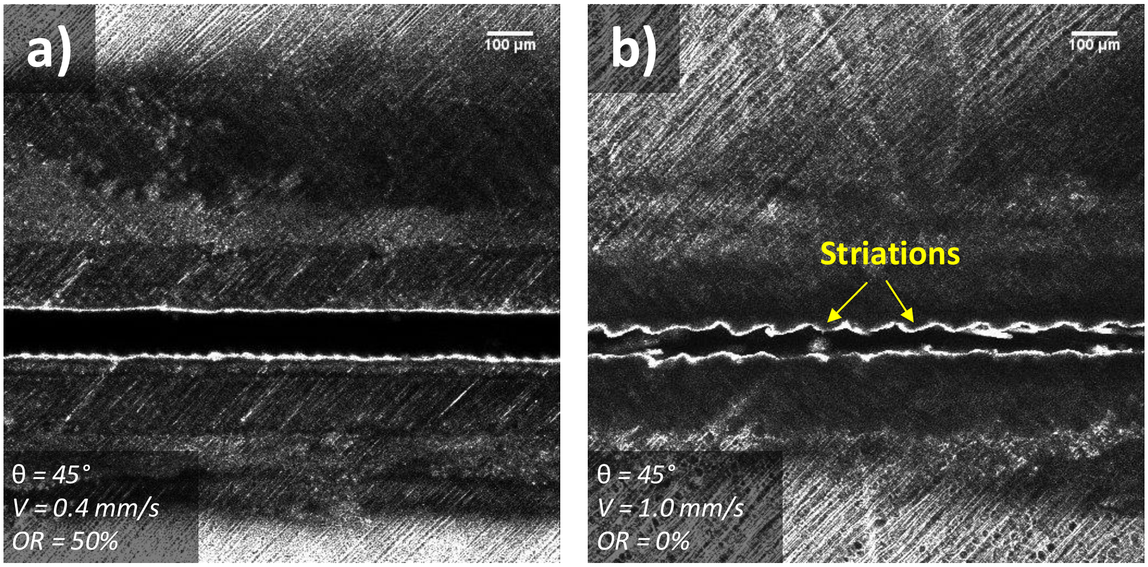

Figure 4-9: Confocal surface imaging: (a) OR = 50%; (b) OR = 0%. Increased pulse overlap produces smoother machined edge with kerf and HAZ width increasing according to the energy density.

4.4.3 Cross-Ply Fiber Orientation

Figure 4-10 compares cross-ply IM7 CFRP for fiber directions of θ = 0° and θ = 90° relative to the laser scanning path. Kerf width and machined depth are unaffected by fiber direction. However, HAZ width increases significantly for θ = 90° as seen in Figure 4-11. Matrix recession is very extensive with large areas of exposed fibers. As θ increases, energy is conducted away from the machining zone and into the surrounding bulk material. Thermal damage was reduced in Figure 4-12 for θ = 0°. In this case, energy is conducted along the laser scanning path. However, machining quality is severely degraded with extensive fiber pull-out. Fiber pull-out and matrix recession at the internal machined surface is attributed to the absorption properties of the matrix for IR irradiation, as previously discussed. Loose fibers partially obstructed laser light reflection, adding uncertainty to depth measurements.

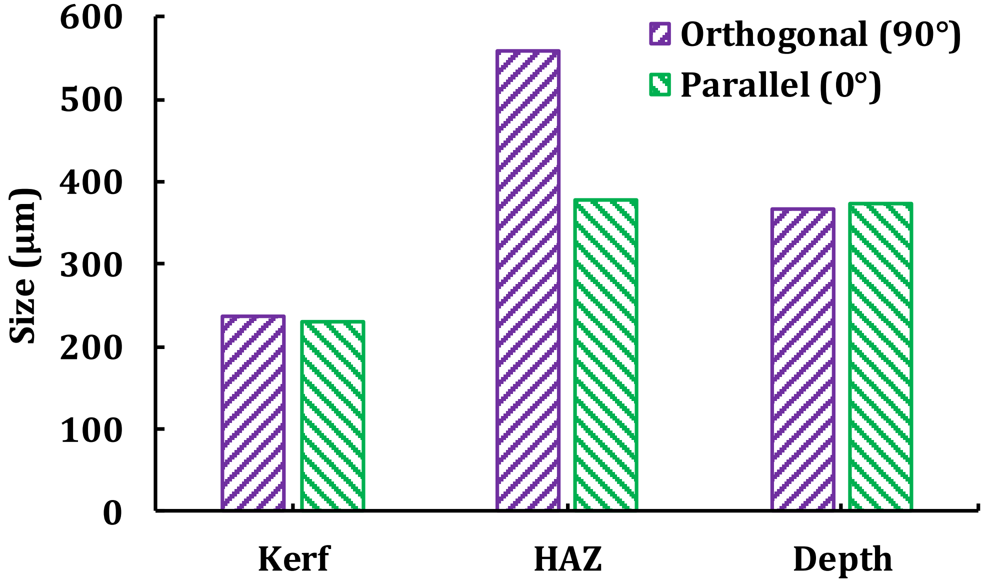

Figure 4-10: Results from tests in LP mode comparing surface fiber direction for cross-ply IM7 CFRP. Surface HAZ width increases significantly with increasing θ.

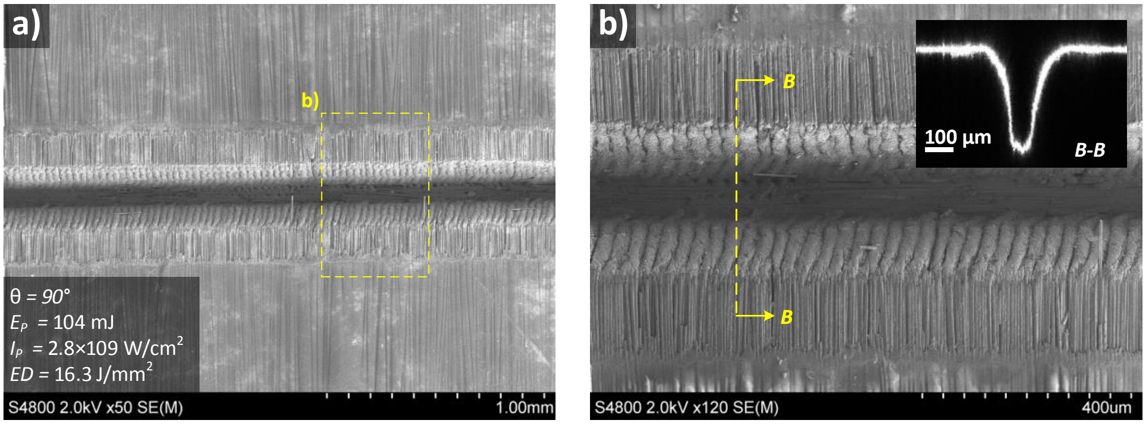

Figure 4-11: Imaging of laser cutting of cross-ply CFRP using LP mode investigating surface fiber direction of θ = 90°: (a) SEM micrograph showing extensive thermal damage; (b) close-up view of machining zone showing surface roughness. Cross section B-B shows no fiber pull-out.

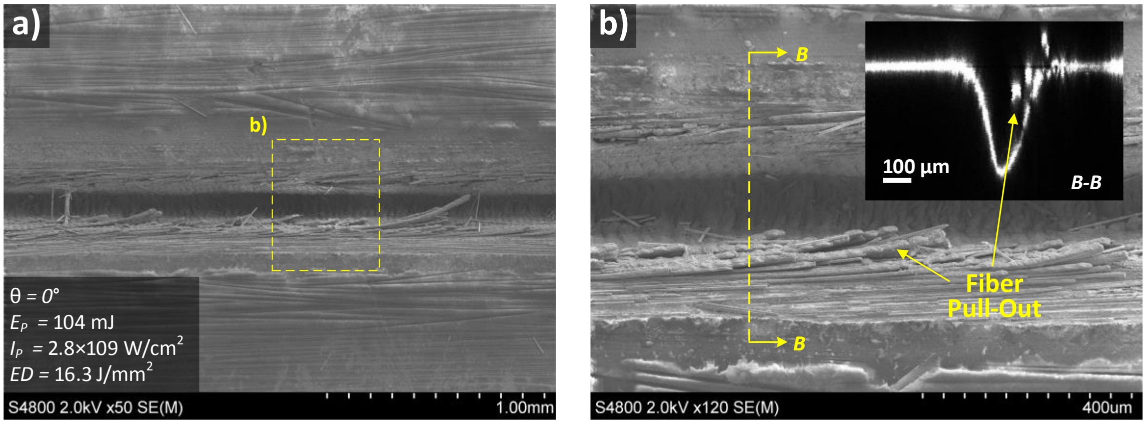

Figure 4-12: Imaging of laser cutting of cross-ply CFRP using LP mode investigating surface fiber direction of θ = 0°: (a) SEM micrograph showing reduced HAZ width (b) close-up view of machining zone showing extensive internal fiber pull-out. Cross section B-B shows effect of fiber pull-out on depth measurement.

4.4.4 Multi-Pass Cutting of CFRP

Kerf and HAZ measurements after multiple laser passes along the scanning path are summarized in Figure 4-13. The entry surface is only slightly affected by additional laser passes since laser-material interaction occurs deep within the trench. Confocal depth measurement is completely ineffective due to the absence of light reflection. As few as 10 laser passes were required to partially machine through the material, shown in Figure 4-14a. Figure 4-14b shows that 20 passes produces a similarly discontinuous exit kerf approximately 23µm wide. Using 50 laser passes machined a continuous trench with an exit kerf width of 58 µm, shown in Figure 4-14c. There is also considerable tapering between the entry and exit surfaces.

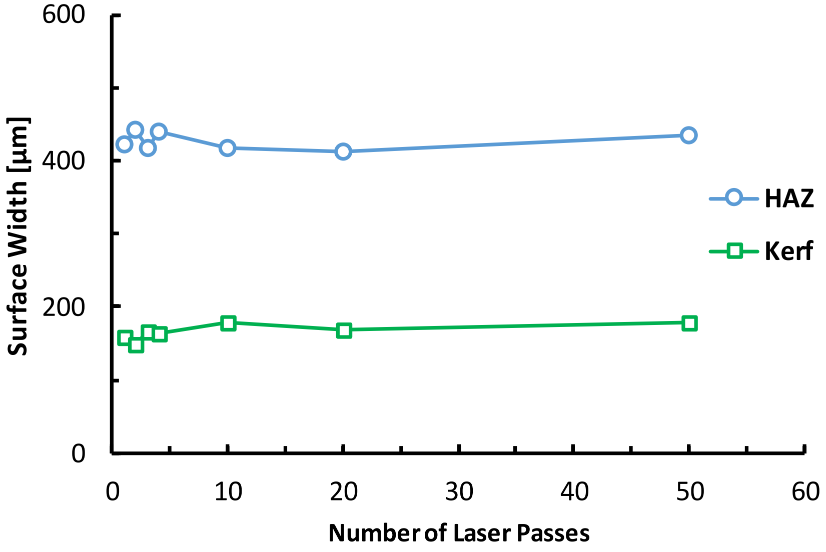

Figure 4-13: Machining results for multiple laser passes using Long Pulse mode: (a) cutting depth measured using confocal microscope; (b) surface HAZ and kerf widths measured at entry surface.

A staircase profile was generated using a contour cutting process to allow for surface integrity analysis using SEM as shown in Figure 4-15 and Figure 4-16. Starting at the top CFRP surface, the first pocket was machined using one laser scan over the cutting path. Then, the working distance was adjusted to lower the laser focal plane onto the machined surface. The second pocket was also machined using one laser scan. After another adjustment of the working distance, the through-cut was achieved using two laser scans over the cutting path. Exposed machined wall surfaces show horizontal marks indicating different laminate layers (Figure 4-15b). The fiber orientation varies between laminate layers in cross-ply CFRP. Thermal damage is observed along internal machined edges in the form of matrix recession (Figure 4-15c). Closer examination of the machined surfaces reveals bundles of fibers separated at a distance corresponding to the hatching distance of the laser scan path (Figure 4-16a). Fiber swelling is observed throughout, particularly where fiber pull-out has occurred. Also, matrix re-solidification is seen at the ends of these fiber bundles near the machined surfaces. The re-solidified matrix has essentially fused the ends of these bundles together to form a larger strand. Fiber pull-out is extensive and intensifies where the local fiber orientation relative to the cutting path approaches 0° (Figure 4-16b). Striations are visible along machined surfaces, with the spacing along the cutting direction approximately equal to the center spacing of the pulses, which is 50 μm for 0.5 mm/s scan speed and 10 Hz repetition rate (Figure 4-16c).

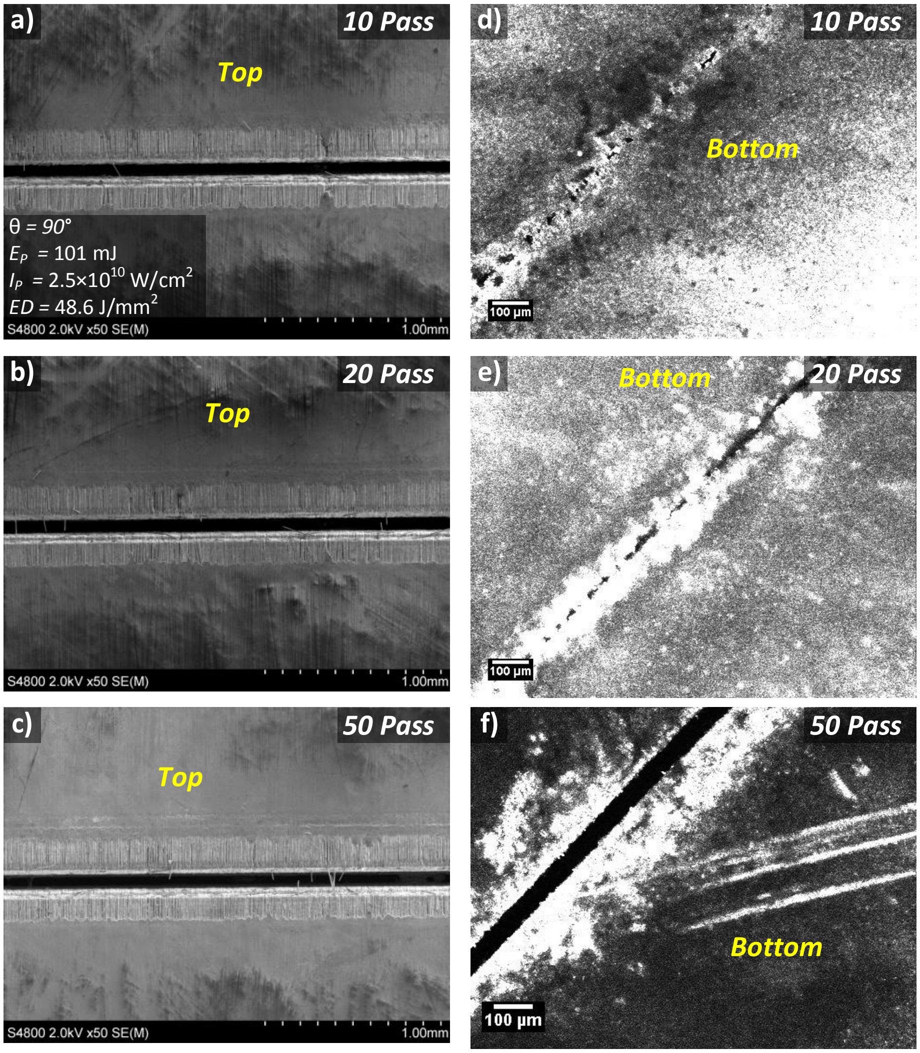

Figure 4-14: Imaging of multi-pass laser cutting for cross-ply CFRP using LP mode: (a-c) entry surface SEM micrographs for 10, 20, and 50 passes, respectively; (d-f) exit surface confocal micrographs for 10, 20, and 50 passes, respectively. Results show that at least 20 passes are required to machine through CFRP.

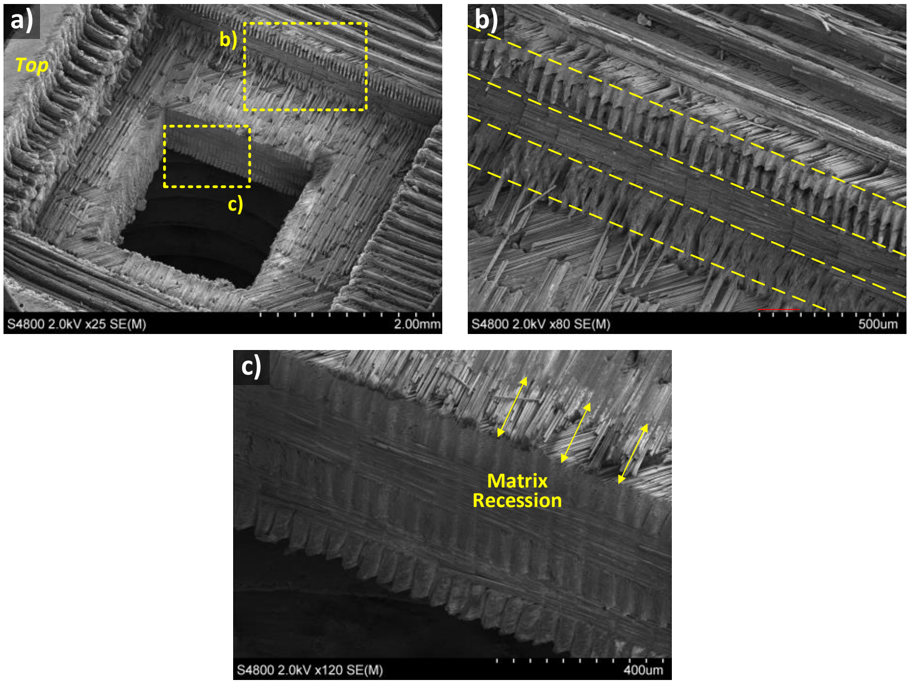

Figure 4-15: Micrographs of contour cutting of cross-ply CFRP: (a) Laser pocketing with square through-cut profile; (b) exposed wall showing fiber orientations in different laminate layers; (c) matrix recession along internal machined edge with visible striations.

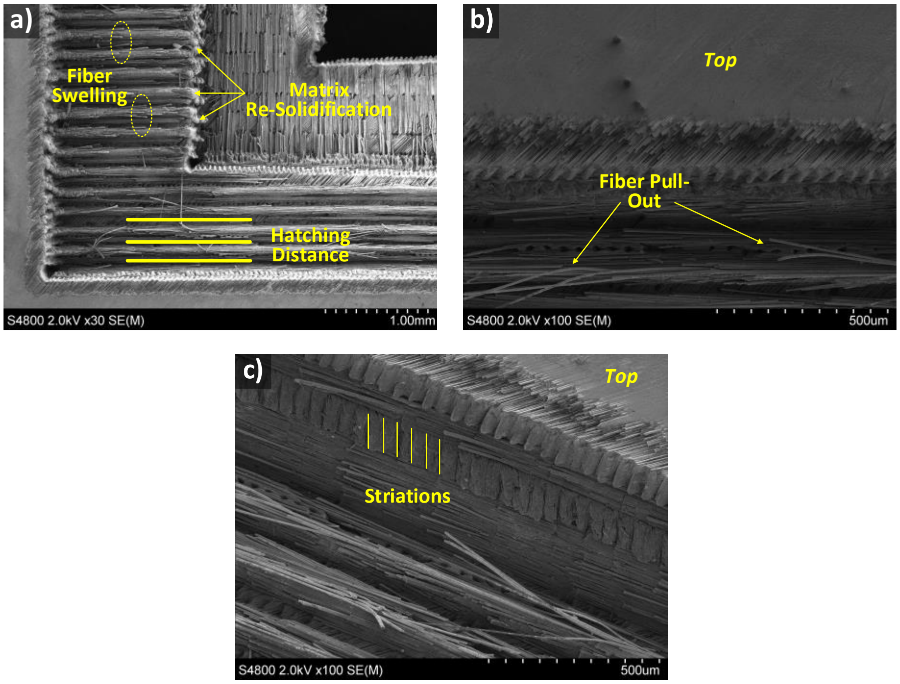

Figure 4-16: Micrographs of contour cutting of cross-ply CFRP: (a) fiber bundle spacing corresponds to hatching distance of laser scan path with noticeable fiber swelling and matrix re-solidification; (b) fiber pull-out is extensive, particularly where the local θ approaches 0°; (c) striations are visible along machined surfaces.

4.4.5 Contour Drilling of CFRP

Figure 4-17 shows a laser drilled hole 4 mm in diameter machined using a standard trepanning technique on cross-ply IM7 CFRP. The fiber orientation is variable along the laser scan path. As θ sweeps between 0° and 90°, the HAZ width varies accordingly. In Figure 4-17(b), where $\theta = 90°$, the HAZ region extends approximately 300 µm from the kerf edge. In Figure 4-17(c), where $\theta = 0°$, the HAZ extension is reduced to 120 µm. Similar results were seen in other laser drilling results, which are shown in Figure 4-18 for both CFRP materials. Laser drilling of woven CFRP samples showed significant charring, particularly at the entry surface (Figure 4-18a-b) while cross-ply samples resulted in less thermal damage with only slight charring at the kerf edge (Figure 4-18c-d). Laser drilling of woven samples of 2.2 mm thickness was achieved using as few as 5 passes at the expense of thermal damage. This was accomplished at maximum laser power with a power intensity of 5.0×10^{10} W/cm^2 and an energy density of 120 J/mm^2.

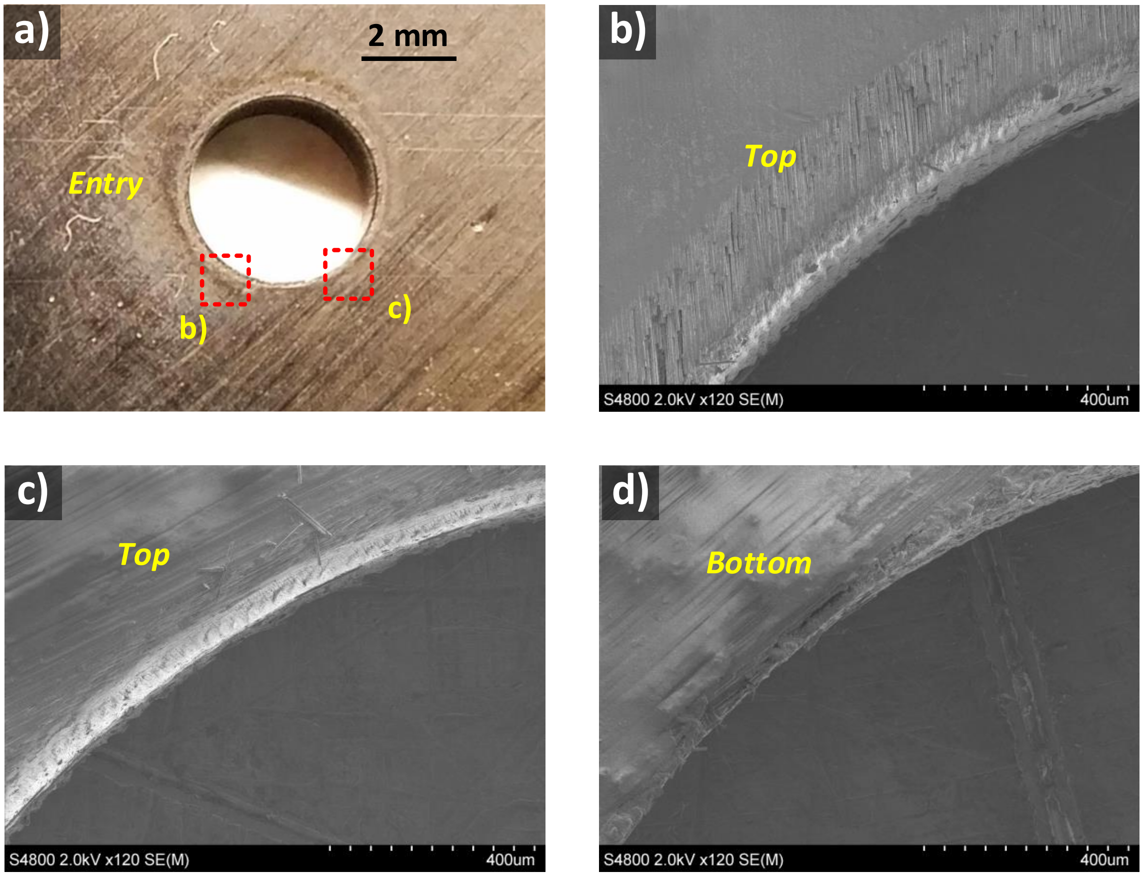

Figure 4-17: Laser drilling experiment of cross-ply CFRP after 20 laser passes. (a) Laser drilled hole entry surface; (b) micrograph at the left corner of the hole entrance with orthogonal local fiber orientation relative to cutting path; (c) micrograph at the right corner of the hole entrance with parallel local fiber orientation relative to cutting path.

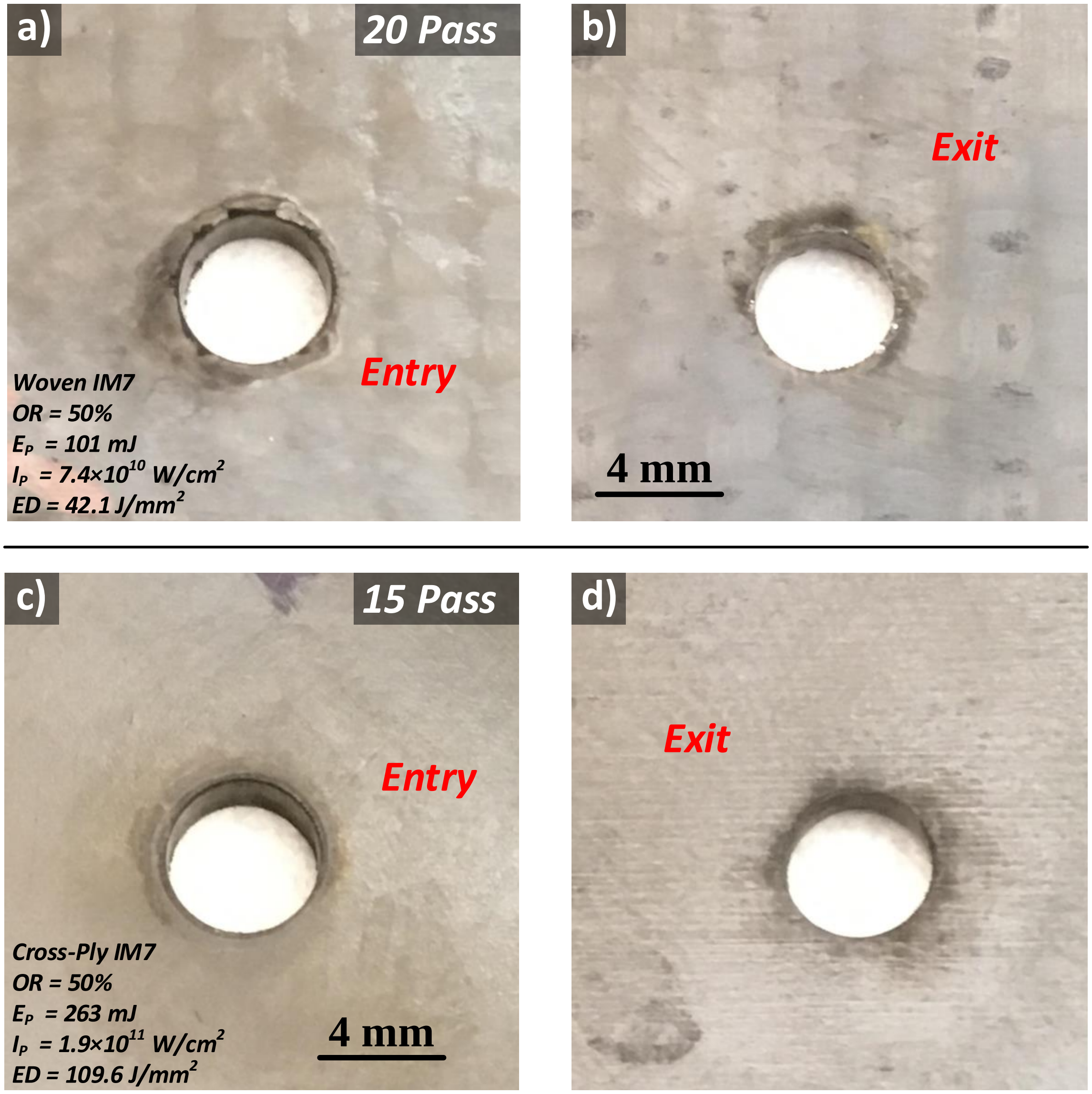

Figure 4-18: Images of laser drilling of CFRP: (a) and (b) woven CFRP after 20 passes showing charring and burning at hole contour edge; (c) and (d) cross-ply CFRP after 15 passes showing reduced charring and improved quality.

4.4 Discussions

4.4.1 Nanosecond Pulsed Laser vs. CW/Modulated Laser

The experiments in Chapter 4 highlight the performance and flexibility that is possible by laser machining. The experimental results provide insight into the energy absorption mechanisms and the factors that affect the finished product. Laser ablation observed using both the Yb:YAG fiber laser from Chapter 3 and the high energy Nd:YAG laser from Chapter 4 is characterized as photo-thermal. This is the result of two main factors.

First, the laser-induced excitation rates were low relative to the thermal response time of the carbon-based fiber reinforcements, which is on the order of 10^{-13} seconds according to Kampfrath et al. (2005) and Ishioka et al. (2008). Microsecond-pulsed laser machining in Chapter 3 showed unacceptable results due to long pulse duration (0.01 ms), resulting in conduction-based material removal where heat accumulation leads to fiber ablation and HAZ expansion. Long-Pulse nanosecond laser machining in Chapter 4 showed better quality using shorter pulse duration (120 ns) and low frequency (10 Hz) using power intensity (over 10^{10} W/cm^2). The machined profiles resemble a keyhole-mode laser removal process, where a high vapor pressure forms due to the intense plasma formed by ablated fibers. This vapor pressure pushes outward to form a deep and narrow kerf, made possible by the elevated power intensity and short pulse duration of the high energy nanosecond laser. This advantage is clearly seen in Figure 4-19 by comparing the machining depths of both laser systems. At an energy density of approximately 20 J/mm^2, the power intensity of the Yb:YAG laser was 1.8×10^7 W/cm^2 and 5.0×10^9 W/cm^2 for the Nd:YAG laser. Therefore, the single-pass machining depth increased from 218 μm to 652 µm for each laser, respectively. The difference in machining depth becomes more apparent for higher energy density.

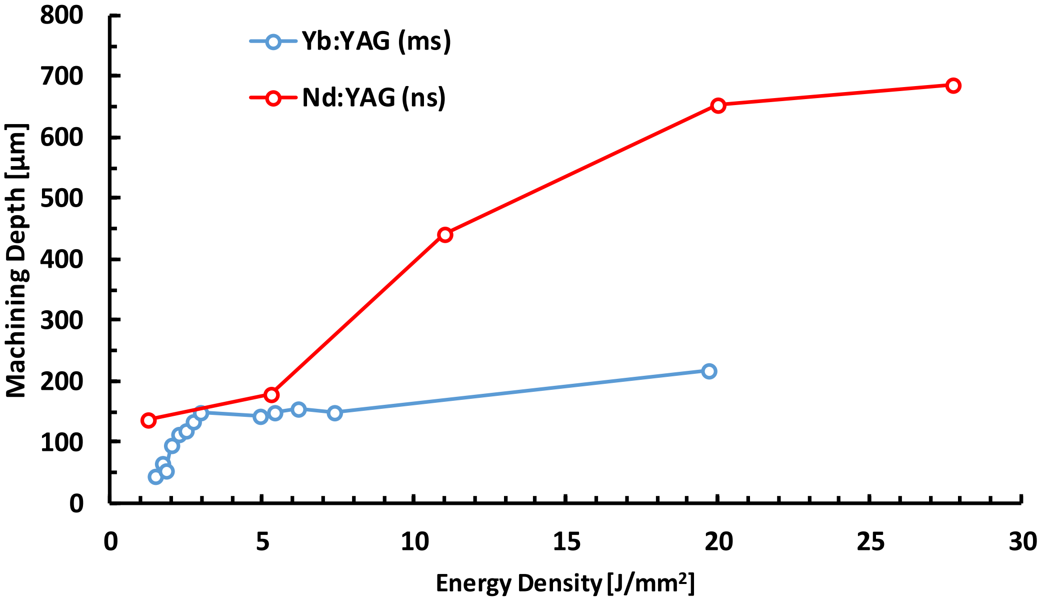

Figure 4-19: Single-pass machining depth comparison of a range of energy density levels for Yb:YAG fiber laser with microsecond pulsing and high energy Nd:YAG laser with nanosecond pulsing. The shorter pulse duration and higher power intensity of the Nd:YAG laser results in keyhole-mode material removal for CFRP sample.

The second factor is laser wavelength; both laser systems used in this study emit at fundamental wavelengths of either 1064 nm or 1070 nm. The photon energy of laser irradiation in the NIR spectrum is approximately 1.17 eV, which is below the bond energy of carbon of 3.49 eV. Also, the CFRP matrix is largely transparent for for ~1064 nm wavelengths, with transmissivity values above 85% and low optical absorption coefficients for many common matrix materials (Abbas and Ali (2014), McKie and Addison, (1994), Völkermeyer et al. (2011)). Laser light is allowed to directly pass through the matrix material to be absorbed by fibers conducted away from the machining zone (Figure 4-20a).

This increases the size and severity of the HAZ region and other thermal damage such geometric deformation and fiber swelling. Lasers emitting in the UV spectrum drastically reduce thermal damage due to irradiation being absorbed directly by the matrix material (Figure 4-20b). The absorption characteristics of the CFRP matrix might also explain the reduced machining depth observed in single-pass cutting of woven CFRP. For cross-ply CFRP, the laser light is able to penetrate deep into the target area, particularly within the first laminate layer, given that the matrix can be upwards of 90% transmissive and all fibers within a single laminate layer are of the same direction, θ. In the case of woven CFRP, the weave pattern can potentially obstruct the penetration of laser irradiation through the matrix and subsequent absorption by the fibers as the fiber orientation angle, θ, is not constant within a laminate layer; further examination is required. Additionally, machining of woven CFRP samples using the Nd:YAG laser in Chapter 4 did not exhibit the same kerf discontinuities near the weave boundaries as seen in Chapter 3. It is hypothesized that the keyhole-mode CFRP laser machining process sufficiently improves the efficiency of the material removal mechanism to eliminate this phenomenon.

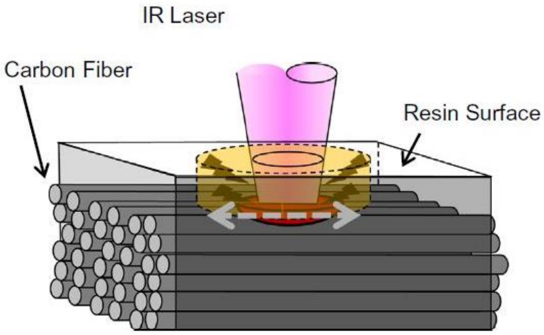

Figure 4-20: Illustration of IR laser-material interaction for CFRP. For laser irradiance in the NIR spectrum (i.e. 1064 nm), the matrix is largely transparent; laser energy passes through the resin surface to be absorbed by the underlying fibers. Heat is conducted along the fiber axes to indirectly heat the adjacent bulk matrix (Takahashi et al., 2016).

4.4.2 LP Mode vs. QSW Mode

The drastic difference in cutting performance between Long-Pulse (LP) and Q-Switch (QSW) pulse modes is attributed to the fundamental change of laser-material interaction when different pulse durations are applied. A hypothesized explanation will be given next for the different performances of laser cutting using LP mode or QSW mode. In this study, power intensity during Q-Switch trials ranged from 5.5×10^{10} W/cm^2 to 1.3×10^{12} W/cm^2. At such power intensity, laser-induced plasma effects become significant. Photon absorption in laser-induced plasma by the inverse Bremsstrahlung mechanism primarily manifests in two ways: (1) optical breakdown of the gas environment above the target area and (2) shielding of the ablated CFRP material (Russo et al. (2007), Brown and Arnold (2010)).

Laser-induced optical breakdown of the gas environment above the target area might occur for the power intensity levels used in our QSW experiments. This threshold intensity was experimentally measured by Thiyagarajan and Thompson (2012) using a Nd:YAG laser with 6 ns pulses based on the multiphoton ionization theory. They found that the threshold was inversely proportional to wavelength, as predicted by Kroll and Watson (1972), with laser-induced optical breakdown for 1064 nm wavelength occurring above 4.42×10^{9} W/cm^2. Intense photon absorption by laser-induced plasma as a result of optical breakdown was observed by Wu et al. (2015). Their study found that laser machining of CFRP was ineffective using a 1064 nm Nd:YAG laser with 10 ns pulses at a power intensity of 3×10^{9} W/cm^2 in a standard air environment, which they attributed to laser-induced breakdown. They also observed that laser machining was effective using 200 ns pulses at a reduced power intensity of 1.5×10^{8} W/cm^2 for the same laser system. In our study, this laser-induced breakdown could lead to the generation of plasma consisting of ionized Argon and/or ionized target material. The formed plasma could be highly absorptive of the laser beam.

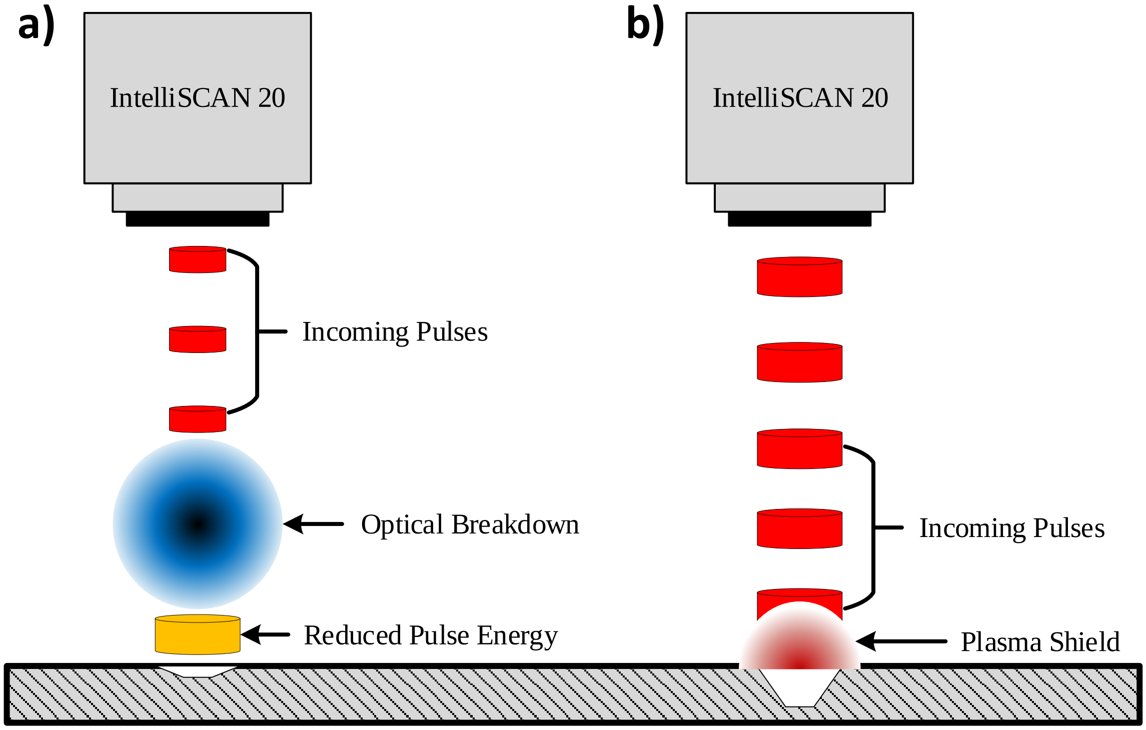

Figure 4-21: Illustration of laser-induced plasma energy absorption. (a) Optical breakdown: significant portion of incoming pulse energy is absorbed by plasma plume above CFRP workpiece, resulting pulses are de-focused (b) Plasma shielding: plasma expansion plume absorbs remaining laser pulse energy after plasma ignition has begun.

Previous work has measured as much as 80% absorption of the incident energy using an excimer laser (Schittenhelm et al., 1996), attributed to the inverse Bremsstrahlung mechanism (Sankaranarayanan and Kar (1999), Morgan (1975)). This plasma might also tend to de-focus, further reducing the incident power intensity as illustrated in Figure 4-21a. Therefore, the laser beam cannot penetrate very deep into the CFRP target with a reduced intensity. At such a reduced power intensity, photo-thermal ablation might be prevented due to the fibers do not absorb sufficient energy to reach sublimation temperature. As a result, material removal can only occur near the target surface and only a shallow cutting depth is produced in QSW mode.

For our laser setup, optical breakdown in QSW mode might be avoided by reducing power intensity below the estimates and observation provided by the literature. This could be accomplished by reducing the power intensity or enlarging the spot diameter. However, enlarging the spot diameter to a minimum of 140 µm is required at minimum laser power (~5 mJ pulse energy) to reduce the power intensity below 4.4×10^9 W/cm^2. This would widen the kerf and also reduce the energy density, limiting the ablation rate and lengthening processing time. Optical breakdown was not observed in Long Pulse (LP) mode likely due to the longer pulse duration of 120 ns, which theoretically raises the threshold power intensity.

The surface is shielded by the plasma plume formed by ionized CFRP material during the ignition stage of the ablation process. This plasma plume absorbs some of the photon energy from the incoming laser pulse when the duration is in the nanosecond domain, illustrated in Figure 4-21b. Plasma shielding can be avoided using durations in the picosecond or femtosecond domain (Zeng et al., 2005), where the energy delivery to the target area effectively outpaces plasma formation. Additionally, ultra-short pulsing reduces thermal diffusion (Eland et al., 2001). The presence of plasma shielding also helps explain results from Chapters 3 and 4 regarding the relationship between laser energy density and machining performance. The expanding plasma plume formed during the ignition phase of the CFRP laser ablation process shields the target area and absorbs incoming photon energy. This decreases the ablation rate until a saturation point is reached (Borisov et al., 1998), evidenced by the logarithmic trend observed in the machining depth measurements.

Shielding of the target area increases until more laser input does not result in more CFRP material being ablated.

The effects of laser-induced optical breakdown and plasma shielding combine to make QSW mode ineffective for laser machining of CFRP. Effective laser machining was observed in all tests using LP mode. Similar results were observed for the CW/modulated Yb:YAG fiber laser in Chapter 3 due to power intensity on the order of 10^6 to 10^7 W/cm^2 and pulse duration in the microsecond domain.

The mechanism of keyhole cutting of CFRP using a long-duration nanosecond pulse laser seen in Figure 4-4 is different from that of the CW laser cutting of metal alloys. Keyhole laser cutting is usually achieved for metal alloys using continuous-wave (CW) lasers, e.g., CO_2 laser cutting of mild steels. Preissig et al. (1994) summarized that the keyhole is usually caused by vapor pressure due to the intense laser irradiation and multiple laser ray reflections in those processes, where the local vapor pressure creates, deepens, and maintains the keyhole during the laser cutting. The keyhole mode laser cutting of metals can be more efficient than classical laser cutting techniques, because the melt can be removed much more efficiently from the center line in the cut front. This makes the melt film thinner to ensure efficient heat conduction from the melt surface. However, the molten material film is unlikely to be developed in this study due to the limited energy input over a short duration for a nanosecond pulse laser.

For the CFRP target, the linear optical absorption coefficient of the polymer matrix is expected to be relatively low. Transmissivity of the thermoplastic matrix material of CFRP is very high at the nanosecond pulse laser wavelength of 1064 nm, as previously discussed. Even though carbon fibers exist in CFRP, the overall linear optical absorption coefficient of the CFRP target may still be relatively low. Therefore, when LP mode was used in this study, where the laser beam intensities were much lower than those for QSW mode, the laser beam could penetrate into a relatively deep region below the CFRP target surface. As a result, the laser beam energy could be absorbed by a relatively thick layer of the target material. Much of the laser energy is absorbed along the depth by the carbon fibers, with a high absorptivity for 1064 nm wavelength. The absorbed laser energy may elevate the target material temperature, cause phase transformations, induce material removal from the target, and eventually produce a relatively large cutting depth. Therefore, a new type of keyhole laser cutting is achieved for CFRP using the long-duration nanosecond pulse laser. It should be noted that future work may still be needed to further verify the above hypothesized explanation and also check whether or not other mechanism(s) has also played an important role.

4.4.3 Comparisons of Machining Performance

Comparing mechanical drilling results from Chapter 2 to laser contour drilling in Chapter 4 reveals several advantages of laser materials processing, including automated and flexible path planning, improved machining quality, and precise control of parameters. Machining performance using the high-energy nanosecond laser system is far superior to mechanical machining, shown in the comparison in Figure 4-22. Delamination and peeling is eliminated, while the high energy nanosecond laser uses short pulse duration and higher power intensity to remove the CFRP material efficiently. Complex features can be created using an automated laser scan head by programming a precise laser cutting path, as seen in multi-pass pocketing from Section 4.4.4. Features can be machined mechanically using milling tools, but are limited by tool size and experience detrimental effects similar to Figure 4-22a-b.

Quantifying laser machining quality for CFRP has not been thoroughly explored by researchers. As previously discussed in Section 1, drilling quality criteria is governed by ISO 286 standards in the aerospace industry. These standards are based solely on physical diametrical tolerances; laser drilling quality is more complex due to the thermal nature of the process and has an extended effect on surface integrity. Caprino and Tagliaferri (1988) suggested a three-class system based on two main criteria: (1) the kerf width relative to the laser spot diameter and (2) the HAZ width, in particular, matrix recession and charring. In general, using their system based on approximations for results in Figure 4-22c by SEM imaging, laser drilling using a high-energy nanosecond-pulsed IR laser system can be categorized as either Class A or B, indicating moderate to high quality.

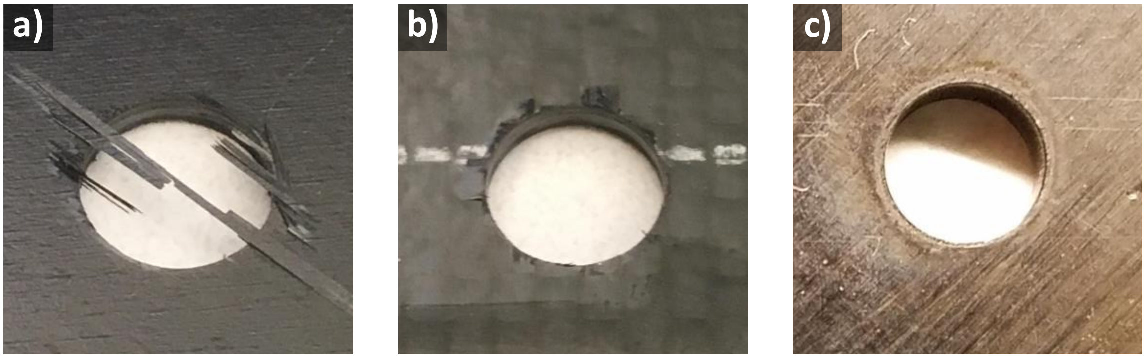

Figure 4-22: Comparison of CFRP machining results: (a) SPF drill showing delamination; (b) DAL drill showing burring and peeling; (c) high-energy nanosecond Nd:YAG laser system.

Comparing results from the CW/modulated fiber laser and the high energy nanosecond laser in Figure 4-23, there is a clear improvement in laser machining quality.

Using the fiber laser in CW mode in Figure 4-23a shows a very wide kerf and extensive matrix evaporation. Microsecond pulsing in Figure 4-23b using the fiber laser produces a narrower kerf and an improvement in thermal damage, although the HAZ is still over 500 µm wide in some areas. Optimum results are observed for the high energy nanosecond laser in Figure 4-23c where thermal damage is minimized using short duration pulsing and high power intensity for efficient laser ablation.

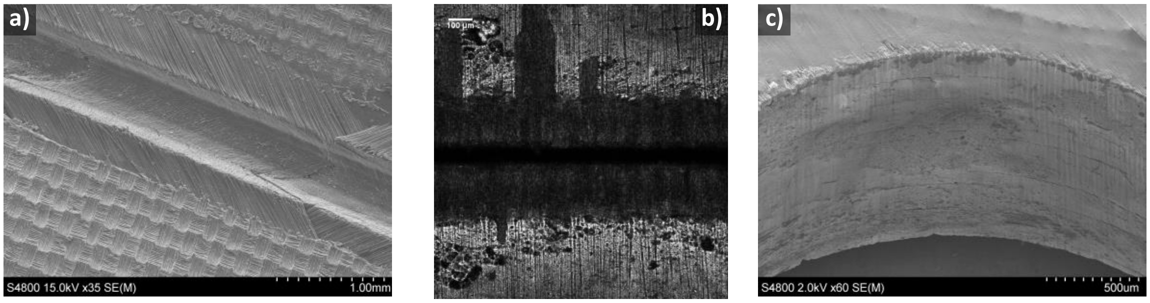

Figure 4-23: Comparison of CFRP machining results: Yb:YAG fiber laser in (a) CW mode and (b) pulse mode with 0.1 ms duration; (c) nanosecond Nd:YAG laser with minimal thermal damage during drilling.

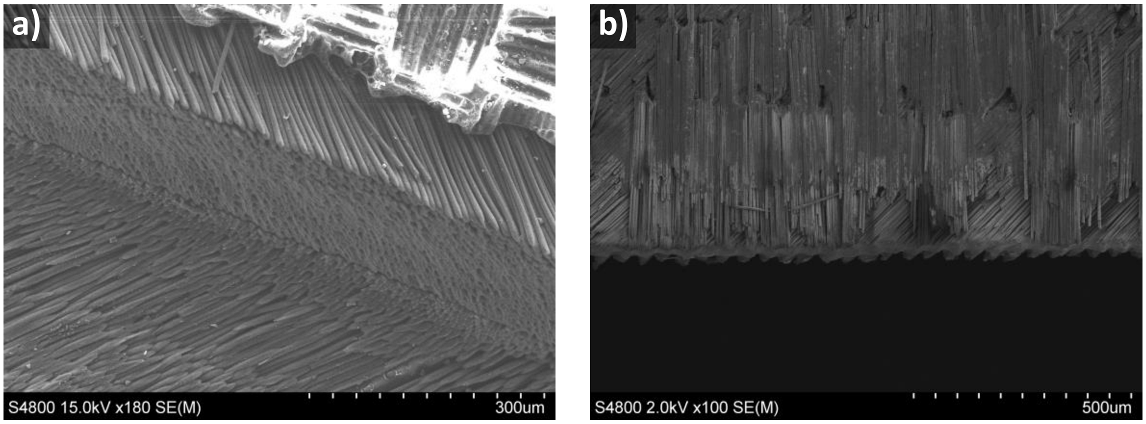

Figure 4-24: Comparison of CFRP laser machining results: (a) CW Yb:YAG fiber laser showing fiber swelling near machined profile (b) high-energy nanosecond Nd:YAG laser showing reduced fiber swelling near machined profile.

Along with the molecular purity of the fiber reinforcement material, fiber swelling could be a direct result of thermal expansion at the cut ends due to the elevated temperatures during laser ablation. Swelling was very apparent in SEM imaging of results using the Yb:YAG fiber laser, particularly when used in CW mode. Laser-material interaction is constant, with no cycle time to allow for workpiece cooling (Figure 4-24a). Temperature gradients within the epoxy matrix in and around the target area are greatest in CW mode. Fiber swelling was reduced for the nanosecond laser where the laser-material interaction time is shortened and subsequent heat conduction is reduced (Figure 4-24b). The short pulse duration transfers the laser beam energy to fibers in the target area more efficiently and reduces temperature gradients in areas along the target area.

Experiments in Chapter 4 demonstrated the effect of an inert assist gas. Laser contour drilling in Section 4.4.5 was performed with an Argon assist gas flow; multi-pass pocketing in Section 4.4.4 was performed without assist gas in an open air environment. A comparison is shown below in Figure 4-25, where there is a clear improvement in surface quality when using Argon assist gas. The Argon flow prevents oxidation reactions at the machined surface and improves surface integrity (Figure 4-25a), similar to results seen by (Rodden, 2002), (Negarestani et al., 2010), and (Riveiro et al., 2012) comparing inert assist gas to mixed reactive assist gas. The oxygen in the open air environment enhances thermal decomposition during the heating stage of photo-thermal laser ablation. Charring and build-up of re-solidified epoxy matrix can be observed at the ends of fiber bundles (Figure 4-25b) and at the exit surface of the pocket profile (Figure 4-25c).

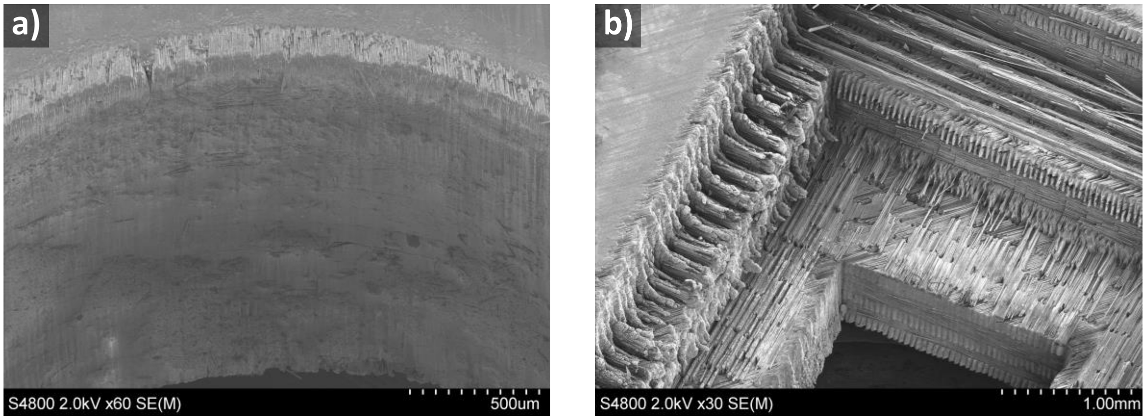

Figure 4-25: Comparison of CFRP machining experiments: (a) laser drilling with Argon assist gas flow; (b) laser pocketing with no assist gas in open air environment.

4.5 Conclusions

From the experiments in Chapter 4, it is clear that high energy nanosecond IR laser systems can effectively machine CFRP with reduced thermal damage. This experimental study demonstrates for the first time that keyhole-mode cutting can be achieved for CFRP using a high-energy long-duration nanosecond laser system. The formation of the keyhole-shaped trench is attributed to laser ablation of the fibers and matrix materials via deep penetration of the laser energy, partially due to the transmissivity of the matrix in the NIR spectrum. Inverse Bremsstrahlung photon absorption by laser-induced plasma had a significant impact on machining performance. Laser machining in Q-Switch mode suffered from optical breakdown above target area, with sufficient absorption and de-focusing to render the ablation process ineffective. Optical breakdown was avoided in Long Pulse mode by using lower power intensity from increased pulse duration. Plasma shielding was observed in Long Pulse mode, with a measurable effect on the ablation rate for increasing laser irradiance. The effect reached saturation for high levels of irradiance where the ablation laser ablation reached a local maximum.

A logarithmic relationship was applied to machining dimensions using energy density to identify critical values for effective laser ablation for both types of CFRP. The logarithmic trend was attributed to a saturation effect from plasma shielding on the ablation rate. Cutting depth was lower for woven AS4 CFRP, likely due to increased thermal properties and the reduced of penetration depth of IR irradiation through a woven fiber structure. As expected, increased pulse overlap increases cutting depth and improves pulse feed striations. Likewise, heat conduction is favored heavily along the fiber axis, which extends the HAZ width when scanning orthogonally to the surface fiber direction. Machining depth measurements at greater depths, particularly when using multiple laser scans, was inconclusive due to the limitations of the CLSM measurement system and fiber pull-out between cross-ply laminate layers. Additional laser passes had a limited effect on the HAZ and kerf width. Multi-pass pocketing cut through the 2.2 mm thick sample using 4 laser passes at maximum power with re-focusing. SEM images revealed fiber pull-out, fiber swelling, and matrix re-solidification along machined surfaces in the absence of an inert assist gas flow. Laser contour drilling of cross-ply samples showed a non-uniform HAZ; SEM images showed a smooth hole surface texture in the presence of an Argon assist gas flow.

Overall, it was shown that nanosecond laser machining at low frequency and high pulse energy significantly reduced thermal damage and increased the ablation rate compared to the CW/modulated laser system from Chapter 3. The ablation process is categorized as photo-thermal given the photon energy of NIR wavelengths, the low laser-induced excitation rate relative to the thermal response time of the carbon reinforcements, and the transmissivity of the matrix for NIR irradiation. However, it is proposed that both thermal and non-thermal laser ablation may occur due to the Gaussian distribution of high energy nanosecond pulses within the laser beam target area. Further study into laser machining of CFRP using UV laser systems is recommended, particularly using Long-Duration nanosecond-pulsed laser systems, for direct comparison of the effect of emission wavelength on thermal damage to the matrix.

CHAPTER 5.

CONCLUSIONS AND FUTURE WORK

5.1 Conclusions

It has been shown experimentally that laser machining can provide drastically improved processing quality for CFRP over conventional methods. Specifically, results using a CW/modulate NIR fiber laser system produced extensive thermal damage and a low ablation rate. Machining using a high energy nanosecond IR laser system produced superior results in terms of reduced thermal damage and efficient material removal through an increased ablation rate.

In Chapter 2, it was concluded that surface damage is the limiting factor in mechanical machining of CFRP using both a standard drill and split-point-fiber (SPF) drill. Axial thrust force proportional to the rotational feed rate caused significant surface damage, as verified by dynamometer measurements. Damage to cross-ply sample was in the form of delamination in the entry and exit surface laminate layers, while damage to woven samples was mainly characterized as peeling along the contour. Surface roughness also suffered at higher spindle speeds using the SPF drill.

Chapter 3 showed that machining using a CW/modulated Yb:YAG IR fiber laser system is characterized by low ablation rates and large areas of thermal damage. Long laser-material interaction time at low pulse energy promotes heat accumulation, increasing thermal damage. Also, the penetration depth of IR irradiation is reduced due to low power intensity, reducing the ablation rate. These effects are exacerbated during continuous wave (CW) mode operation. Energy density provided a more accurate prediction of results by accounting for all variations in laser process parameters in a single control variable.

The machining process was substantially improved using the high energy nanosecond Nd:YAG IR laser system from Chapter 4. Laser-induced plasma effects became important as a result of increased power intensity, rendering Q-Switch pulse mode ineffective due to optical breakdown and triggering plasma shielding in Long Pulse mode. Long Pulse mode efficiently ablated both CFRP materials during both multi-pass machining and contour drilling. Through-cutting of 2.2 mm thick samples was achieved in as few as 4 laser scans and small diameter holes were drilled with limited thermal damage. The use of Argon assist gas was shown to reduce oxidation and improve surface quality.

5.2 Future Work

High energy nanosecond IR laser machining was found to improve ablation rates and reduce damage thermal damage by using short pulse duration and high power intensity. However, future study with a comparable laser system in the UV range is recommended. Photon energy at UV wavelengths is sufficient to directly break carbon bonds within the reinforcements by photo-chemical laser ablation. UV laser machining of CFRP has been studied, but not using short-duration high-energy pulsing, particularly in the context of laser-induced plasma effects resulting from the increased power intensity. The inverse Bremsstrahlung absorption coefficient is proportional to λ^3 and is drastically reduced in the UV spectrum. Also, higher pulse frequency is recommended to allow for faster scanning speed and reduced processing time.

REFERENCES

Anzai, K., Aoyama, M., Fujisaki, A., Miyato, T., Kayahara, T., Harada, Y., Niino, H., 2014. Laser trepanning of CFRP with a scanner head for IR and UV lasers. Proc. SPIE. doi:10.1117/12.2037264

Attia, H., Sadek, A., Meshreki, M., 2011. High speed machining processes for fiber-reinforced composites, in: Machining Technology for Composite Materials: Principles and Practice. Woodhead Publishing Cambridge, UK.

Beal, V.E., Paggi, R.A., Salmoria, G. V., Lago, A., 2009. Statistical evaluation of laser energy density effect on mechanical properties of polyamide parts manufactured by selective laser sintering. J. Appl. Polym. Sci. 113, 2910–2919. doi:10.1002/app.30329

BMW acquires stake in SGL Carbon, 2012. . Reinf. Plast. 56, 12. doi:10.1016/S0034-3617(12)70017-6

Bogaerts, A., Chen, Z., Gijbels, R., Vertes, A., 2003. Laser ablation for analytical sampling: what can we learn from modeling? Spectrochim. Acta Part B At. Spectrosc. 58, 1867–1893. doi:10.1016/j.sab.2003.08.004

Borisov, O.V., Mao, X.L., Ciocan, A.C., Russo, R.E., 1998. Time-resolved parametric studies of laser ablation using inductively coupled plasma atomic emission spectroscopy. Appl. Surf. Sci. 127–129, 315–320. doi:10.1016/S0169-4332(97)00649-1

Brown, M.S., Arnold, C.B., 2010. Fundamentals of Laser-Material Interaction and Application to Multiscale Surface Modification, in: Sugioka, K., Meunier, M., Piqué, A. (Eds.), Laser Precision Microfabrication. Springer Berlin Heidelberg, Berlin, Heidelberg, pp. 91–120. doi:10.1007/978-3-642-10523-4_4

Cabalín, L.M., Laserna, J.J., 1998. Experimental determination of laser induced breakdown thresholds of metals under nanosecond Q-switched laser operation. Spectrochim. Acta Part B At. Spectrosc. 53, 723–730. doi:10.1016/S0584-8547(98)00107-4

Campbell, F.C., 2006. Structural Assembly, in: Manufacturing Technology for Aerospace Structural Materials. Elsevier, pp. 495–537. doi:10.1016/B978-185617495-4/50011-1

Caprino, G., Tagliaferri, V., 1988. Maximum cutting speed in laser cutting of fiber reinforced plastics. Int. J. Mach. Tools Manuf. 28, 389–398. doi:10.1016/0890-6955(88)90052-1

Cherif, C. (Ed.), 2011. Textile Werkstoffe für den Leichtbau. Springer Berlin Heidelberg, Berlin, Heidelberg. doi:10.1007/978-3-642-17992-1

DAVIM, J., RUBIO, J., ABRAO, A., 2007. A novel approach based on digital image analysis to evaluate the delamination factor after drilling composite laminates. Compos. Sci. Technol. 67, 1939–1945. doi:10.1016/j.compscitech.2006.10.009

Denkena, B., Volkermeyer, F., Kling, R., Hermsdorf, J., 2007. Novel UV–laser applications for carbon fibre reinforced plastics, in: Applied Production Technology. Bremen, pp. 99–108.

Dutta Majumdar, J., Manna, I., 2003. Laser processing of materials. Sadhana 28, 495–562. doi:10.1007/BF02706446

Eland, K.L., Stratis, D.N., Gold, D.M., Goode, S.R., Angel, S.M., 2001. Energy dependence of emission intensity and temperature in a LIBS plasma using femtosecond excitation. Appl. Spectrosc. 55, 286–291.

Emmelmanna, C., Petersen, M., Goeke, A., Canisius, M., 2011. Analysis of laser ablation of CFRP by ultra-short laser pulses with short wavelength, in: Physics Procedia. pp. 565–571. doi:10.1016/j.phpro.2011.03.071

Faraz, A., Biermann, D., Weinert, K., 2009. Cutting edge rounding: An innovative tool wear criterion in drilling CFRP composite laminates. Int. J. Mach. Tools Manuf. 49, 1185–1196. doi:10.1016/j.ijmachtools.2009.08.002

Feito, N., Diaz-Álvarez, A., Cantero, J.L., Rodríguez-Millán, M., Miguélez, H., 2015. Experimental analysis of special tool geometries when drilling woven and multidirectional CFRPs. J. Reinf. Plast. Compos. 35, 33–55. doi:10.1177/0731684415612931

Fischer, F., Romoli, L., Kling, R., 2010. Laser-based repair of carbon fiber reinforced plastics. CIRP Ann. - Manuf. Technol. 59, 203–206. doi:10.1016/j.cirp.2010.03.075

French, P., Naeem, M., Wolynski, A., Sharp, M., 2010. Fibre laser material processing of aerospace composites 103, 1028–1035.

Fuchs, A.N., Schoeberl, M., Tremmer, J., Zaeh, M.F., 2013. Laser Cutting of Carbon Fiber Fabrics. Phys. Procedia 41, 372–380. doi:10.1016/j.phpro.2013.03.090

Fujita, M., Ohkawa, H., Somekawa, T., Otsuka, M., Maeda, Y., Matsutani, T., Miyanaga, N., 2016. Wavelength and pulsewidth dependences of laser processing of CFRP, in: Physics Procedia. pp. 1031–1036. doi:10.1016/j.phpro.2016.08.108

Gardiner, G., 2014. Hole quality defined : CompositesWorld [WWW Document]. Compos. World. URL http://www.compositesworld.com/articles/hole-quality-defined (accessed 9.7.17).

Gaugel, S., Sripathy, P., Haeger, A., Meinhard, D., Bernthaler, T., Lissek, F., Kaufeld, M., Knoblauch, V., Schneider, G., 2016. A comparative study on tool wear and laminate damage in drilling of carbon-fiber reinforced polymers (CFRP). Compos. Struct. 155, 173–183. doi:10.1016/j.compstruct.2016.08.004

Han, Q., Wang, L., Xu, J., 2016. Experimental research on fracture behaviors of damaged CFRP tendons: Fracture mode and failure analysis. Constr. Build. Mater. 112, 1013–1024. doi:10.1016/j.conbuildmat.2016.03.036

Herzog, D., Schmidt-Lehr, M., Canisius, M., Oberlander, M., Tasche, J.-P., Emmelmann, C., 2015. Laser cutting of carbon fiber reinforced plastic using a 30 kW fiber laser. J. Laser Appl. 27, S28001. doi:10.2351/1.4906304

Herzog, D., Schmidt-Lehr, M., Oberlander, M., Canisius, M., Radek, M., Emmelmann, C., 2016. Laser cutting of carbon fibre reinforced plastics of high thickness. Mater. Des. 92, 742–749. doi:10.1016/j.matdes.2015.12.056

Hexcel, 2014a. HexTow® IM7.

Hexcel, 2014b. HexTow® AS4.

Hexcel Corporation, 2000. FORWARD-LOOKING STATEMENTS: Risks, Uncertainties, Other Factors with Respect to " Forward-Looking Statements " [WWW Document]. Annu. Rep. URL http://media.corporate-ir.net/media_files/NYS/HXL/reports/ar_2000.pdf (accessed 9.11.17).

Ho-Cheng, H., Dharan, C.K.H., 1990. Delamination During Drilling in Composite Laminates. J. Eng. Ind. 112, 236. doi:10.1115/1.2899580

Hocheng, H., Tsao, C.C., 2006. Effects of special drill bits on drilling-induced delamination of composite materials. Int. J. Mach. Tools Manuf. 46, 1403–1416. doi:10.1016/j.ijmachtools.2005.10.004

Hoffman, J., Chrzanowska, J., Kucharski, S., Moscicki, T., Mihailescu, I.N., Ristoscu, C., Szymanski, Z., 2014. The effect of laser wavelength on the ablation rate of carbon. Appl. Phys. A 117, 395–400.

Iliescu, D., Gehin, D., Gutierrez, M.E., Girot, F., 2010. Modeling and tool wear in drilling of CFRP. Int. J. Mach. Tools Manuf. 50, 204–213. doi:10.1016/j.ijmachtools.2009.10.004

Ishioka, K., Hase, M., Kitajima, M., Wirtz, L., Rubio, A., Petek, H., 2008. Ultrafast electron-phonon decoupling in graphite. Phys. Rev. B 77, 121402. doi:10.1103/PhysRevB.77.121402

Jung, K.-W., Kawahito, Y., Katayama, S., 2012. Ultra-high speed disk laser cutting of carbon fiber reinforced plastics. J. Laser Appl. 24, 12007. doi:10.2351/1.3673521

Kampfrath, T., Perfetti, L., Schapper, F., Frischkorn, C., Wolf, M., 2005. Strongly Coupled Optical Phonons in the Ultrafast Dynamics of the Electronic Energy and Current Relaxation in Graphite. Phys. Rev. Lett. 95, 187403. doi:10.1103/PhysRevLett.95.187403

Kim, D., Ramulu, M., Doan, X., 2005. Influence of consolidation process on the drilling performance and machinability of PIXA-M and PEEK thermoplastic composites. J. Thermoplast. Compos. Mater. 18, 195–217.

König, W., Graß, P., 1989. Quality Definition and Assessment in Drilling of Fibre Reinforced Thermosets. CIRP Ann. - Manuf. Technol. 38, 119–124. doi:10.1016/S0007-8506(07)62665-1

Kononenko, T. V, Freitag, C., Komlenok, M.S., Onuseit, V., Weber, R., Graf, T., Konov, V.I., 2014. Oxygen-assisted multipass cutting of carbon fiber reinforced plastics with ultra-short laser pulses. J. Appl. Phys. 115, 103107. doi:10.1063/1.4868385

Köpf, A., Feistritzer, S., Udier, K., 2006. Diamond coated cutting tools for machining of non-ferrous metals and fibre reinforced polymers. Int. J. Refract. Met. Hard Mater. 24, 354–359. doi:10.1016/j.ijrmhm.2005.11.013

Koplev, A., Lystrup, A., Vorm, T., 1983. The cutting process, chips, and cutting forces in machining CFRP. Composites 14, 371–376. doi:10.1016/0010-4361(83)90157-X

Kroll, N., Watson, K.M., 1972. Theoretical Study of Ionization of Air by Intense Laser Pulses. Phys. Rev. A 5, 1883–1905. doi:10.1103/PhysRevA.5.1883

Lau, W.S., Lee, W.B., Pang, S.Q., 1990. Pulsed Nd: YAG Laser Cutting of Carbon Fibre Composite Materials. CIRP Ann. - Manuf. Technol. 39, 179–182. doi:10.1016/S0007-8506(07)61030-0

Lednev, V.N., Pershin, S.M., Obraztsova, E.D., Kudryashov, S.I., Bunkin, A.F., 2013. Single-shot and single-spot measurement of laser ablation threshold for carbon nanotubes. J. Phys. D. Appl. Phys. 46, 52002.

Leider, H.., Krikorian, O.., Young, D.., 1973. Thermodynamic properties of carbon up to the critical point. Carbon N. Y. 11, 555–563. doi:10.1016/0008-6223(73)90316-3

Leone, C., Genna, S., Tagliaferri, V., 2014. Fibre laser cutting of CFRP thin sheets by multi-passes scan technique. Opt. Lasers Eng. 53, 43–50.

Leone, C., Pagano, N., Lopresto, V., Iorio, I. De, 2009. Solid state Nd : YAG laser cutting of CFRP sheet : influence of process parameters on kerf geometry and HAZ. 17th Int. Conf. Compos. Mater.

Leone, C., Papa, I., Tagliaferri, F., Lopresto, V., 2013. Investigation of CFRP laser milling using a 30W Q-switched Yb:YAG fiber laser: Effect of process parameters on removal mechanisms and HAZ formation. Compos. Part A Appl. Sci. Manuf. 55, 129–142. doi:10.1016/j.compositesa.2013.08.004

Li, Z.L., Chu, P., Zheng, H., Lim, G., Li, L., Marimuthu, S., Negarestani, R., Sheikh, M., 2008. Process development of laser machining of carbon fibre reinfoenced plastic composites, in: 27th International Congress Application of Lasers and Electro-Optics (ICALEO08), Temecular, CA, USA, 20-23 October. pp. 222–230.

Li, Z.L., Zheng, H.Y., Lim, G.C., Chu, P.L., Li, L., 2010. Study on UV laser machining quality of carbon fibre reinforced composites. Compos. Part A Appl. Sci. Manuf. 41, 1403–1408. doi:10.1016/j.compositesa.2010.05.017

Lopresto, V., Caggiano, A., Teti, R., 2016. High Performance Cutting of Fibre Reinforced Plastic Composite Materials. Procedia CIRP 46, 71–82. doi:10.1016/j.procir.2016.05.079

M'Saoubi, R., Axinte, D., Soo, S.L., Nobel, C., Attia, H., Kappmeyer, G., Engin, S., Sim, W.-M., 2015. High performance cutting of advanced aerospace alloys and composite materials. CIRP Ann. - Manuf. Technol. doi:10.1016/j.cirp.2015.05.002

Mascarin, A., Hannibal, T., Raghunathan, A., Ivanic, Z., Francfort, J., 2015. Vehicle Lightweighting: 40% and 45% Weight Savings Analysis: Technical Cost Modeling for Vehicle Lightweighting. Idaho National Lab.(INL), Idaho Falls, ID (United States).

Mathew, J., Goswami, G.L., Ramakrishnan, N., Naik, N.K., 1999. Parametric studies on pulsed Nd:YAG laser cutting of carbon fibre reinforced plastic composites. J. Mater. Process. Technol. 89–90, 198–203. doi:10.1016/S0924-0136(99)00011-4

Mazumdar, S., Karthikeyan, D., Pichler, D., Benevento, M., Frassine, R., 2016. State of the Composites Industry, Composites Manufacturing Magazine.

McKie, A.D.W., Addison, R.C., 1994. Practical considerations for the rapid inspection of composite materials using laser-based ultrasound. Ultrasonics 32, 333–345. doi:10.1016/0041-624X(94)90103-1

Meredith, J., Bilson, E., Powe, R., Collings, E., Kirwan, K., 2015. A performance versus cost analysis of prepreg carbon fibre epoxy energy absorption structures. Compos. Struct. 124, 206–213. doi:10.1016/j.compstruct.2015.01.022

Modest, M.F., 1996. Transient Model for CW and Pulsed Laser Machining of Ablating/Decomposing Materials-Approximate Analysis. Trans. Soc. Mech. Eng. J. HEAT Transf. 118, 774–780.

Morgan, C.G., 1975. Laser-induced breakdown of gases. Reports Prog. Phys. 38, 621–665. doi:10.1088/0034-4885/38/5/002

Mucha, P., Weber, R., Speker, N., Berger, P., Sommer, B., Graf, T., 2014. Calibrated heat flow model for determining the heat conduction losses in laser cutting of CFRP, in: Physics Procedia. pp. 1208–1217. doi:10.1016/j.phpro.2014.08.036

Murphy, C., Byrne, G., Gilchrist, M.D., 2002. The performance of coated tungsten carbide drills when machining carbon fibre-reinforced epoxy composite materials. Proc. Inst. Mech. Eng. Part B J. Eng. Manuf. 216, 143–152.

Negarestani, R., 2010. Laser cutting of carbon fibre-reinforced polymer composite materials.

Negarestani, R., Li, L., Sezer, H.K., Whitehead, D., Methven, J., 2010. Nano-second pulsed DPSS Nd:YAG laser cutting of CFRP composites with mixed reactive and inert gases. Int. J. Adv. Manuf. Technol. 49, 553–566. doi:10.1007/s00170-009-2431-y

Niino, H., Kurosaki, R., 2011. Laser cutting of carbon fiber reinforced plastics (CFRP) by UV pulsed laser ablation. Proc. SPIE. doi:10.1117/12.876231

Ohkubo, T., Tsukamoto, M., Sato, Y., 2014. Numerical simulation of laser beam cutting of carbon fiber reinforced plastics, in: Physics Procedia. pp. 1165–1170. doi:10.1016/j.phpro.2014.08.031

Pecat, O., Rentsch, R., Brinksmeier, E., 2012. Influence of Milling Process Parameters on the Surface Integrity of CFRP. Procedia CIRP 1, 466–470. doi:10.1016/j.procir.2012.04.083

Ramulu, M., 1997. Machining and surface integrity of fibre-reinforced plastic composites. Sadhana 22, 449–472. doi:10.1007/BF02744483

Rawat, S., Attia, H., 2009. Wear mechanisms and tool life management of WC–Co drills during dry high speed drilling of woven carbon fibre composites. Wear 267, 1022–1030. doi:10.1016/j.wear.2009.01.031

Rentsch, R., Mamedov, S., n.d. u169 Crack Formation and Crack Path in CFRP Machining, in: CP2012.

Riveiro, A., Quintero, F., Lusquiños, F., del Val, J., Comesaña, R., Boutinguiza, M., Pou, J., 2012. Experimental study on the CO2 laser cutting of carbon fiber reinforced plastic composite. Compos. Part A Appl. Sci. Manuf. 43, 1400–1409. doi:10.1016/j.compositesa.2012.02.012

Rodden, W.S.., 2002. A comprehensive study of the long pulse Nd:YAG laser drilling of multi-layer carbon fibre composites. Opt. Commun. 210, 319–328. doi:10.1016/S0030-4018(02)01807-2

Romoli, L., Fischer, F., Kling, R., 2012. A study on UV laser drilling of PEEK reinforced with carbon fibers. Opt. Lasers Eng. 50, 449–457. doi:10.1016/j.optlaseng.2011.10.008

Russo, R.E., Mao, X.L., Yoo, J.H., Gonzalez, J.J., 2007. Laser Ablation, in: Laser-Induced Breakdown Spectroscopy. pp. 49–82. doi:10.1016/B978-044451734-0.50006-5

Sadek, A., Meshreki, M., Attia, M.H., 2012. Characterization and optimization of orbital drilling of woven carbon fiber reinforced epoxy laminates. CIRP Ann. - Manuf. Technol. 61, 123–126. doi:10.1016/j.cirp.2012.03.089

Salama, A., Li, L., Mativenga, P., Sabli, A., 2016a. High-power picosecond laser drilling/machining of carbon fibre-reinforced polymer (CFRP) composites. Appl. Phys. A 122, 73. doi:10.1007/s00339-016-9607-8

Salama, A., Li, L., Mativenga, P., Whitehead, D., 2016b. TEA CO2 laser machining of CFRP composite. Appl. Phys. A 122, 497. doi:10.1007/s00339-016-0025-8

Salama, A., Yan, Y., Li, L., Mativenga, P., Whitehead, D., Sabli, A., 2016c. Understanding the self-limiting effect in picosecond laser single and multiple parallel pass drilling/machining of CFRP composite and mild steel. Mater. Des. 107, 461–469. doi:10.1016/j.matdes.2016.06.048

Sankaranarayanan, S., Kar, A., 1999. Nonlinear effects of laser-plasma interaction on melt-surface temperature. J. Phys. D. Appl. Phys. 32, 777–784. doi:10.1088/0022-3727/32/7/005

Sato, Y., Tsukamoto, M., Nariyama, T., Nakai, K., Takahashi, K., Masuno, S., Nakano, H., 2013. Experimental study of CFRP cutting with nanosecond lasers.

Schittenhelm, H., Callies, G., Berger, P., Hügel, H., 1996. Investigations of extinction coefficients during excimer laser ablation and their interpretation in terms of Rayleigh scattering. J. Phys. D. Appl. Phys. 29, 1564–1575. doi:10.1088/0022-3727/29/6/023

Sedov, L., 1993. Similarily and dimesional methods in mechanics, 10th ed. CRC Press.

Shyha, I., Soo, S.L., Aspinwall, D., Bradley, S., 2010. Effect of laminate configuration and feed rate on cutting performance when drilling holes in carbon fibre reinforced plastic composites. J. Mater. Process. Technol. 210, 1023–1034. doi:10.1016/j.jmatprotec.2010.02.011

Steel is "Cooked" If BMW's i3 Takes Off - EVWORLD.COM [WWW Document], 2013. . EV World. URL http://evworld.com/news.cfm?newsid=31837 (accessed 9.7.17).

Steen, W.M., 2003. Laser material processing—an overview. J. Opt. A Pure Appl. Opt. 5, S3–S7. doi:10.1088/1464-4258/5/4/351

Takahashi, K., Tsukamoto, M., Masuno, S., Sato, Y., 2016. Heat conduction analysis of laser CFRP processing with IR and UV laser light. Compos. Part A Appl. Sci. Manuf. 84, 114–122. doi:10.1016/j.compositesa.2015.12.009

Takahashi, K., Tsukamoto, M., Masuno, S., Sato, Y., Yoshida, H., Tsubakimoto, K., Fujita, H., Miyanaga, N., Fujita, M., Ogata, H., 2015. Influence of laser scanning conditions on CFRP processing with a pulsed fiber laser. J. Mater. Process. Technol. 222, 110–121. doi:10.1016/j.jmatprotec.2015.02.043

Teti, R., 2002. Machining of Composite Materials. CIRP Ann. - Manuf. Technol. 51, 611–634. doi:10.1016/S0007-8506(07)61703-X

Thiyagarajan, M., Thompson, S., 2012. Optical breakdown threshold investigation of 1064 nm laser induced air plasmas. J. Appl. Phys. 111, 73302.

Ushida, K., Wataru, I., Shimamura, Y., Kawata, Y., 2012. Characteristic analysis of CFRP cutting with nanosecond pulsed laser. J. Adv. Res. Phys. 3.

Voisey, K.T., Fouquet, S., Roy, D., Clyne, T.W., 2006. Fibre swelling during laser drilling of carbon fibre composites. Opt. Lasers Eng. 44, 1185–1197. doi:10.1016/j.optlaseng.2005.10.008

Völkermeyer, F., Fischer, F., Stute, U., Kracht, D., 2011. Laser-based approach for bonded repair of carbon fiber reinforced plastics, in: Physics Procedia. pp. 537–542. doi:10.1016/j.phpro.2011.03.066

Weber, R., Freitag, C., Kononenko, T. V., Hafner, M., Onuseit, V., Berger, P., Graf, T., 2012. Short-pulse Laser Processing of CFRP, in: Physics Procedia. pp. 137–146. doi:10.1016/j.phpro.2012.10.023

Weber, R., Hafner, M., Michalowski, A., Graf, T., 2011. Minimum Damage in CFRP Laser Processing. Phys. Procedia 12, 302–307. doi:10.1016/j.phpro.2011.03.137

Wolynski, A., Herrmann, T., Mucha, P., Haloui, H., L'huillier, J., 2011. Laser ablation of CFRP using picosecond laser pulses at different wavelengths from UV to IR, in: Physics Procedia. pp. 292–301. doi:10.1016/j.phpro.2011.03.136

Wu, C.W., Wu, X.Q., Huang, C.G., 2015. Ablation behaviors of carbon reinforced polymer composites by laser of different operation modes. Opt. Laser Technol. 73, 23–28. doi:10.1016/j.optlastec.2015.04.008

Xu, H., Hu, J., 2017. Modeling of the material removal and heat affected zone formation in CFRP short pulsed laser processing. Appl. Math. Model. 46, 354–364. doi:10.1016/j.apm.2017.01.072

Zazula, J.M., 1997. On Graphite Transformations at High Temperature and Pressure Induced By Absorption of the LHC Beam. Geneva.

Zel'dovich, Y., Raizer, Y., 2002. Physics of shock waves and high-temperature hydrodynamics phenomena. Dover Publications.

Zeng, X., Mao, X.L., Greif, R., Russo, R.E., 2005. Experimental investigation of ablation efficiency and plasma expansion during femtosecond and nanosecond laser ablation of silicon. Appl. Phys. A Mater. Sci. Process. 80, 237–241.